

ABSTRACT

SHAH, PARTH VIDYUT. Chemi-ionization and Nanoparticle Charging in Oxy-fuel Flames. (Under the direction of Dr. Alexei Saveliev).

Charged species are formed in all combustion processes. Even though they are present in small amounts they offer wider range of applications including flame control and nanoparticle formation like soot. Hence, understanding the chemistry of charged species and their interaction with particles is of critical importance.

In the present study, charged species formed in a laminar counterflow diffusion flame of methane and oxygen enriched air are studied experimentally and numerically. An experimental method of measuring electron and total positive ion concentration is used. Electric current is measured as a function of the applied voltage, and volt-ampere characteristics are obtained at different points between the two nozzles of the counterflow burner at positive and negative potentials for different oxygen concentrations and different strain rates. The Langmuir probe theory is used to evaluate the spatial ion and electron concentrations from the volt-ampere curves. Mole fractions and concentrations of major individual charged species are predicted using a one-dimensional counterflow diffusion flame model. A 63 step chemi-ionization mechanism in addition to a 208 step methane-air combustion mechanism is used to model the chemical kinetics of the flame at different oxygen concentrations and strain rates. The effect of thermoionization of the neutral species is also analyzed.

With no external electric field nanoparticle charging is mainly governed by diffusion of charge carriers that are produced by chemi-ionization that electrostatically interact with particles. Another mechanism involves thermal ionization at high temperatures. A numerical model that describes the charging mechanism of a spherical nanoparticle in a methane-air counterflow laminar diffusion flame in oxy-fuel conditions is developed. The detailed kinetic model considers the production of ions and electrons

in a methane-air flame due to chemi-ionization, thermal ionization and charging due to diffusion. The model is analyzed to study the effects of temperature, total nanoparticle concentration and chemi-ionization on nanoparticle charging and on ion and electron concentrations. The nanoparticle charging model is also extended to agglomerates by making changes to the model for the primary particles. The effect of charging for linear chain aggregates with fractal dimension of 1.0 is compared to that for fractal agglomerates with fractal dimension of 1.6. The nanoparticle model is validated by comparison with previous experimental results.

© Copyright 2015 by Parth Shah

All Rights Reserved

Chemi-ionization and Nanoparticle Charging in Oxy-fuel flames

by
Parth V. Shah

A dissertation submitted to the Graduate Faculty of
North Carolina State University
in partial fulfillment of the
requirements for the degree of
Doctor of Philosophy

Aerospace Engineering

Raleigh, North Carolina

2015

APPROVED BY:

Dr. Alexei Saveliev
Committee Chair

Dr. Mohamed Bourham

Dr. Tarek Echehki

Dr. Tiegang Fang

DEDICATION

This work is dedicated to my parents and my sister for their unconditional and undiminishing love and support. This work is also dedicated to my thesis advisor Prof. Saveliev for his flawless and enlightening guidance and mentoring. Undoubtedly, this short dedication is extremely insufficient to describe the immense contributions they have made to this work.

BIOGRAPHY

The author was born in Ahmedabad, India to a loving housewife and a charming businessman, though soon he moved to the city of Mumbai where he grew up. He also has a beautiful sister who is a French teacher at a prestigious high school in Mumbai. He received a bachelor's degree in Production Engineering from Dwarkadas J. Sanghvi College of Engineering, Mumbai in 2007 which at that time was affiliated with University of Mumbai. Since childhood he has always been fascinated by NASA, space and planes. The closest thing he could do to learn about planes was to go to the city airport and watch planes land and take off. Since he couldn't fulfill his dream of pursuing a career in aeronautics in India, in the fall of 2007 he moved to sunny California where he received his Masters in Aerospace Engineering from University of Southern California, Los Angeles in 2009 to pursue knowledge in aeronautics. In the fall of 2009 he got accepted to North Carolina State University, Raleigh for a doctoral degree in Aerospace Engineering to advance his interests in combustion and propulsion. After a few semesters at the school, he found an amazing opportunity to work with Prof. Alexei Saveliev to work pursue research in the electrical aspects of flames. After graduation he will move to Minneapolis, MN to begin his employment as a Postdoctoral Associate at the University of Minnesota with Prof. Steven Girshick where he will have the exciting opportunity to work on numerical modeling of nanodusty plasmas.

ACKNOWLEDGEMENTS

Many people have my appreciation for my time at NC State. First and foremost, I would like to express my deep gratitude towards Prof. Alexei Saveliev who has been my thesis advisor and my mentor for the past four years. I haven't met anyone with as much knowledge coupled with humility and patience as Prof. Saveliev. He also helped me during my tough financial times by providing me with assistantships and research opportunities. I'm truly grateful. He not only provided me with valuable scientific and technical inputs but has also taught me how to think as a researcher. I feel truly privileged to have worked with him. I would also like to thank Prof. Bourham, Prof. Echekeki and Prof. Fang for their valuable inputs and valuable academic classes. The above four gentlemen have helped me generate a profound and an elevated sense of respect for professors and scientists and one day I hope to become a great researcher like them.

My friends have made this journey incredible. I would have never thought that I'd make so many friends who would become like family in Raleigh. They have always encouraged me as well helped me through some tough financial times. The list of these friends is too long for me to mention them all in one page. Kindly forgive me for that.

Finally, I would like to thank my parents and my sister for supporting me and sacrificing these many years so that I can fulfill my dream. I realize that this short acknowledgement is far from enough to show my love and respect for my family.

TABLE OF CONTENTS

LIST OF TABLES	viii
LIST OF FIGURES	ix
1 Introduction	1
1.1 Ions and electrons in flames	1
1.1.1 Ionization in flames	1
1.1.2 Ions in methane- oxygen flames.....	5
1.1.3 Electric field effects.....	6
1.1.4 Numerical models	6
1.2 Nanoparticle charging	7
1.2.1 Charging mechanisms	8
1.2.2 Effect of particle morphology on charging	14
1.3 Thesis Objectives	15
2 Experimental study	16
2.1 Diffusion / Nonpremixed flame	16
2.1.1 Counterflow flame	16
2.1.2 Burner configuration.....	18
2.2 Electric probe	20
2.2.1 Langmuir probe theory	20
2.2.2 Modifications to the probe.....	28
3 Flame modeling	30
3.1 Counterflow flame model.....	30
3.2 Transport properties	33
3.3 Ambipolar diffusion.....	34
3.4 Numerical method	35
4 Model data	36
4.1 Reaction mechanism	36
4.1.1 Charged species.....	37

4.2	Thermodynamic data	38
4.3	Transport data	39
5	Results of the flame experiments and model	40
5.1	Flame structure	40
5.1.1	Effect of oxygen content.....	40
5.1.2	Effect of strain rate	43
5.2	Volt-Ampere (VAC) Characteristics	45
5.3	Ion and electron profiles	46
5.3.1	Effect of oxygen content and strain rate on peak charged species concentrations.....	50
5.4	Conservation of charge	52
5.5	Effect of gas-phase thermal-ionization	52
6	Primary nanoparticle charging model	56
6.1	Theory and Objective	56
6.2	Chemi-ionization model	57
6.3	Bipolar diffusion charging model	59
6.4	Thermal-ionization model	62
6.5	Model formulation and validation	63
7	Results of the primary nanoparticle charging model	69
7.1	Fixed ion and electron concentration.....	69
7.2	Zero chemi-ionization.....	71
7.3	Negligible thermal-ionization	72
7.4	Ions and electrons interacting with charged particles.....	75
7.4.1	Charged particle distribution.....	75
7.4.2	Average particle charge	77
7.4.3	Electron concentration	87
7.4.4	Ion concentration.....	92
8	Nanoparticle agglomerates charging model	95
8.1	Theory	95

8.2	Modifications to the primary nanoparticle charging model.....	96
8.3	Model formulation and validation	99
8.4	Results of the nanoparticle agglomerates charging model.....	102
8.4.1	Zero chemi-ionization.....	102
8.4.2	Zero thermal-ionization.....	104
8.4.3	Relative charge and effects on ions and electrons	106
8.4.4	Ions and electrons in equilibrium with charged agglomerates	109
9	Conclusions.....	112
	REFERENCES	115
	APPENDICES	124
	Appendix A: Numerical scheme for the charging model	125

LIST OF TABLES

Table 2-1. Parameters to calculate the ion and electron concentrations for probe configuration P1.....	25
Table 4-1. List of charged species included in the model.....	37

LIST OF FIGURES

Fig. 1.1. Sources of ions and electrons in flames.	3
Fig. 1.2. Schematic of various nanoparticle charging mechanisms (Sahu et al, 2012). 8	
Fig. 2.1 Schematic of a laminar counterflow diffusion flame.....	17
Fig. 2.2 Schematic of the counter flow diffusion flame burner (Desai, 2010).	19
Fig. 2.3. Schematic of the Langmuir probe measurements for P1.	21
Fig. 2.4. Typical VAC of a single Langmuir probe.....	22
Fig. 2.5. VAC curves with probe configuration P1 for 50% O ₂ at (a) 10 mm (b) 15 mm from fuel nozzle.	26
Fig. 2.6. VAC curves with probe configuration P1 for 100% O ₂ at (a) 10 mm (b) 15 mm from fuel nozzle.	27
Fig. 2.7. Schematic of the probe with a cooling system (P2).	29
Fig. 5.1. Effect of oxygen on flame structure at 20 s ⁻¹ (Desai, 2010).	41
Fig. 5.2. Effect of oxygen content at 20 s ⁻¹ on the (a) Flame temperature profile (b) axial velocity profile.	42
Fig. 5.3. Effect of strain rate on flame structure at 100% O ₂ (Desai, 2010).....	43
Fig. 5.4. Effect of strain rate at 100 s ⁻¹ on the (a) Flame temperature profile (b) axial velocity profile.	44
Fig. 5.5. VAC for 21% O ₂ at 10 mm from the nozzle to measure electron saturation current ion saturation current.	45
Fig. 5.6. VAC for 75% O ₂ at 10 mm from the nozzle to measure (a) electron saturation current (b) ion saturation current.....	46
Fig. 5.7 Distributions of major positive and negative ions in a methane –air diffusion flame at 20 s ⁻¹	47
Fig. 5.8. Ion and electron profiles at (a) 21% O ₂ (b) 75% O ₂	49

Fig. 5.9. Effect of (a) oxygen content (b) strain rate on peak charged species concentration.....	51
Fig. 5.10. Electron density as a function of temperature from major neutral species in the flame.	54
Fig. 5.11. Comparison of electrons produced from thermal-ionization and chemi-ionization.....	55
Fig. 6.1. Schematic of the interaction between ions, electrons and nanoparticles in a hydrocarbon flame.	64
Fig. 6.2. Comparison of relative soot volume fraction: experimental results by Homann and Wolf (1983) (symbols), computed (solid lines) and model by Balthasar et al. (2002) (dashed lines).....	67
Fig. 6.3. Comparison of relative number density: our modeling results (solid lines) and model by Balthasar et al. (2002) (dashed lines) (a) negatively charged particles (b) positively charged particles.	68
Fig. 7.1. Comparison of fraction of charged particles for fixed total electron and ion concentration at (a) 1000 K (b) 2000 K (c) 3000 K.	70
Fig. 7.2. Comparison of fraction of charged particles for zero chemi-ionization.	72
Fig. 7.3. Comparison of distribution of charged particles for zero thermal -ionization at (a) 1000 K (b) 2000 K (c) 3000 K for a fixed $N_p=10^{15} \text{ m}^{-3}$	74
Fig. 7.4. Distribution of charged particles for different η at (a) 1000 K, (b) 2000 K and (c) 3000 K.	76
Fig. 7.5. Charge distributions for the nanoparticles of TiO_2 , MoO_3 , and graphite introduced in the flame environment with $T = 3000 \text{ K}$ and $N_{e(chemi)} = 0$	77
Fig. 7.6. Comparison of average charge carried by a 20 nm spherical particle at different temperatures.....	79

Fig. 7.7. Comparison of average charge accumulated on a 20 nm particle as a function of temperature with $N_{e(chemi)} = 10^{15} m^{-3}$ at 3 different η	81
Fig. 7.8 Comparison of average charge formed on a 20 nm particle versus electrons and ions formed per unit volume by chemi-ionization at three different temperatures with $N_p = 10^{15} m^{-3}$	82
Fig. 7.9. Comparison of average charge formed on a 20 nm particle as a function of total nanoparticle concentration for a fixed $N_{e(chemi)} = 10^{15} m^{-3}$	84
Fig. 7.10. Comparison of (a) average charge at 1000 K and 3000 K (b) average charge at 1000 K and 2000 K (c) distribution of charges formed on a particle as a function for 20 nm and 60 nm particle and $\eta = 1$	86
Fig. 7.11. Electron concentration as a function of temperature for $N_{e(chemi)} = 10^{15} m^{-3}$	88
Fig. 7.12. Electron concentration as a function of electrons produced by chemi-ionization at $N_p = 10^{15} m^{-3}$	89
Fig. 7.13. Electron concentration as a function of total particle concentration at $N_{e(chemi)} = 10^{15} m^{-3}$	90
Fig. 7.14. Electron concentration as a function of particle diameter for $N_p = N_{e(chemi)} = 10^{15} m^{-3}$	91
Fig. 7.15. Ion concentration as a function of (a) temperature for a fixed $N_{e(chemi)} = 10^{15} m^{-3}$ (b) electrons from chemi-ionization for a fixed $N_p = 10^{15} m^{-3}$	92
Fig. 7.16. Ion concentration as a function of (a) total particle concentration fixed $N_{e(chemi)} = 10^{15} m^{-3}$ and (b) particle diameter for $N_p = N_{e(chemi)} = 10^{15} m^{-3}$	94

Fig. 8.1. Schematic of (a) straight chain (b) branched chain agglomerates.	96
Fig. 8.2. Comparison of capacitance of straight and branched chain normalized by capacitance of primary particles.....	98
Fig. 8.3. Comparison of previous experimental (Ball and Howard, 1971) and numerical results.	101
Fig. 8.4. Comparison of net charge formed on an agglomerate as a function of the number of primary particles for zero chemi-ionization.	103
Fig. 8.5. Comparison of net charge per particle of an agglomerate as a function of the number of primary particles for zero chemi-ionization.....	104
Fig. 8.6. Comparison of net charge formed on an agglomerate as a function of the number of primary particles for zero thermal-ionization at (a) 1000 K (b) 3000K.	105
Fig. 8.7. Comparison of net charge formed on an agglomerate as a function of the number of primary particles for zero thermo-ionization (a) 1000 K (b) 3000K.	106
Fig. 8.8. Comparison of relative charge for straight chain and branched chain agglomerates with zero chemi-ionization.	107
Fig. 8.9. Relative electron concentration as a function of number of primary particles.	108
Fig. 8.10. Comparison of relative charge for straight chain and branched chain agglomerates with zero thermal-ionization.	109
Fig. 8.11. Comparison of charge on a primary particle as a function of particle diameter for (a) $N_A=50$ (b) $N_A=100$ (c) $N_A=200$ (d) $N_A=300$	111

1 Introduction

A hydrocarbon flame is characterized by complex chemical kinetics. It is beneficial to study the formation of different species and their effect on the flame chemistry. In addition to the neutral species a typical flame produces a small amount of charged particles, i.e. ions and electrons. These particles not only play a role in the numerous ion and ion-molecular reactions but also play an important role in reaction pathways that generate soot and aerosols. It has been known for many decades that an electric field can deflect the flame. This effect is attributed to the formation of charged particles. In an external electric field, these particles can form ion wind which in turn deflects the flame. Ions are also formed in many ignition processes like spark ignition and laser ignition. Nowadays, there has been widespread interest in understanding of ion and electron formation for engine diagnostics. Hence studying the electrical composition of a flame has innumerable benefits.

1.1 Ions and electrons in flames

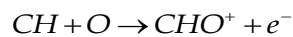
1.1.1 Ionization in flames

1.1.1.1 Hydrocarbon flames

Initially it was thought that the thermal ionization was the primary source of the high concentration of ions and electrons in a combustion process. Calcote (1957) critically reviewed the idea of production of ions by thermal ionization due to different species. In the review, it was mentioned that impurities with low ionization potential can produce ions from thermal ionization in a hydrocarbon flame (Fig. 1.1). Reaction

intermediates like OH, CH and NO have been suggested for the possible sources of thermal ionization. But on careful study it was seen that the measured high ion concentration in flames could not be explained by the low concentration of ions produced due to thermal ionization at those flame temperatures. Carbon particles with a work function between 4.35 eV and 11 eV in the form of solid and gaseous particles respectively have been considered as a possible source for thermal ionization by Perkins et al. (1962). But on further investigation it was found that the ions were produced in the green-zone of the flame where the soot was not as prominent as in other regions of the flame.

Charged species in flames have been studied extensively in the past and have been reviewed by Fialkov (1997). Especially laminar premixed flames have been studied extensively for charged species chemistry. It was found by Calcote (1957) that the primary cause of ion production could be the chemi-ionization reaction. A chemi-ionization reaction is a chemical reaction which produces charged species from neutral reactants. The primary chemi-ionization reaction was determined by Calcote (1961):



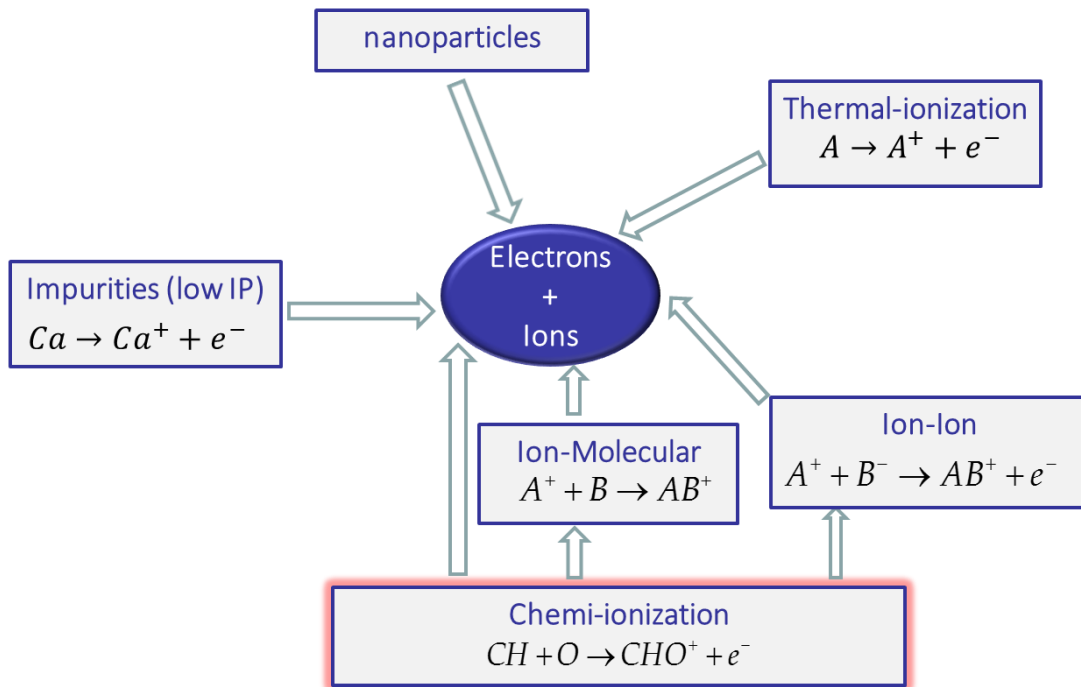
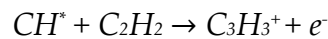
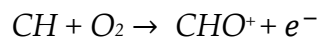


Fig. 1.1. Sources of ions and electrons in flames.

This reaction is negligibly dependent on temperature and it has been proved comprehensively that this is the most dominant source of ionization. The second most important chemi-ionization reaction was suggested by Knewstabb and Sugden (1960):



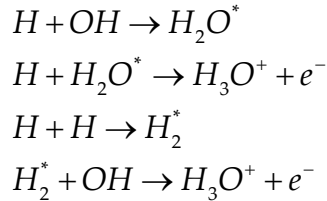
Unlike CHO^+ , it was shown experimentally $C_3H_3^+$ is the most important species with highest concentration in fuel rich flames. Other important chemi-ionization reaction suggested by Burke et al. (1963) was:



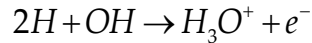
1.1.1.2 Ionization in non-hydrocarbon flames

Low concentrations of charged species are found in pure hydrogen flames. The high concentration of ions found in hydrogen flames are purely because of impurities (Bascombe et al., 1962).

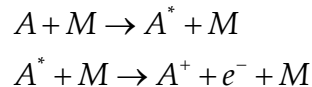
The following mechanism is proposed for pure hydrogen flames (Axford et al., 1998):



Overall chemi-ionization reaction is given by



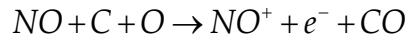
For a hydrogen flames with additives like metals and halogens, a large concentration in ions and electrons is observed. This is because of the high temperatures and high amount of radicals present in a hydrogen flame i.e. H, OH and O. The number of ion and electrons due to thermal ionization can be estimated by using Saha equation given in Chapter 5. The pathway of production of charged species due to alkali metals is given as follows (Padley and Sugden, 1962; Kelly and Pradley, 1969)



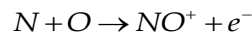
For nitrogen containing fuels (Bulewicz and Padley, 1963) ion concentration in cyanogen-oxygen flames is very high and is at par with that observed in hydrocarbon

flames. The thermal ionization mechanism has very little to do with the ionization even though the temperatures reached are of the ~4000 K.

The following ionization mechanisms was proposed:



For very hot flames atomic nitrogen reacts with an oxygen atom to produce a positive ion and an electron as given by



1.1.2 Ions in methane- oxygen flames

The types of ions produced in a flame vary according to mixture composition. But still there are many common ions produced even for very dissimilar chemical compositions. In all cases it has been found that ion concentration is usually of the same order of magnitude as the electron concentration. The most common ions found in methane-oxygen flames other than electrons are CHO^+ , H_3O^+ , $C_2H_3O^+$, OH^- , O_2^- and O^- though the anions are present in very small quantities.

The ionic chemistry of methane-oxygen flames at atmospheric pressure were successfully studied by Sugden et al. (1979) and Goodings et al. (1979). Methane – oxygen flames were also studied at low pressures by Feugier and van Tiggelen (1965). When the flame is highly fuel rich (Goodings et al., 1977) at 1 atm, the total ion and

electron concentration were found to be $4 \times 10^{10} \text{ cm}^{-3}$. At this condition, large amounts of $\text{C}_2\text{H}_5\text{O}^+$ and C_3H_3^+ were also observed.

1.1.3 Electric field effects

It has been known for decades that electric fields affect the shape and behavior of flames and also the soot particles (Brande, 1814). This means that there has been strong evidence since many years for the presence of charged species as well as particles in a flame. Harnessing this property could mean that the shape and hence the heat and mass transfer properties of the flames could be controlled. There have been studies on the modification of flame speed by using electric fields since many years (Guenault and Wheeler, 1931). Scalov and Socolic (1934) concluded that the speed of hydrocarbon flames decreased with increase in traverse DC electric field.

Electric fields can cause increase or decrease in the formation of soot and also can change the nature of growth and morphology of soot (Place and Weinberg, 1966).

1.1.4 Numerical models

The number of numerical studies performed to study the electron and ion formation have been limited. One study looks at the effect of external electric field on stoichiometric and lean premixed methane-oxygen flame at atmospheric pressure but the negative ions were neglected in the study (Pedersen and Brown, 1993). Also it incorporates only a 13 step chemi-ionization reaction and a fewer number of ions. A more recent study was made by Prager et al. (2007) on a lean to atmospheric methane-

oxygen laminar premixed flame which successfully demonstrates the more detailed ionic chemistry and transport model. Unfortunately, not many studies have been performed on diffusion flames which are more applicable to real combustion systems.

1.2 Nanoparticle charging

Recently, there has been a widespread interest to nanoparticle charging especially in material synthesis, electrostatic filtration of particles and particle control (Schaeublin et al., 2011 and Muzino, 2000). Hence, it has become very important to understand the mechanism that governs the charging of nanoparticles under different conditions. With no external electric field nanoparticle charging is mainly governed by diffusion of charge carriers that are produced from chemi-ionization and electrostatically interact with particles. Another mechanism involves thermal ionization at high temperatures (Savel'ev & Starik, 2006; Sgro et al., 2010). A considerable number of theories have been put forward to describe the diffusion charging mechanism. As shown in Fig. 1.2, there are multiple ways for a particle to acquire a charge in a flame.

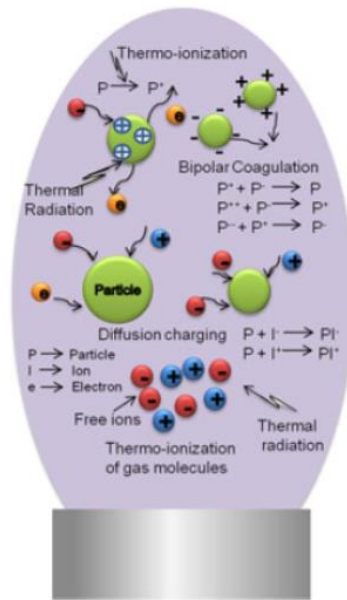


Fig. 1.2. Schematic of various nanoparticle charging mechanisms (Sahu et al, 2012).

A theory on stationary charge distribution on a spherical particle in a bipolar environment has been widely accepted and verified (Fuchs, 1963). Wersborg et al. (1973) reported that one third of soot particles greater than ~2 nm are charged while Mayo & Weinberg (1970) reported that all soot particles formed in a counterflow diffusion flame are charged.

1.2.1 Charging mechanisms

A good amount of experimental work has been performed recently on measuring charge distribution of nanoparticles in flames. Maricq (2005 & 2006) experimentally studied a charge distribution on soot particles in laboratory premixed flames by using

sampling methods coupled with DMA analyzer and compared the results with theoretical equilibrium predictions. Sahu, Park & Biswas (2012) measured charge distribution on TiO₂ and Cu-TiO₂ nanoparticles introduced in a diffusion flame. A comprehensive model has been developed by Jiang, Lee & Biswas (2007) which describes the nanoparticle charging for a soft X-ray enhanced electrostatic precipitator (ESP) device. The model included simultaneous diffusion, thermal ionization and photoionization. A model on charging and growth of soot particles has also been studied by Savel'ev & Starik (2006) without considering high temperature thermal ionization and chemi-ionization.

The charge deposited on a particle can affect the growth of the particle and its structure including fractal shapes of aggregates formed under certain conditions (Onischuk et al., 2008). Charging is extremely sensitive to the ion and electron concentrations around a nanoparticle, temperature as well as the material of the particle. There have been little or no studies on charging of particles in oxy-fuel flames where thermal ionization becomes the dominant charging mechanism due to flame temperatures reaching 3000 K.

Wen et al. (1984) reviewed a number of theoretical approaches to describe charging of arbitrary shaped particles. They introduced the notion of a charging-equivalent diameter into the Boltzmann expression and found it to provide a good approximation to the general theory of Laframboise and Chang (1977) for the charging of soot particles. Rogak and Flagan (1992) further examined the effect of morphology by comparing the neutral fractions of spherical versus aggregate particles leaving a diffusion charger. They concluded that aggregate and spherical particle charging was very similar, observing only a 5% lower neutral fraction for

aggregates for particle diameters between 100 nm and 800 nm. Very recently, Lall and Friedlander (2006) introduced the idea of “idealized aggregates” to calculate the surface area of particles with low fractal dimension. In a two-step approach they make a series of approximations to relate aggregate morphology to mobility, but then they also adopt the method of Wen et al. (1984) to calculate the aggregate’s charging efficiency. Owing to the current interest in combustion aerosols it is, therefore, worthwhile to re-examine the extent to which the bipolar charging of spherical and aggregated particles may differ.

1.2.1.1 Bipolar diffusion charging

Soot particles in a bipolar ion atmosphere are charged by capturing gaseous ions. In the absence of an external electrical field this mechanism is believed to be mainly governed by diffusion of charge carriers and their electrostatic interaction with the particles. A time dependent charge distribution is eventually reached within the particle no matter whatever is the initial charge on the particles after times of the order of $t = \frac{1}{4\pi e(nZ)}$ as shown by Gunn (1955). The diffusion charging models can be divided into two groups. One is the extension of gas kinetic theory to the collision of particles that leads to Boltzmann charge distribution. The other model is based on time independent ion diffusion flux toward a sphere which must be determined for each of the particles charge levels.

The Boltzmann charge distribution model appears to be describing the charge distributions in a satisfactory way down to particle diameters of less than 0.1 μm . Below about 0.06 μm the Boltzmann formula increasingly underestimates the

charging probabilities. Below that diameter Fuchs model is in better agreement with the experimental results as shown by Reischl et al. (1983). Due to the simplicity of its expression it is the most popular distribution function. The characteristic feature of the steady state approximation is the assumption of a vacuum boundary layer of thickness λ near the surface of the particle in which kinetic theory of gas applies. The primary difference between the various models lies in the details of the motion and capture of the ions in the vicinity of the particle.

Boltzmann distribution -

The electrostatic energy contained in the Coulomb field of a sphere in vacuum is

$$\varepsilon_v = \frac{v^2 e^2}{2a} \quad (1.1)$$

$$N_v = N_0 \exp\left(-\frac{\varepsilon_v}{kT}\right) \quad (1.2)$$

where v is the number of unit charges on the sphere, N_0 is the concentration of the neutrals.

Steady-state ion diffusion theory in the continuum limit -

For a sphere at rest with respect to its environment, the transport of ions outside the transition layer is governed solely by the diffusion equation modified for the electric force arising from the free charge carried by the sphere. The ion flux I transported across a spherical shell of radius r in unit time is

$$I = 4\pi r^2 \left(D \frac{dn}{dr} + EZn \right) \quad (1.3)$$

where D is the ion diffusion coefficient, dn/dr is the radial concentration gradient of ions at the shell, Z and n are electric mobility and ion concentration. When we solve Eq. (1.3) we get a solution for $n(r)$.

1.2.1.2 Charging from thermal ionization

Thermal ionization occurs inside the sooting region of the flame. The equilibrium concentration of the thermoionized charged species with a single positive charge is given by Saha's equation

$$\frac{n_e^2}{(n - n_e)} = \frac{2}{\Lambda^3} \frac{g_1}{g_0} \exp\left(\frac{-A_1}{k_b T}\right) \quad (1.4)$$

n_e is the electron number density, n is the neutral particle number density, g_1 is the degeneracy of the states of the 1st ion, g_0 is the degeneracy of the state of the neutral species, A_1 is the ionization potential and T is flame temperature. Thermal de Broglie wavelength Λ can be found as

$$\Lambda = \frac{h}{\sqrt{3mk_b T}}$$

The ionization potential for the small species is given by

$$A_1 = A_w + e^2 / 2C \quad (1.5)$$

where A_w is the work function of the substance making up the particle, e is the electron charge, C is the capacity of the particle equal to $2\pi\epsilon_0 d$ for a sphere of a diameter d .

Mayo and Weinberg (1970) found that soot particles usually carry a single charge. Others reported that the smallest soot particles in a low pressure flame carry a single

charge which could be positive or negative. Doubly positively charged particles were only found in really hot C_2H_2 - O_2 flames as studied by Homann and Wolf (1983). Calcote (1957) found that soot particles larger than 3 nm are formed as a result of thermoionization but smaller particles are not. This is because the recombination coefficient exceeds the rate of thermal ionization for larger particles to neutralize them. Gerhardt et al. (1988) reported that the thermal ionization of particles with diameter greater than 2 nm did not match with the experimental data. But a good agreement was found for particles greater than 3 nm in diameter. Wesborg et al. (1973) reported that one third of soot particles greater than about 2 nm are charged while Mayo and Weinberg (1970) reported that all soot particles in a counterflow diffusion flame are charged.

Balthasar et al. (2002) computationally modeled thermoionization in premixed and diffusion flames by considering the oxidation of fuel, the formation and growth of polycyclic aromatic hydrocarbons, and particle inception, coagulation, as well as mass growth via surface reactions. They found that thermoionization is insignificant for laboratory flames under 2100 K. Over that temperature it can play an important role. The work function of the soot particle also decreases tremendously with the increase in diameter which is primarily due to agglomeration. Hence the tendency to thermally ionize increase with particle size.

Thus it can be said that although it may be intuitive to think that soot particle thermoionization is the primary source of charge on soot, it is clear that there are other processes that are mainly responsible for soot charging unless the temperature is very high. Soot charging is a complex process which depends on a variety of factors like

sooting zone, type of fuel, temperature, pressure, height above the burner and particle size.

1.2.2 Effect of particle morphology on charging

Recent work in this area is directed towards nanoparticles charging and the comparison of experimental data to models of diffusion charging for example by Hoppel et al. (1986). But the influence of morphology on particle charging has had relatively little attention. It was supposed that Coulombic interactions may play a considerable role in the aggregation process and affect essentially the aggregate morphology as studied by Onischuk et al. (2008) and few others. It was shown that soot aggregates formed in flame are charged. Onischuk et al. (2008) later studied the morphology of soot in a propane/air diffusion flame to correlate the Coulombic interactions and the soot structure. It was determined that Coulombic interactions play an important role in soot deposition to the wall resulting in dendrite structure formation at the surface. He found that Coulombic interactions may affect considerably the aggregate–aggregate sticking process. This influence was demonstrated by changing the orientation and by accelerated mutual approach when sticking. An effect of soot aggregate restructuring resulting in transformation of chain-like aggregates to compact structures was observed during the coagulation at room temperature.

1.3 Thesis Objectives

The first part of this thesis is to study the ions and electrons experimentally and numerically in a one-dimensional laminar counterflow oxy-fuel diffusion flame. Experimentally the species are measured using a Langmuir probe by measuring volt-ampere characteristics (VAC) at different positions in the flame. Appropriate theory is used to interpret these curves so that we can calculate the charged species concentrations to validate the numerical results. Then numerically the charged species are computed using a counterflow flame model. Electron and ion profiles are studied for different strain rates and oxygen contents.

The second part of this study is to analyze the interaction between ions, electrons and nanoparticles in a hydrocarbon flame. To achieve this, a basic model was developed that describes the physics governing the charge formation on a spherical nanoparticle as well as its effect on the population of ions and electrons and vice versa in oxygen enriched flames. The model includes diffusion charging and charging of a nanoparticle from thermal ionization in the presence of ions and electrons produced in a flame by chemi-ionization. In order to validate the model the numerical results under certain conditions were compared to the available experimental and numerical results from the literature. This model was extended for fractal agglomerates.

2 Experimental study

2.1 Diffusion / Nonpremixed flame

As the name suggests, in a diffusion or a nonpremixed flame the fuel and the oxidizer are not mixed like the premixed flames before they burn. The reaction occurs due to the diffusion of fuel. In a diffusion flame after diffusing into the flame zone the fuel and oxidizer burn at around stoichiometric conditions. Since real life combustion systems are generally of this kind, we chose to study diffusion flames instead of their counterpart.

Diffusion flames can be produced and stabilized using various configurations which can be 1-D, 2-D or axisymmetric. We chose to select the 1-D counterflow flame configuration for reasons described in Section 2.1.1.

2.1.1 Counterflow flame

A laminar counterflow diffusion flame was used for the investigation of ions and electrons using a set of two opposed flow jets, as shown in Fig. 2.1. It is a widely used diffusion flame configuration to study the ionic chemistry of flames due to it being one-dimensional, low buoyancy and easy to control the parameters of the flame (Ombrello et al., 2006; Ombrello et al., 2008; Kee et al., 1988). It consists of two jets, oxidizer and fuel and the diffusion flame is formed between the two coaxial nozzles. The jets could be surrounded by a shroud which is usually an inert gas like N_2 . A stagnation plane which is a plane where the momentum of the two streams balance

with each other. The flow can be approximated as one dimensional at the axis of the jets.

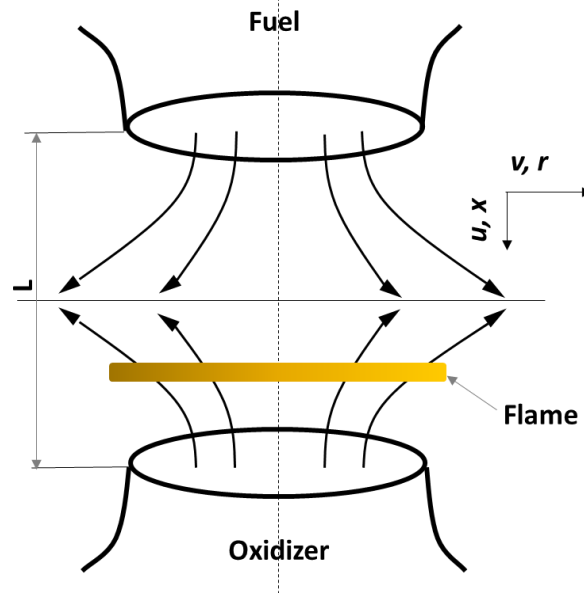


Fig. 2.1 Schematic of a laminar counterflow diffusion flame.

Counterflow flames are characterized by a parameter called the strain rate s which locally is defined as the change in velocity over the change in distance. Assuming the oxidizer and the fuel velocities are equal, the global strain rate is defined as follows:

$$s = \frac{2U}{L} \quad (2.1)$$

where U is the velocity of the fuel and the oxidizer stream at the exit of the nozzle and L is the distance between the two nozzles. The strain rate can be thought of as inverse of the residence time take by the two streams. As mentioned earlier the global strain rate is based on oxidizer and fuel exit velocity and not on local flow velocities which makes it useful to characterize multiple experimental conditions, i.e., flow rate, nozzle diameter and the axial distance by one parameter, i.e., strain rate. A comprehensive information about the counterflow diffusion flames is available in Tsuji, (1982).

2.1.2 Burner configuration

To stabilize a counterflow diffusion flame we use a burner configuration with two opposed nozzles. Fuel which is methane in this case runs from the top and oxidizer which is oxygen enriched air runs from the bottom, as shown in Fig. 2.2. The two streams collide and the flame is ignited manually using an acetylene torch at the location where the two jets meet. The mixing chamber which carries the oxidizer is filled with glass beads. Between the oxidizer and the fuel nozzle there is a concentric annular space through which nitrogen is passed to act as a shroud in order to protect the flame from external perturbations as well as to prevent oxidizer and the fuel to spill outside which can be hazardous. The nitrogen is passed through a ceramic honeycomb to have a stable and a laminar flow. The upper nozzles is surrounded by a cooling system which is a cylindrical jacket also concentric to the two nozzles to cool the exhaust gases. The distance between the two nozzles is fixed at 2 cm. The top part of the burner is mounted on a sliding system and can be traversed in the vertical direction using a motor relative to the bottom burner which is fixed. The supply lines

for all the gases except for air are connected to their individual cylinders and pressure regulators, flow meter and flow controllers are used to monitor and control the flow.

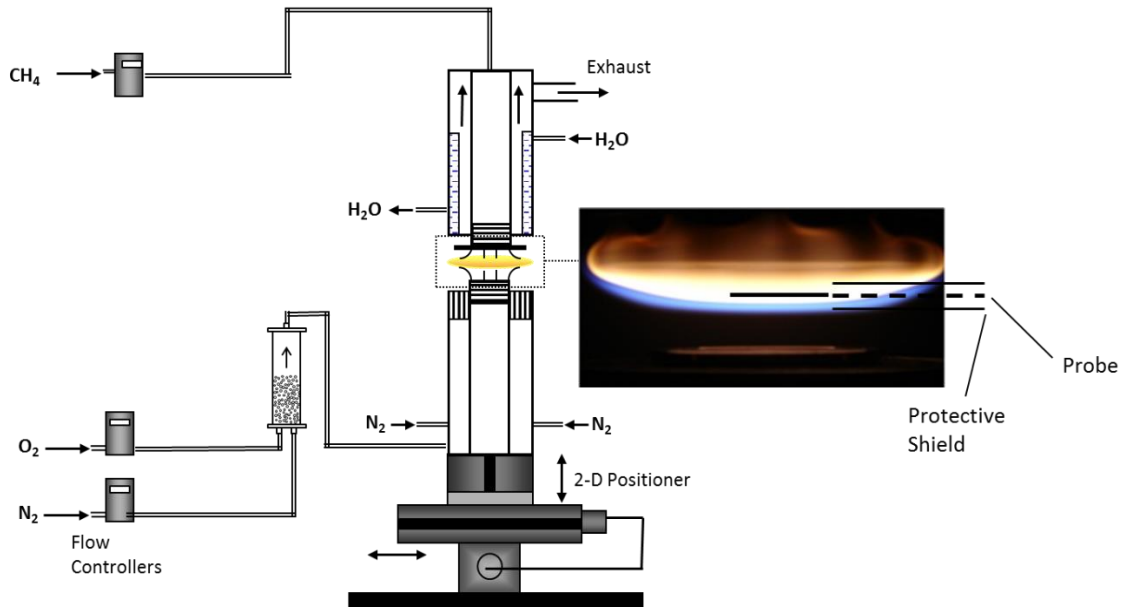


Fig. 2.2 Schematic of the counter flow diffusion flame burner (Desai, 2010).

Compressed air comes in from the in-house compressor and it is mixed with oxygen in the mixing chamber to control the oxygen to nitrogen ratio. Further information regarding the burner set up and the burner operation procedures can be found elsewhere (Salkar, 2011).

2.2 Electric probe

2.2.1 Langmuir probe theory

Langmuir probe is an intrusive technique to measure electrical properties of the flame. The different properties that could be measured are electron temperature, conductivity, mobility, and electron and ion concentration. In this study we focus our attention at recording volt-ampere characteristics (VAC) by using an electric probe. The formulation of the theory to measure concentrations from VAC can change depending on the plasma conditions. The probes could be either of spherical or cylindrical shape. For one dimensional flat flames like a counterflow diffusion flame, a cylindrical probe is best suited.

The experimental setup to measure VAC is shown in Fig. 2.3. First we performed experiments with a 0.25 mm tungsten probe. We call the first probe configuration as P1 which is used here. Later a hollow steel probe (P2) for reasons described in section 2.2.2 is used by making some additional modifications to P1. The tungsten probe is surrounded by a high temperature resistant ceramic tube. We get the VAC curves by changing the potential of the probe with respect to the oxidizer nozzle, treating that nozzle as a ground electrode. The probe is connected to an ammeter in series with a 24 V battery and a 10 K Ω potentiometer is used to change the potential. Also the probe is mounted on a fixture and has the capability to traverse in the axial direction.

The electric current drawn from a flame depends on the probe length and the probe diameter but the current density would be constant irrespective of the probe geometry. When the probe is highly positive it attracts electrons and repels positively charged ions. At such conditions, a thin layer around the probe becomes full of

electrons. Hence there is an electric field in the thin layer near the probe. There is no electric field outside the layer since the plasma is quasineutral. Hence in this case the current measured is the electron saturation current, as shown in Fig. 2.4.

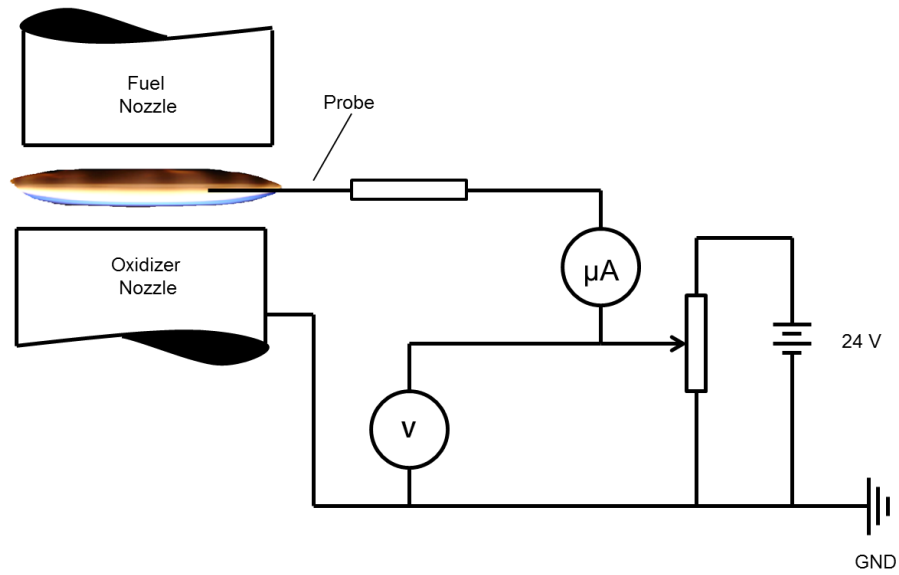


Fig. 2.3. Schematic of the Langmuir probe measurements for P1.

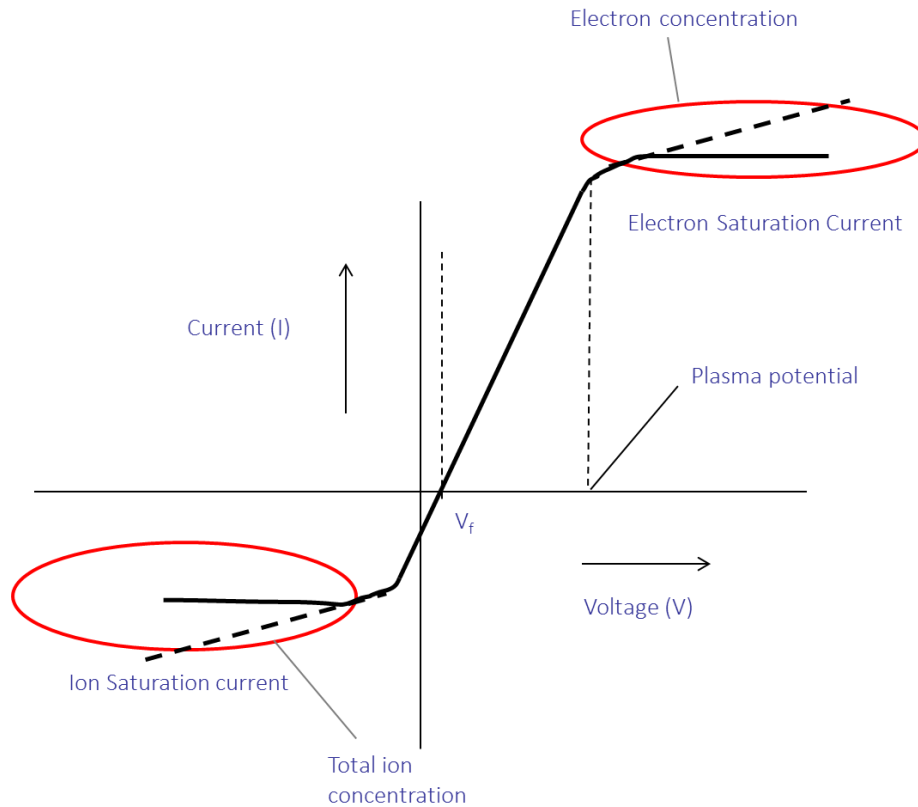


Fig. 2.4. Typical VAC of a single Langmuir probe.

When the probe potential is reduced below the plasma potential, more positive ions and less electron enter the probe. This process continues until the potential of the probe equals the floating potential V_f at which the ion and electron currents to the probe balance each other and the total current of the probe is equal to zero. At this potential the ion current equals the electron current. When the probe potential is strongly negative as compared to the plasma, the positive ions are attracted but the electrons are repelled. In this case the probe is surrounded by a layer of positive ions and the saturation ion current is reached. Even though saturation currents can be

reached for positive ions and electrons at high negative and positive potentials, electrons and ions can enter the probe from other parts of the flame causing an increase in current. So from Fig. 2.4 it can be seen the saturation current is not truly constant but it has a small slope. Hence we are interested in the value of the current at which the slope of the VAC curve drops. Also it can be seen that the ion saturation current is much lower than the electron saturation current due to the high difference in masses.

From the saturation current ' I ' we can determine the current density if we know the probe area by the relation:

$$I = jS_A = j \cdot \pi dL \quad (2.2)$$

where j is the current density and S_A is the surface area of the probe exposed to the plasma, d is the probe diameter and L is the length. The interpretation of the curve varies depending on the application. For low pressure and temperature plasma systems the following equation assuming Maxwell-Boltzmann distribution is often used (Lochte-Holtegreven, 1968 and Clements, 1978):

$$j = \frac{1}{4} en_e u_e = \frac{1}{4} en_e \left(\frac{2k_b T_e}{\pi m_e} \right)^{\frac{1}{2}} \quad (2.3)$$

where e is elementary charge, k_b is the Boltzmann constant, T_e is the electron temperature, m_e is the electron mass, n_e is the number density of the electrons and u_e is the thermal velocity of electrons. From Eqs. (2.2) and (2.3) the electron concentration can be determined.

Similarly ion concentration ' n_i ' can be determined from the following relation:

$$j = \frac{1}{4} en_+ u_+ = \frac{1}{4} en_+ \left(\frac{2k_b T_+}{\pi m_+} \right)^{\frac{1}{2}} \quad (2.4)$$

where the subscript '+' stands for positive ions. The floating potential can also be determined by equating the ion and electron currents, making the net current equal to zero

$$\frac{1}{4} en_e \left(\frac{2k_b T_e}{\pi m_e} \right)^{\frac{1}{2}} \left(\frac{-eV_f}{k_b T_e} \right) = \frac{1}{4} en_+ \left(\frac{2k_b T_+}{\pi m_+} \right)^{\frac{1}{2}}$$

Assuming quasineutrality, i.e., $n_e = n_+$, gives the solution for V_f as:

$$V_f = \frac{k_b T_e}{2e} \left(\frac{T_e m_+}{T_+ m_e} \right) \quad (2.5)$$

For flames, $T_e = T_+ = T$, where T is the flame temperature.

Hence

$$V_f = \frac{k_b T}{2e} \left(\frac{m_+}{m_e} \right) \quad (2.6)$$

The above equations work well when the temperature of the plasma is low and the pressure is way below atmospheric. But for high temperature and atmospheric pressure conditions present in our flame we have to use a modified version of the equation that relates current density and number density for cylindrical probes (Calcote, 1963)

For electron number density,

$$n_e = \frac{j_e}{e} \left(\frac{2\pi m_e}{k_b T_e} \right)^{\frac{1}{2}} \left[1 + \frac{0.75d}{2\lambda_e} \ln \left(\frac{L}{(0.5d) + \lambda_e} \right) \right] \quad (2.7)$$

For ion number density;

$$n_+ = \frac{j_+}{e} \left(\frac{2\pi m_+}{k_b T_+} \right)^{\frac{1}{2}} \left[1 + \frac{0.75d}{2\lambda_+} \ln \left(\frac{L}{(0.5d) + \lambda_+} \right) \right] \quad (2.8)$$

where, λ_e and λ_+ represent the mean free paths of the electrons and ions, respectively. We use the following values for parameters in Eqs. (2.7) and (2.8) to calculate the concentrations for electrons and ions (Table 2-1). The mass for the ion is assumed to be that of the hydronium ion, i.e. H_3O^+ , since that is the most abundant ion found in hydrocarbon flames (Fialkov, 1997).

Table 2-1. Parameters to calculate the ion and electron concentrations for probe configuration P1.

Quantity	Value
m_+	$3.15 \cdot 10^{-26}$ kg
m_e	$9.1 \cdot 10^{-31}$ kg
d	0.25 mm
L	101 mm
λ_+	$5.26 \cdot 10^{-5}$ cm
λ_e	$1.9 \cdot 10^{-4}$ cm

The values for the mean free paths for ions and electrons are taken from Calcote (1963). These values are pressure and temperature dependent and the conditions present in Calcote (1963) are also nearly similar to our conditions hence it is reasonable to assume those values for our calculations. The temperatures used are the flame temperatures and are not measured but computed as discussed in Chapter 5. VAC

curves for 50 % O₂ and 100% O₂ are shown in Figs. 2.5 and 2.6, respectively. The saturation currents are measured at locations 10 mm and 15 mm from the fuel nozzle for both the cases. We see that the electron saturation current for 50 % O₂ at 10 mm and 15 mm is approximately 1.5 μA and 0.5 μA which when plugged in Eq. (2.7) gives the electron concentrations of $2 \cdot 10^{13} \text{ cm}^{-3}$ and $8 \cdot 10^{12} \text{ cm}^{-3}$ respectively. For 100 % O₂ at 100 mm and 15 mm the saturation currents are $\sim 7.5 \text{ μA}$ and $\sim 5 \text{ μA}$ which when used in the same equation gives $8 \cdot 10^{13} \text{ cm}^{-3}$ and $6 \cdot 10^{13} \text{ cm}^{-3}$, respectively. This agrees reasonably well with classical experiments performed in flames (Fialkov, 1997).

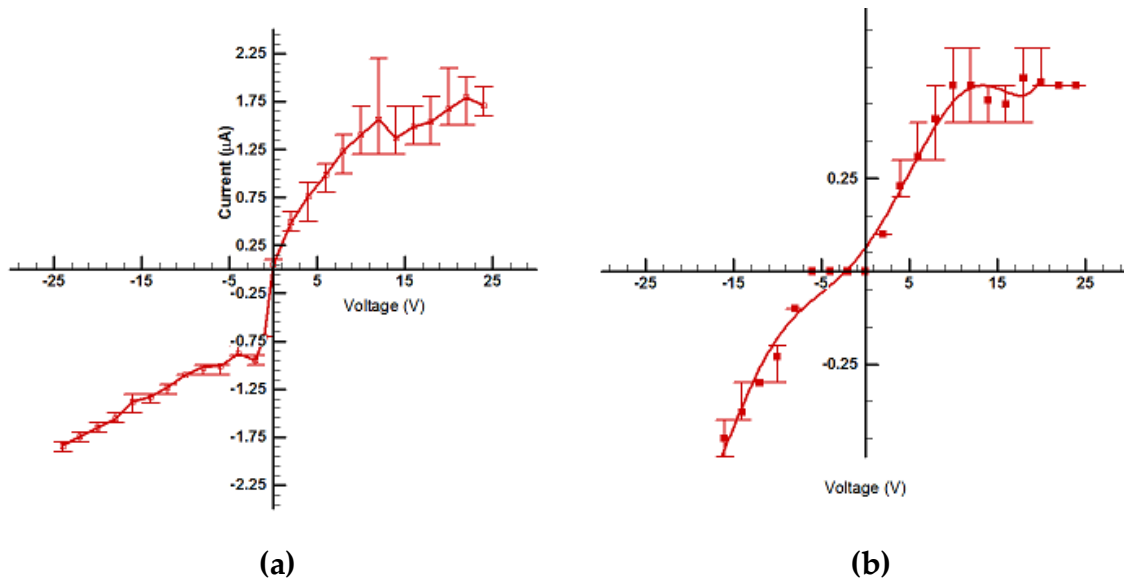
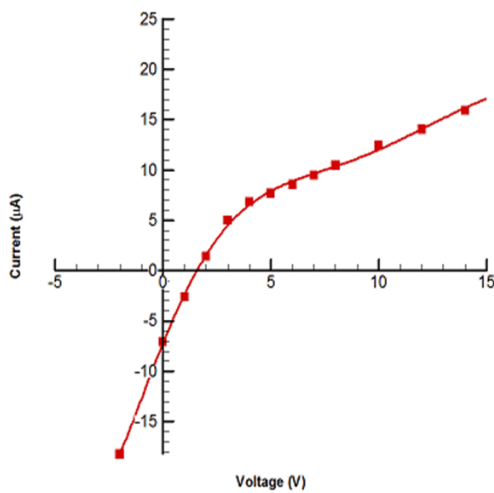
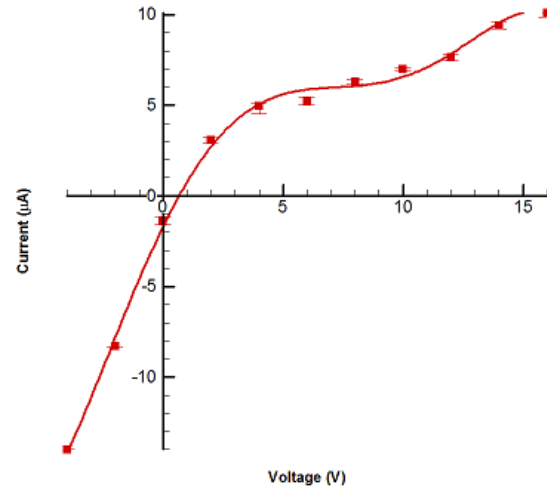


Fig. 2.5. VAC curves with probe configuration P1 for 50% O₂ at (a) 10 mm (b) 15 mm from fuel nozzle.



(a)



(b)

**Fig. 2.6. VAC curves with probe configuration P1 for 100% O₂ at (a) 10 mm
(b) 15 mm from fuel nozzle.**

We only obtain the ion saturation current for 50 % O₂ with an absolute value of $\sim 1 \mu\text{A}$ which corresponds to an ion concentration of $\sim 10^{16} \text{ cm}^{-3}$. This is much higher than expected from Eqs. (2.7) and (2.8) assuming ion concentration is of the same order of magnitude to that of electron concentration. It can be seen that the saturation current does not occur when the oxygen content is increased even though the probe is highly negative. The most probable causes for such anomalies are as follows:

- Due to the high temperature of the flame thermionic emission takes place. So when the probe is at high negative potential with respect to the oxidizer nozzle the electrons released due to thermionic emission are further repelled by the strong negative potential generating the additional current.

- At high oxygen contents the soot generated and the flame temperatures are relatively high as compared to low oxygen contents. Due to this the soot at high oxygen contents gets thermally ionized. This can create a large error in measuring the true ion current when the probe is at negative potential.

Another problem with the above system is that at high temperatures (>1700 K) and at high oxygen content i.e. $> 50\%$ O_2 , the probe gets oxidized making it impossible to measure the currents at certain locations. Hence there is a need to make certain modifications to our probe setup as described in the next section.

2.2.2 Modifications to the probe

The problems associated with the above system can be minimized by cooling the probe. The only feasible way to cool the probe would be through convection. The rate of thermionic emission exponentially increases with the surface temperature of the probe. By cooling the probe internally the thermionic emission can be significantly reduced. Concurrently, the flame disturbances are minimized. Due to the strong temperature effect on thermionic emission rate, even a small reduction in temperature can have a significant effect on the thermionic current.

To minimize the any perturbation in the flame due to the probe, the size of the probe has to be chosen carefully. Hence a tube is chosen which has an outer diameter of 0.9 mm and the inner diameter is 0.7 mm. Due to such small diameters the only feasible manner to cool the probe is to use a gaseous cooling medium instead of liquid due to significantly lower hydraulic resistance and negligible electric conductivity of the gas. Compressed nitrogen at high pressure is passed through the hollow probe. Since the

ion currents are to be of the order of nano amperes, the previous method of measuring current is replaced by Keithley – 6517 A electrometer which can measure currents with very high precision and accuracy of 10^{-12} A, as shown in Fig. 2.7. The results from this probe configuration (P2) are presented in Chapter 5.

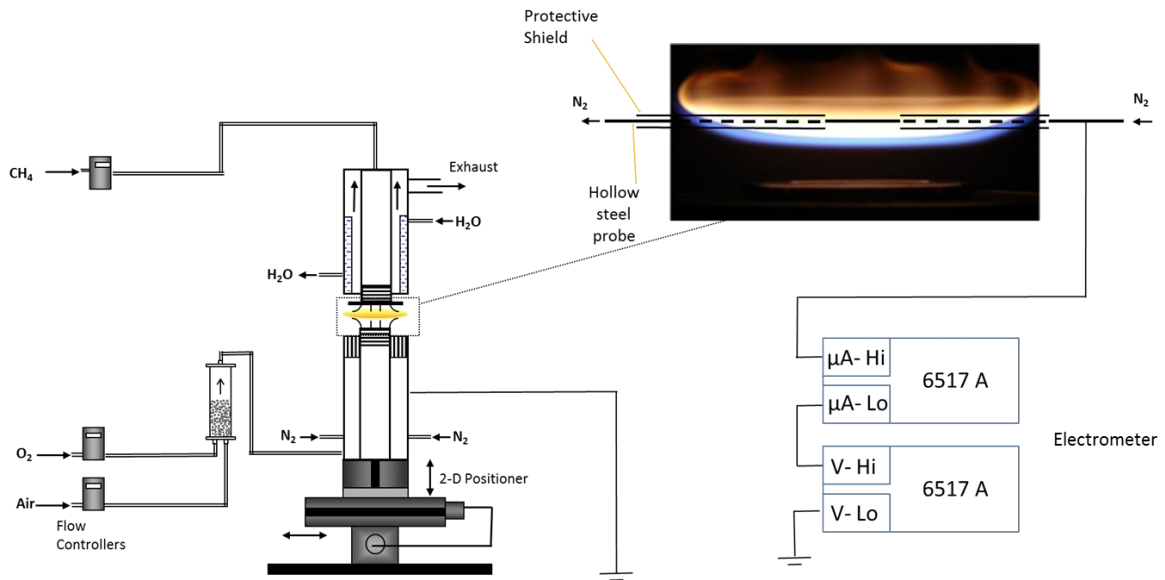


Fig. 2.7. Schematic of the probe with a cooling system (P2).

3 Flame modeling

A one-dimensional counterflow flame model is used to study the ionic structure of the flames. The flame is produced by burning 100% methane (CH_4) with oxygen enriched air and the oxygen content is varied from 21% to 100%. The strain rate of the flame is increased from 20 s^{-1} to 90 s^{-1} in the steps of 10 s^{-1} . The axial distance between the two nozzles is kept at 2 cm.

3.1 Counterflow flame model

The model is solves for the steady state solution for opposed flow diffusion flames axisymmetric and concentric in geometry, as shown in Fig. 2.1. The model is used to predict the mole fractions, mass fractions, velocity and temperature profiles. The model can be used for premixed flames as well, but unlike the diffusion flames, two flames will be produced on the two sides of the stagnation flame.

If we exclude the edge effects, this type of flame geometry is very desirable because the flames produced are flat unlike other types of axisymmetric flames reducing the problem down from two dimensional to one dimensional and making it easier to study the chemistry of the flames.

A brief summary of the model is given below. For more information about the model and its derivation, one can refer to Kee et al., (1988) and Lutz et al. (1997).

The axisymmetric mass conservation equation in cylindrical system is

$$\frac{\partial}{\partial x}(\rho u) + \frac{1}{r} \frac{\partial}{\partial r}(\rho v r) = 0 \quad (3.1)$$

As shown in Fig. 2.1, ρ is the density, u and v are axial (x) and radial (r) components of the velocity respectively.

$$\text{Let, } G(x) = -\frac{\rho v}{r} \quad \text{and} \quad F(x) = \frac{\rho u}{2}$$

After formulating the momentum equation, one can realize that the v/r and other variables like temperature, velocity, density, mole and mass fractions should be a function of the axial distance only (Karman, 1946 and Kee et al. 1988). After plugging in the above expressions into (3.1) one can find

$$G(x) = \frac{dF(x)}{dx} \quad (3.2)$$

Hence,

$$\text{(radial momentum)} \quad H = \frac{1}{r} \frac{\partial p}{\partial r} = \text{constant} \quad (3.3)$$

$$\text{(axial momentum)} \quad H - 2 \frac{\partial}{\partial x} \left(\frac{FG}{\rho} \right) + \frac{3G^2}{\rho} + \frac{\partial}{\partial x} \left[\mu \frac{\partial}{\partial x} \left(\frac{G}{\rho} \right) \right] = 0 \quad (3.4)$$

Energy equation becomes

$$\rho u \frac{dT}{dx} - \frac{1}{C_p} \frac{d}{dx} \left(\lambda \frac{dT}{dx} \right) + \frac{\rho}{C_p} \sum_k C_{pk} Y_k V_k \frac{dT}{dx} + \frac{1}{C_p} \sum_k h_k \dot{\omega}_k = 0 \quad (3.5)$$

Species equation becomes

$$\rho u \frac{dY_k}{dx} + \frac{d}{dx} (\rho Y_k V_k) - \dot{\omega}_k W_k = 0 \quad k=1,2,3,\dots,N \quad (3.6)$$

Where V_k is the diffusion velocity either given by the multicomponent formulation or the mixture averaged formulation.

Mixture averaged diffusion velocity is

$$V_k = -\frac{1}{X_k} D_{km} \frac{dX_k}{dx} - \frac{D_k^T}{\rho Y_k} \frac{1}{T} \frac{dT}{dx} \quad (3.7)$$

Multicomponent diffusion velocity is

$$V_k = \frac{1}{X_k \bar{W}} \sum_{j=1}^N W_j D_{kj} \frac{dX_j}{dx} - \frac{D_k^T}{\rho Y_k} \frac{1}{T} \frac{dT}{dx} \quad (3.8)$$

(mixture averaged)

$$D_{km} = \frac{1 - Y_k}{\sum_{j \neq k}^N \frac{X_j}{D_{jk}}}$$

(multi component)

$$D_{km} = \frac{\sum_{j \neq k}^N X_j M_j}{\bar{W} \sum_{j \neq k}^N \frac{X_j}{D_{jk}}} \quad (3.9)$$

where X_k is the mole fraction, Y_k is mass fraction, C_p is the specific heat capacity, w_k is the molecular weight of the species, \dot{w}_k is the species production or consumption rate, \bar{W} is the mean molecular weight of the mixture, λ is the thermal conductivity of the species, D_{km} is the mixture averaged diffusion coefficient, D_{kj} is binary diffusion coefficient and D_k^T is the thermal diffusion coefficient.

The temperature, composition of the mixture and the velocities are specified at the exit of the nozzles giving the following boundary conditions

$$x = 0: F = \frac{\rho_F u_F}{2}, \quad G = 0, \quad T = T_F, \quad \rho u Y_k + \rho Y_k V_k = (\rho u Y_k)_F$$

$$x = L: F = \frac{\rho_O u_O}{2}, \quad G = 0, \quad T = T_O, \quad \rho u Y_k + \rho Y_k V_k = (\rho u Y_k)_O \quad (3.10)$$

where the subscript 'F' and 'O' stand for fuel and oxidizer respectively.

3.2 Transport properties

The above equations need the values for D_{ij}, D_{km}, D_k^T , viscosities and thermal conductivities so that we can solve them. In order to obtain values of those coefficients we need to find those quantities we need we have an option to use either one of two models, mixture-averaged or multicomponent method. Mixture-averaged quantities easier to compute and take less computational time. But they are less accurate and they may or may not conserve mass in the species equation.

The following gives a brief overview of the method to calculate mixture averaged properties by conventional chemical kinetics package like CANTERA for combustion applications.

Viscosity:

$$\mu_k = \frac{5}{16} \frac{\sqrt{\pi W_k k_b T}}{\pi \sigma_k^2 \Omega} \quad (3.11)$$

where σ_k is the Lennard-Jones collision diameter and Ω is the collision integral which depends on dipole moment and the temperature.

Binary diffusion coefficient:

$$D_{jk} = \frac{3}{8} \frac{\sqrt{\pi k_b^3 T^3 / m_{jk}}}{\pi \sigma_{jk}^2 \Omega} \quad (3.12)$$

where m_{jk} is the reduced mass and σ_{jk} is reduced collision diameter and are given by

$$m_{jk} = \frac{2m_j m_k}{m_j + m_k}, \quad \sigma_{jk} = \frac{2\sigma_j \sigma_k}{\sigma_j + \sigma_k} \quad (3.13)$$

Mixture averaged viscosity:

$$\eta = \sum_{k=1}^N \frac{X_k \eta_k}{X_j \left[\frac{1}{\sqrt{8}} \left(1 + \frac{M_k}{M_j} \right)^{-0.5} \left(1 + \left(\frac{\eta_k}{\eta_j} \right)^{0.5} \left(\frac{M_j}{M_k} \right)^{0.25} \right)^2 \right]} \quad (3.14)$$

Mixture averaged thermal conductivity:

$$\lambda = \frac{1}{2} \left(\sum_{k=1}^N X_k \lambda_k + \frac{1}{\sum_{k=1}^N \frac{X_k}{\lambda_k}} \right) \quad (3.15)$$

For more details regarding the coefficients and also about the multicomponent properties one can refer to Kuo, (1986).

3.3 Ambipolar diffusion

When charged species are included assumption of quasineutrality is used which means at every point summation of all charges are zero. This is only possible if the summation of all diffusion fluxes at that point is equal to zero (Franklin, 2003).

Ambipolar diffusion is the diffusion of positive and negative particles in a plasma at the equal rate because of their interactions with the internal electric field inside a plasma. Since electrons move faster than ions, there will always be a charge separation between ions and electrons hence quasineutrality will not be achieved. The internal electric field accelerates the ions and decelerates the electrons making them diffuse together

Hence we have to make changes to the diffusion flux by introducing ambipolar diffusion (Cancian et al., 2013)

$$j_{k(ambi)} = \rho Y_k \sum_{j \neq e} \frac{Y_j}{X_j} D_{j,m} \frac{dX_j}{dx} + \frac{Y_k E_{ambi}}{k_b T} \frac{dX_e}{dx} \left(q_k e D_{k,m} - \sum_{j \neq e} q_j e Y_j D_{j,m} \right)$$

$$E_{ambi} = \frac{k_b T_e}{q_e e X_e} \frac{dX_e}{dx} \quad (3.16)$$

where E_{ambi} is the internal electric field created.

3.4 Numerical method

The method used is finite-difference approximation for the differential equations. Central differencing scheme is used for the diffusive terms which gives a second order error approximation. Upwind differencing is used for the convective terms and gives first order error approximation with better convergence. To solve the system of equations the TWOPNT (Gracar, 1992) solver is implemented. More information can be found at Lutz et al. (1997) regarding the numerical scheme.

4 Model data

This section contains the source of all the input data used for the simulations and description of reaction mechanism, thermodynamic and transport data.

4.1 Reaction mechanism

The neutral reaction mechanism is based the combustion of lean to stoichiometric methane-air flames which contains 208 reactions with 38 neutral species and describes the chemistry reasonably well (Warnatz et al, 1997). This neutral mechanism was selected because the charged species reaction mechanism used was developed based on this neutral reaction mechanism.

Ions appear in the flame via chemi-ionization reaction. The following is the most widely accepted chemi-ionization reaction especially in stoichiometric flames (Fialkov, 1997; Prager et al., 2007; Speelman et al., 2014)



Even though CHO^+ is the first set of ions produced in a flame it is present in very low quantities and is not the most abundant ion. Thus is because the CHO^+ thus formed from reaction (4.1) quickly undergoes a proton transfer reaction producing H_3O^+ (Prager et al., 2007 and Speelman et al., 2014).



4.1.1 Charged species

The charged species are the ones used by Prager et al. (2007). It consists of eleven charged species, 4 positive ions and 7 negative ions including electrons which are the most abundant ions found in experiments by Goodings et al. (1979) as shown in Table 4-1. In the previous experiments (Goodings et al., 1979) 70% of the net charge was due to 3 of the charged species only in the cold region and about all the net charge in the flame zone and the burnt region.

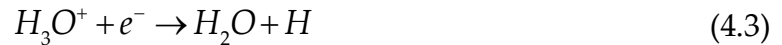
Table 4-1. List of charged species included in the model.

Positive ions	Negative ions
$H_3O^+, C_2H_3O^+,$ CH_5O^+, CHO^+	$e^-, O_2^-, O^-, OH^-,$ CHO_2^-, CHO_3^-, CO_3^-

In addition to the above two major reactions there are 61 more reactions that describe the charged species reaction mechanism of flames which will can be found in Prager et al., (2007). We chose this charged species mechanism because this is the only mechanism that has included negative ions unlike other studies for flames where only the cation chemistry was used (Pedersen et al., 1993). The cation chemistry used in the flame is well established and observed in the experiments by Goodings et al. (1979) and simulations by Eraslan et al. (1988). But the negative ion chemistry is not very reliable and still needs work because the reaction rates used for the negative ion

chemistry are approximated. Hence the uncertainties involved in these reaction rates are a little high.

The recombination reactions are also important due to the high reaction rates. One of the most important recombination reactions is (Belhi et al., 2010 and Speelman et al., 2014):



4.2 Thermodynamic data

The thermodynamic data needed as input in the model are specific heat capacity, entropy and enthalpy. These can be easily found in standard databases (Chase et al., 1985; McBride et al., 2002 and Burcat et al., 2005) for most neutral species with full confidence. Only for O, O₂ and N₂ the properties are taken from Warnatz et al., 2006. Properties for O⁻ and OH⁻ are available in Burcat et al., 2001 and that for e⁻, CHO⁺, H₃O⁺ and O₂⁻ are taken from McBride et al., 2002. Properties for C₂H₃O⁺, CH₅O⁺, CHO₂⁻, CHO₃⁻ and CO₃⁻ are not readily available hence the properties for these molecules are approximated by using values of those molecules that are similar in molecular structure and molecular weight. For example the properties for C₂H₃O⁺ is considered to be those used for neutral C₂H₃O. Since ions present in a flame have a mole fraction of less than 10⁻⁸, their presence does not have a real effect on the flame temperature.

4.3 Transport data

The transport data for neutral species are taken from GRI Mech database. The properties not available for the charged species and some of the neutral species i.e. HCCO, CH₂CHO, CH₂CH₂OH, CH₃O₂H had to be estimated with the properties of similar molecules with available data. Since some of the ionic species didn't have the data for transport properties readily available, we used the properties for those available and whose molecular weights and structures were close to that of the ionic species. The detailed description of the transport properties and the equations in which they are used is given in Section 3.2.

5 Results of the flame experiments and model

5.1 Flame structure

The flame has a unique appearance and structure depending on the conditions. Oxygen content in the oxidizer stream and strain rate have a strong influence on the flame structure.

5.1.1 Effect of oxygen content

Typically a counterflow diffusion flame has two distinct parts as shown in Fig. 5.1. One is the yellow part which is near the fuel side and secondly a blue part which is on the oxidizer side of the flame. The yellow part is rich in carbon content and radiative soot due to fuel rich environment and the blue part is rich in oxygen containing radicals (Glassman, 1989; Tree et al. 2007). It's because the stagnation plane is on the fuel side the soot is found on that side of the flame. Another reason of formation of soot on the fuel side is the lack of oxygen containing radicals. In certain flames, oxygen content and hence the temperature (Fig. 5.2(a)) can have complex effects on soot formation and hence the structure of the flames. Initially the increase in oxygen content will reduce the soot, then increase in oxygen content further increases the soot content due to higher temperatures on the fuel side but incomplete combustion. But with methane-oxygen flames increase in oxygen content causes an increase in soot formation (Refs is required here). The higher the oxygen content the larger is the shift of the more soot peak towards the fuel side because of the shifting

of the stagnation plane towards the fuel nozzle with increase in overall density of the oxidizer, as shown in Fig. 5.2(b).

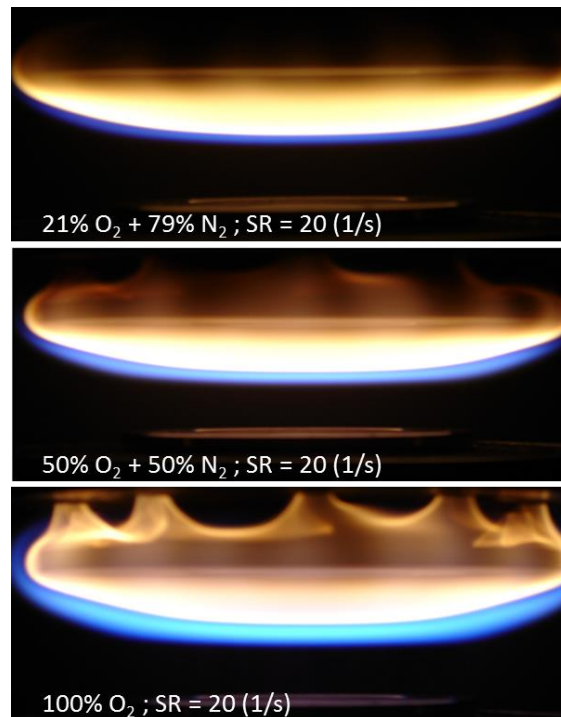
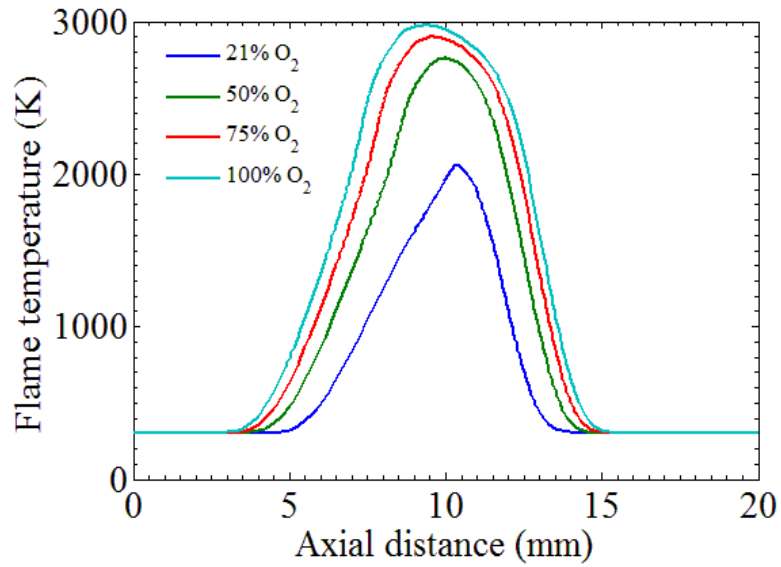
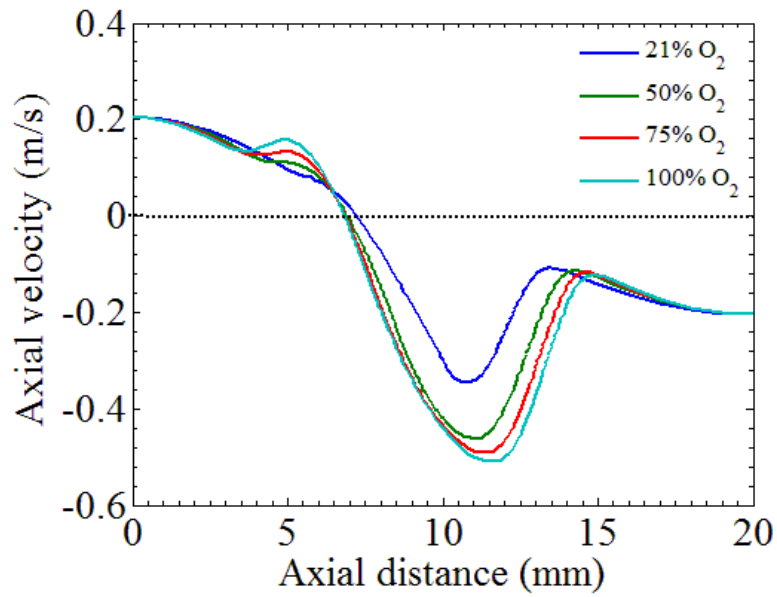


Fig. 5.1. Effect of oxygen on flame structure at 20 s⁻¹ (Desai, 2010).

As the oxygen content increases the distance between the flame and the stagnation plane decreases and fuel consumption increases making the flame much brighter over a larger area, as shown in Fig. 5.2(a).



(a)



(b)

Fig. 5.2. Effect of oxygen content at 20 s^{-1} on the (a) Flame temperature profile (b) axial velocity profile.

5.1.2 Effect of strain rate

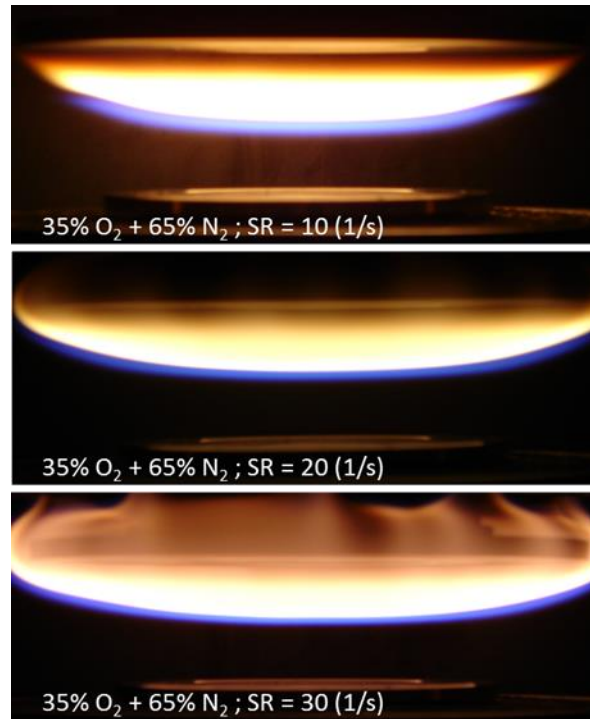
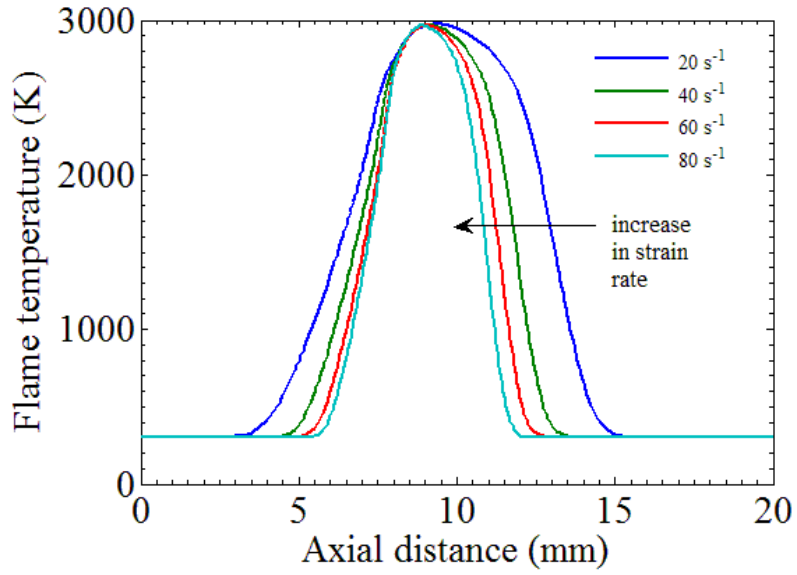
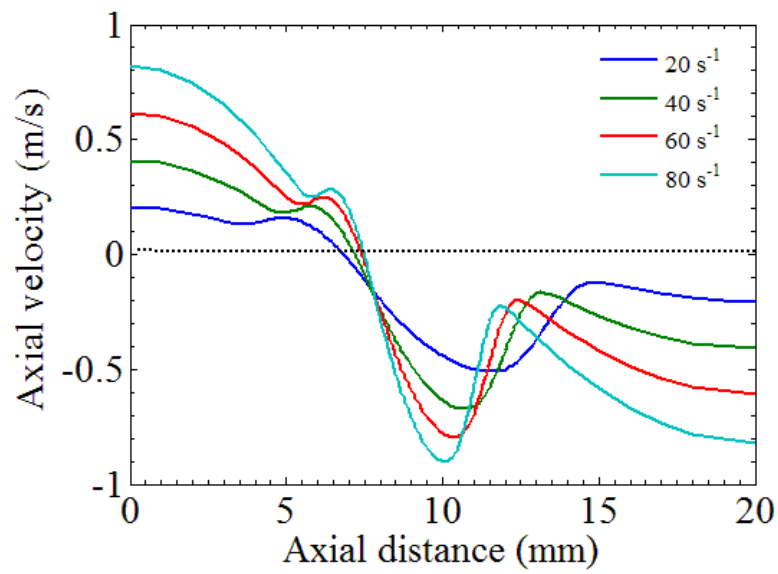


Fig. 5.3. Effect of strain rate on flame structure at 100% O₂ (Desai, 2010).

When the strain rate is low the flame is brighter and distinct. As the strain rate is increased, the flame gets squeezed and hence the flame thickness decreases and curves around the edge of the burner as seen in Figs. 5.3. With strain rate the temperature gradients become larger, as shown in Fig. 5.4(a). With an increase in strain rate, the soot formation is suppressed since the temperature is distributed over a smaller area resulting in lower soot formation.



(a)



(b)

Fig. 5.4. Effect of strain rate at 100 s⁻¹ on the (a) Flame temperature profile (b) axial velocity profile.

5.2 Volt-Ampere (VAC) Characteristics

Volt-ampere characteristics were produced using the modified probe as discussed in Section 2.2.2. VACs were measured at different points in the axial distance between the two nozzles for different oxygen contents and different strain rates. Figure 5.5 shows the VAC recorded for 21 % O₂ at 10mm from the fuel nozzle. The figure clearly shows an electron saturation current at around 1.5 μA and a closer look at the ion saturation current gives a small non-zero current of approximately 8 nA. The curves are then interpreted using the equations describe in Section 2.2.1.

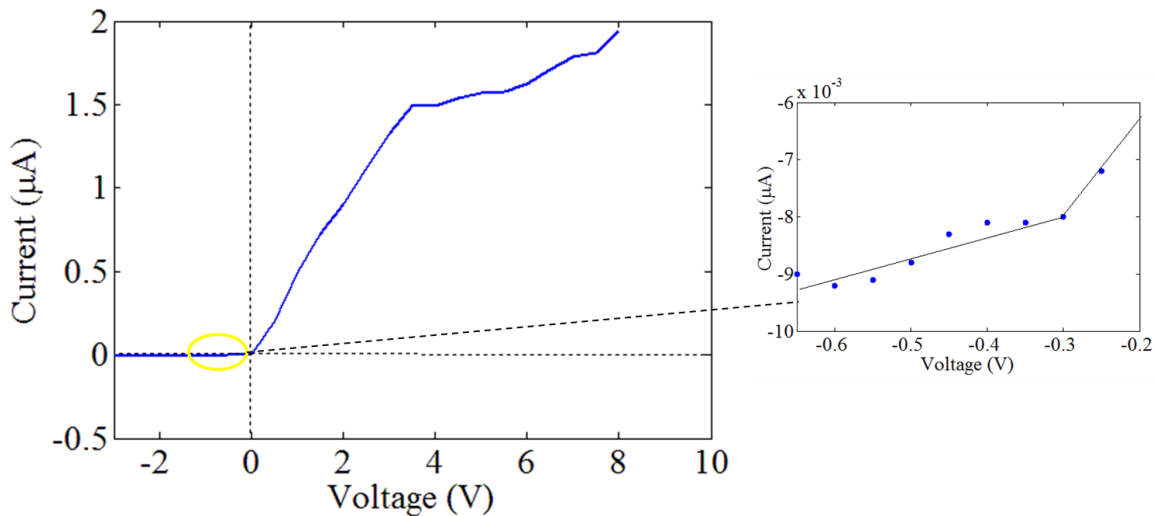


Fig. 5.5. VAC for 21% O₂ at 10 mm from the nozzle to measure electron saturation current ion saturation current.

Figure 5.6 shows the characteristic VAC recorded using the cooled probe configuration (P2) for 75% O₂ and we can clearly see the low ion saturation currents and the electron currents with high precision using an electrometer.

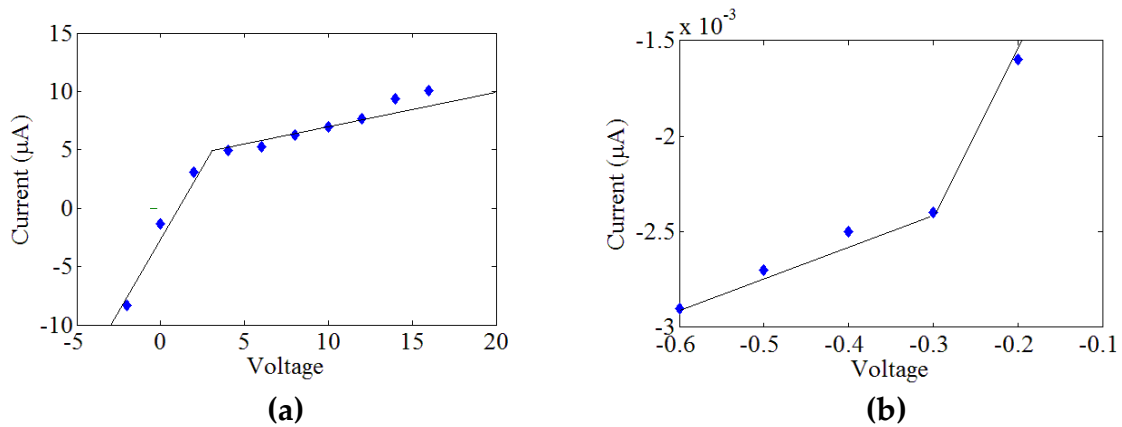


Fig. 5.6. VAC for 75% O₂ at 10 mm from the nozzle to measure (a) electron saturation current (b) ion saturation current.

It can be also noticed that the electron current measured at 75 % O₂ is higher than that with 21% O₂ which is as expected.

5.3 Ion and electron profiles

Figure 5.7 shows the mole fractions of major positive ions and electrons for methane air flame at 20 s⁻¹. The major positive ion produced is H₃O⁺ and the major negative charge carried is electron. Hence the total ion concentration can be assumed to be that

of the hydronium ion. Even though the entire cation and anion chemistry is included in the model it can be seen that the electron is the only dominant negative charge carrier and negligible negative ions are formed in the flame. Even though CHO^+ is the first cation formed via chemi-ionization its concentration is still lower than the hydronium (H_3O^+) ion because once CHO^+ is formed it quickly combines with a water molecule to give the hydronium ion.

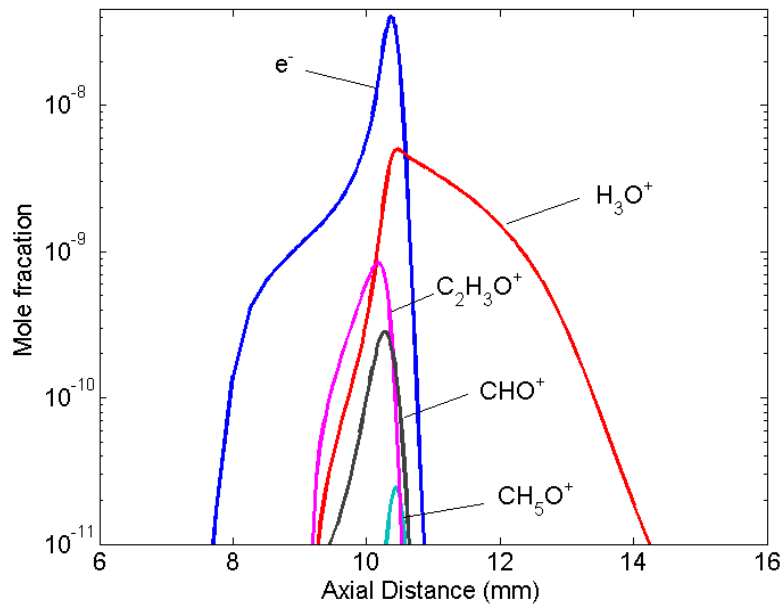


Fig. 5.7 Distributions of major positive and negative ions in a methane –air diffusion flame at 20 s^{-1} .

Using the modified Langmuir probe theory ion and electron concentrations were calculated and compared with the numerical results as shown in Fig. 5.8. One can clearly see the close agreement between the experimental and numerical results. It's also helpful to note that as the oxygen content is increased the peak electron and ion concentration moves towards the fuel nozzle since the flame also moves in that direction as shown in Fig. 5.2 (a).

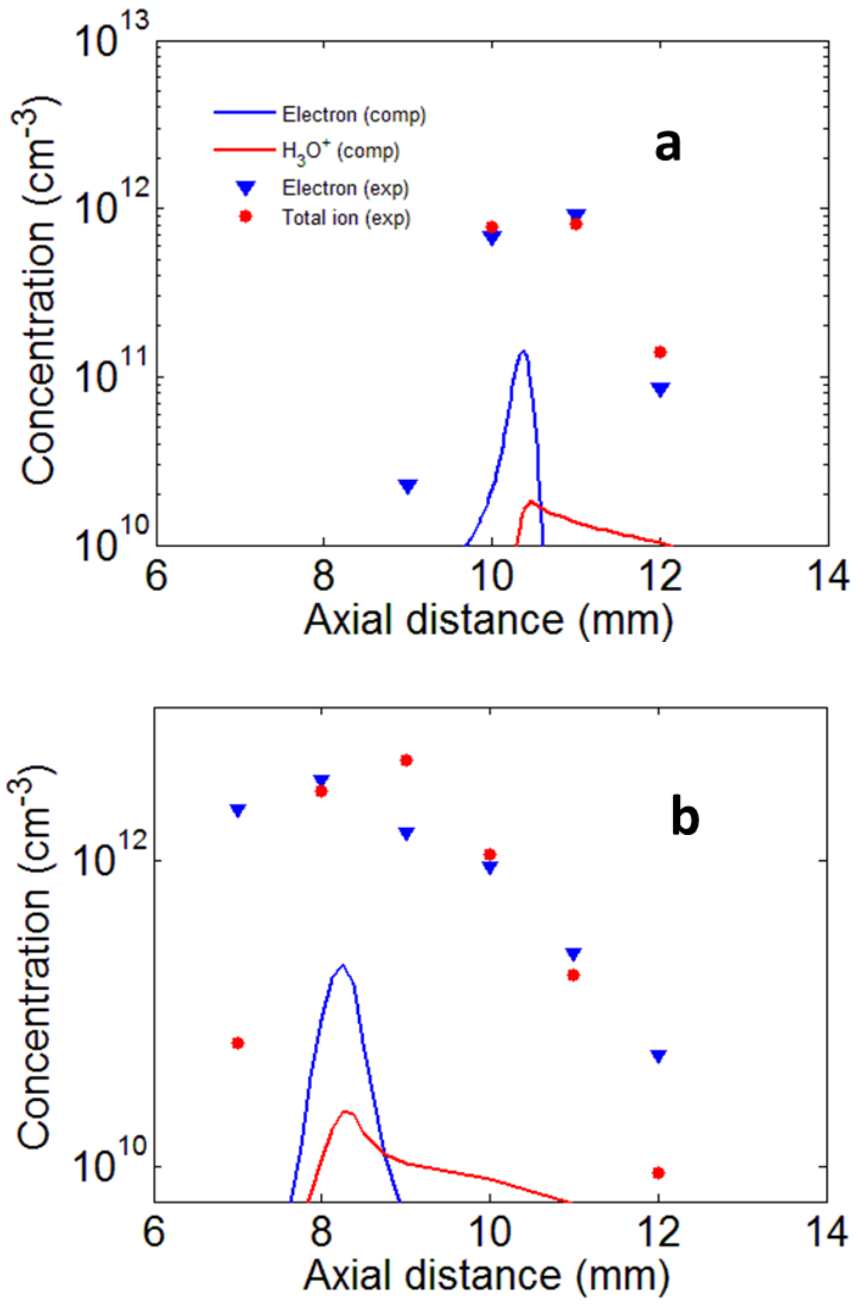
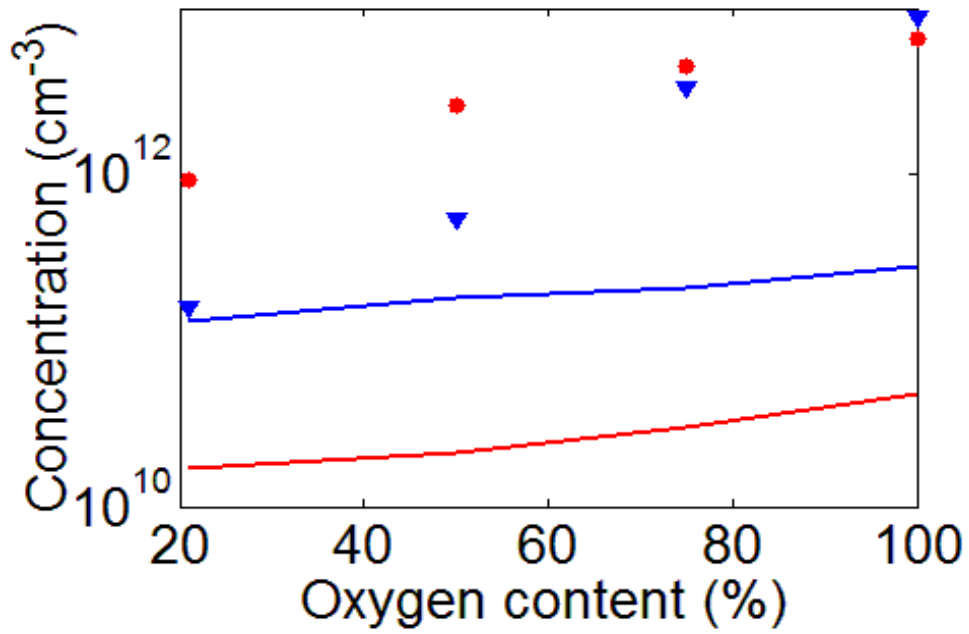


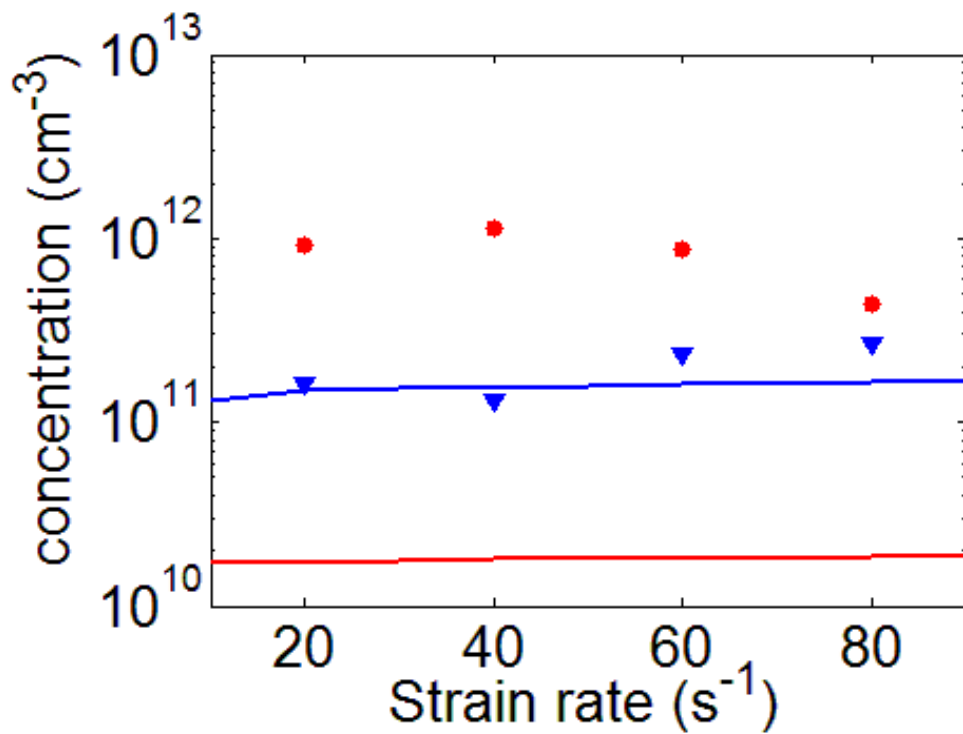
Fig. 5.8. Ion and electron profiles at (a) 21% O_2 (b) 75% O_2 .

5.3.1 Effect of oxygen content and strain rate on peak charged species concentrations

In Fig. 5.9, we can see that strain rate has a very small impact on the peak charged species concentration but oxygen content has a strong influence on charged species concentration. The experimental and numerical results are in close agreement with each other. The peak electron concentration increases as much as by three times and the peak positive ion concentration increases as much as by four times.



(a)



(b)

Fig. 5.9. Effect of (a) oxygen content (b) strain rate on peak charged species concentration.

5.4 Conservation of charge

The charged species in the flame are produced mainly from chemi-ionization reaction which is a reaction where a positive ion and an electron is formed from two reacting neutral molecules. Since we do not consider any particles present in the system, the sum of all charges in the flame should be equal to zero. In other words

$$\sum N_+ = \sum N_-$$

Where N_+ and N_- stand for positive and negative charged species concentrations. Now at the first glance in Fig. 5.8. its not clear whether the charges are conserved. But when the respective areas under the positive and negative species are calculated they turn out to be approximately equal.

5.5 Effect of gas-phase thermal-ionization

The Saha equation for ionization relates the ionization of a species to its pressure and temperature

The equation is as follows:

$$\frac{n_e^2}{(n - n_e)} = \frac{2}{\Lambda^3} \frac{g_1}{g_0} \exp\left(\frac{-\varepsilon}{kT}\right) \quad (5.1)$$

Where:

n_e = electron number density

n = neutral number density

Λ = thermal de Broglie wavelength

g_1 = degeneracy of the states of the 1st ion

g_0 = degeneracy of the state of the neutral species

ε = Ionization potential

T= Temperature

$$\Lambda = \sqrt{\frac{h^2}{2\pi k T m_e}} \quad (5.2)$$

Where:

h = Planck Constant = $6.626 \cdot 10^{-34}$ J·s

m_e = electron mass = $9.1 \cdot 10^{-31}$ kg

k = Boltzmann's constant = $1.38 \cdot 10^{-23}$ m² kg s⁻² = $8.62 \cdot 10^{-5}$ eV/K

From Fig. 5.10 it can be seen that O₂ and H₂O would be the most readily ionizable species as compared to others due to its lowest ionization potential. Hence if we estimate the number of electrons produced due to thermal-ionization for CH₄ -100% O₂ flame we find that the electrons produced by thermal-ionization is much less as compared to that produced from chemi-ionization even though the temperature is close to 3000 K, as shown in Fig. 5.11. Hence we can neglect thermal-ionization when we are trying to compute the charged species concentration in a flame.

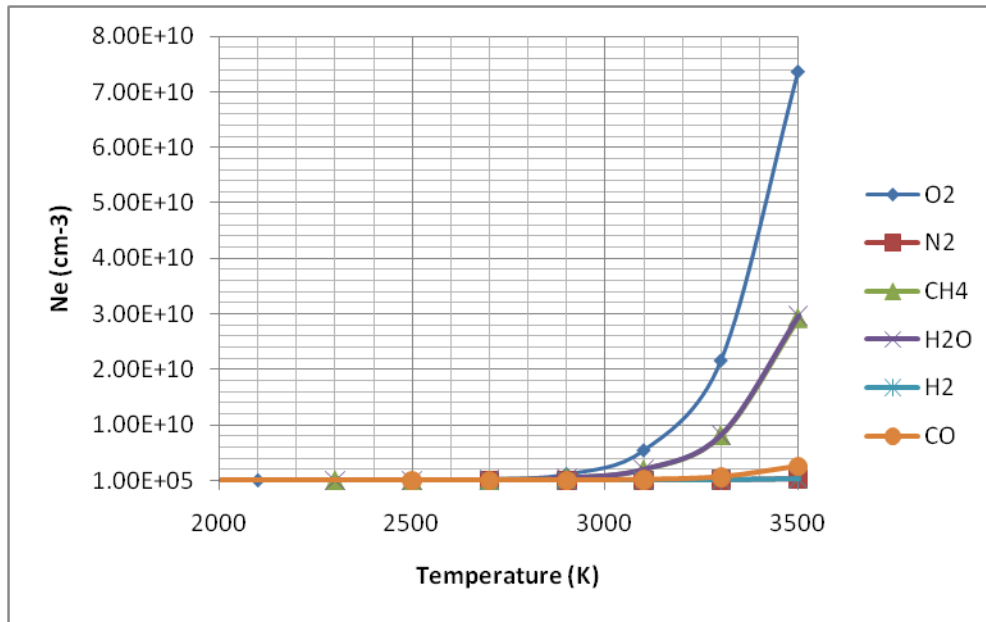


Fig. 5.10. Electron density as a function of temperature from major neutral species in the flame.

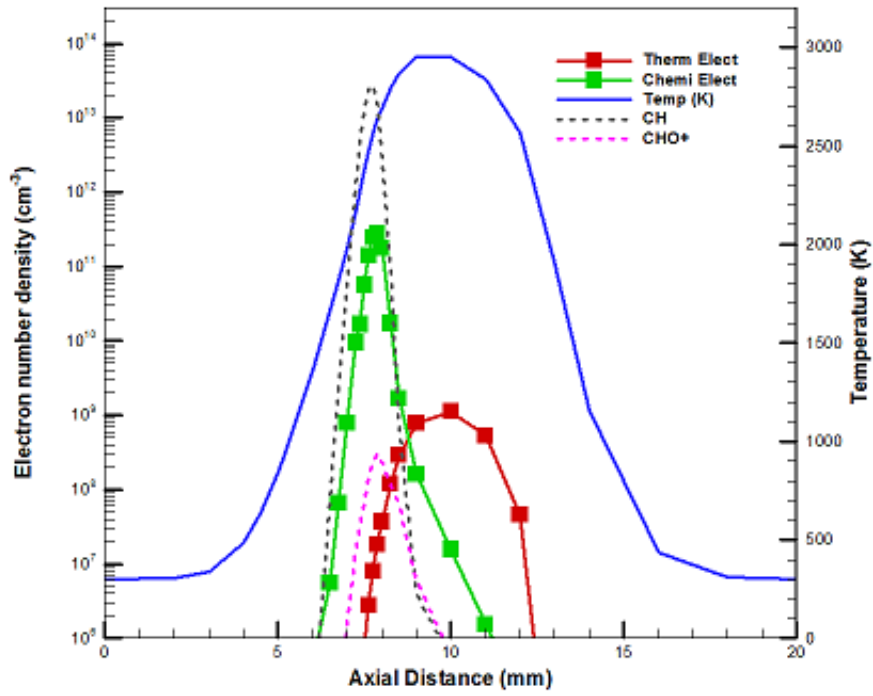


Fig. 5.11. Comparison of electrons produced from thermal-ionization and chemi-ionization.

6 Primary nanoparticle charging model

6.1 Theory and Objective

Particles immersed in bipolar ion atmosphere are charged by capture of ions and electrons due to diffusion even in the absence of external electric field. This is in contrast to field charging wherein charging takes place when ions travel along the electric field lines. For diffusion charging the actual number of charges on a particle undergoing diffusion charging is approximately proportional to the particle diameter. Diffusion charging is one of the primary mechanism to charge submicron particles in any plasma system. A particle introduced in a hydrocarbon flame will also charge due to bipolar diffusion as in the plasma containing both ions and electrons. Ions and electrons collide with particles randomly and deposit a net charge on the particles. Due to the random nature of charge transfer particles charged unequally but there is a distribution of net charge on particles.

The purpose of this study is to analyze the interaction between ions, electrons and nanoparticles in a hydrocarbon flame. To achieve this, a basic model was developed that describes the physics governing the charge formation on a spherical nanoparticle as well as its effect on the population of ions and electrons and vice versa in oxygen enriched flames. The model includes diffusion charging and charging of a nanoparticle from thermal ionization in the presence of ions and electrons produced in a flame from chemi-ionization. In order to validate the model the numerical results under certain conditions were compared to the available experimental and numerical results from the literature.

6.2 Chemi-ionization model

Electrons and numerous types of ions are observed in a flame (Prager et al., 2007; Savel'ev, 2012) such as CHO^+ , C_3H_3^+ , H_3O^+ , $\text{C}_2\text{H}_3\text{O}^+$, CHO^- , O^- , O_2^- and many more depending on the type of the flame, equivalence ratio for premixed flame and the mixture composition. Ions and electrons are generally produced first by the chemi-ionization reaction which is the primary source of ions and electrons in a flame (Calcote). To understand the formation of ions and electrons in hydrocarbon flames many complex chemical mechanisms have been proposed (Prager et al., 2007; Starik et al., 2002; Pedersen et al.; 1993). The composition of ions and electrons in the diffusion flame strongly depends on the oxygen content of the flame.

The chemi-ionization reaction that produces the first set of charged species followed by neutral-charged reactions and charged-charged reactions to generate more ions and electrons is



It is shown (Goodings et al., 1979; Prager et al., 2007) that the major ions produced in a methane-oxygen flame are CHO^+ , H_3O^+ , $\text{C}_2\text{H}_3\text{O}^+$, CH_5OH^+ , OH^- , O_2^- , O^- and CO_3^- . Amongst these ions, hydronium H_3O^+ represents 90% of the population of ions. Hence, in order to simplify the chemistry for our model we can consider the average ionic molecular mass to be that of the hydronium ion and neglect the negative ion population other than the electrons. Also, since reaction (6.1) produces the initial set of ions and electrons we can assume the net rate of ion and electron formation to be equal to the rate of reaction (6.1).

The rate, k at which the ions and electrons are produced is given by the following Arrhenius equation

$$k = BT^n \exp\left(\frac{-E_a}{R_u T}\right) \quad (6.2)$$

where B is the pre-exponential factor, T is the temperature, n is between 0 and 1, E_a is the activation energy and R_u is the universal gas constant. These parameters for chemi-ionization reaction (1) are taken from Prager et al. (2007). The ions and electrons recombine to reach a steady state in a combustion system with a rate k_r . Hence the overall rates of formation $\dot{\omega}_e$ and $\dot{\omega}_+$ for electrons and ions respectively are given by

$$\dot{\omega}_e = \dot{\omega}_+ = \dot{\omega}_{IR} - k_r N_e N_+ \quad (6.3)$$

where $\dot{\omega}_{IR} = k[CH][O]$ is the chemi-ionization rate, N_e is the concentration of electrons, N_+ is the concentration of ions, and k_r is the effective recombination rate describing electron and ion losses in flame. k_r is obtained from Prager et al. (2007) and Goodings et al. (1979) by using known quantities of N_e , N_+ , concentrations of CH and O and plugging them in Eq. (6.3) by substituting $\dot{\omega}_e = 0$. The calculated values of k_r lie between $4.5 \cdot 10^{16} \text{ cm}^3 \cdot \text{mol} \cdot \text{s}^{-1}$ and $8 \cdot 10^{16} \text{ cm}^3 \cdot \text{mol} \cdot \text{s}^{-1}$ for temperatures ranging from 1000 K and 3000 K respectively which is falls within range for the recombination rate for the reaction $H_3O^+ + e^- \rightarrow H_2O + H$ (Prager et al., 2007).

Propensity of a nanoparticle-free flame to form ions and electrons through chemi-ionization can be characterized by a steady state concentrations of ions and electrons, $N_{e(\text{chemi})}$ and $N_{+(\text{chemi})}$. In a nanoparticle free flame ($N_p = 0$) N_e is equal to N_+ and

$N_e = N_{e(chemi)} = N_{+(chemi)}$. Electron concentration $N_{e(chemi)}$ can be used as a parameter in Eq. (6.3) modifying it to the following form:

$$\dot{\omega}_e = \dot{\omega}_+ = k_r (N_{e(chemi)}^2 - N_e N_+) \quad (6.4)$$

The effect of chemi-ionization on nanoparticle charging is further analyzed using the chemi-electron concentration in a nanoparticle-free flame as the model parameter. The ratio of total nanoparticle concentration to chemi-electron concentration at nanoparticle-free flame serves as another parameter which is given by $\eta = \frac{N_p}{N_{e(chemi)}}$.

Electrons are mainly produced from the chemi-ionization reaction (6.1) which is basically a thermoneutral reaction (Calcote, 1957). Hence the production of electrons is governed by the product of concentrations of CH and O only. The temperature in the flame is strongly dependent on the oxygen content relative to the nitrogen content and independent of the charged species concentration (Merchan-Merchan et al., 2003; Prager et al., 2007). Therefore, the effect of chemi-electron concentration and temperature on charging can be analyzed independently.

6.3 Bipolar diffusion charging model

The rate at which the particles capture the ions or the electrons depends strongly on the mobility of the particles and the ion-particle or the electron particle Coulombic forces which could be attractive or repulsive depending on the nature of the potential difference between the ion or the electron and the particle. Van der Waals forces may also be important for particles less than 10 nm in diameter. Irrespective of the initial

charge a time dependent charge distribution is eventually reached within the particle after a characteristic time. When particles are more than 40 nm in diameter the characteristic charge that they acquire is practically independent of the material properties and is only a strong function of particle size and morphology. It is very difficult to determine the rate at which ions or electrons attach to the particles experimentally hence a number of models have been put forth to describe the same. The traditional models describing charging can be split into three parts. The first one is the Boltzmann charge distribution which is the extension of the equilibrium gas kinetic theory, the second being a steady state model formulated for the continuum region and the third one formulated for the free-molecular region. For nanoparticles in atmospheric flames the characteristic length is very small as compared to the mean free path, hence we consider the model for the free-molecular regime.

In a combustion system with no external applied electric field the thermal velocity exceeds the drift velocity tremendously, hence it would be reasonable to assume the drift velocity to be negligible as compared to the thermal velocity.

The flame has ions and electrons moving randomly and freely depending on their individual temperatures and mass. We can assume that a nanoparticle introduced in a chemically reacting ionized gas gets hit by ions and electrons from all directions and gets captured or attached to the nanoparticle. Hence, we can put forth the following equation for the rate at which rate at which electrons diffuse and attach to the nanoparticles with charge z and radius a

$$\Gamma_z^e(z, a) = S_A N_e \frac{v_e}{4} \beta_e \quad (6.5)$$

where v_e is the thermal velocity of the electrons, N_e is the number density of the electrons, S_A is the surface area of the nanoparticle and β_e is the electrostatic interaction coefficient given by Orbital motion limited (OML) theory (Zobnin et al., 2000) for submicron and nanoparticles:

$$\beta_e = \begin{cases} \exp\left(\frac{ze^2}{4\pi\epsilon_0 k_b T a}\right) & z < 0 \\ 1 & z \geq 0 \end{cases} \quad (6.6)$$

And the thermal velocity of the electrons is given by the kinetic theory as

$$v_e = \left(\frac{8k_b T}{\pi m_e}\right)^{\frac{1}{2}} \quad (6.7)$$

The rate at which ions diffuse and attach to the nanoparticles with charge z and radius a is given by

$$\Gamma_z^+(z, a) = S_A N_+ \frac{v_+}{4} \quad (6.8)$$

From the kinetic theory, the average thermal velocity of ions is given by

$$v_+ = \left(\frac{8k_b T}{\pi m_+}\right)^{\frac{1}{2}} \quad (6.9)$$

where m_e and m_+ are the respective masses of electrons and ions.

6.4 Thermal-ionization model

Most of the ions and electrons in a flame appear due to chemi-ionization. But when particles are introduced in a flame they can affect the charged species concentration in the flame due to multiple processes. One of the ways it can be affected is thermal-ionization. The rate at which electrons escape from the particles due to thermal-ionization is strongly material dependent. The rate at which electrons are emitted from a material surface is given by the modified Richard-Dushman equation (Sodha & Guha, 1971) for small particles:

$$\gamma_z(a, z) = \begin{cases} S_A A T^2 \exp\left(\frac{-\phi}{k_b T}\right) & z < 0 \\ S_A A T^2 \left(1 + \frac{(z+1)e^2}{4\pi\epsilon_0 a k_b T}\right) \times \exp\left(-\frac{1}{k_b T} \left[\phi + \frac{(z+1)e^2}{4\pi\epsilon_0 a}\right]\right) & z \geq 0 \end{cases} \quad (6.10)$$

where S_A is the surface area, A is the material dependent constant, ϕ is the work function of that material, k_b is the Boltzmann's constant, ϵ_0 is the vacuum permittivity and e is the elementary charge.

In our model thermal ionization was not considered to be in equilibrium but treated kinetically. The terms A and ϕ are taken from the literature for graphite (Jain et al., 1952) except in Section 7.4.2.1 where ϕ is varied depending on the material. The work-function ϕ corresponds to the minimum amount of energy needed by an electron to overcome the barrier and escape the surface of the material. Also, the larger is the particle, the easier is to thermally ionize it.

6.5 Model formulation and validation

Most of the modeling studies on charging of nanoparticles till now have been performed in a low to mid temperature plasma and flame environment and do not consider the effect of ions and electrons produced at oxygen enriched flame conditions on charging of the particles. Due to the production of ions and electrons in the flame in a high temperature environment we take into account charging due to diffusion, thermal ionization and chemi-ionization in the model. Since ions, electrons and nanoparticles occur simultaneously in a flame; their respective concentrations are influenced by each other until they reach a steady state, as shown in Fig. 6.1. The time required to reach a steady state depends on factors like temperature, total nanoparticle concentration, nanoparticle size and chemi-ionization conditions.

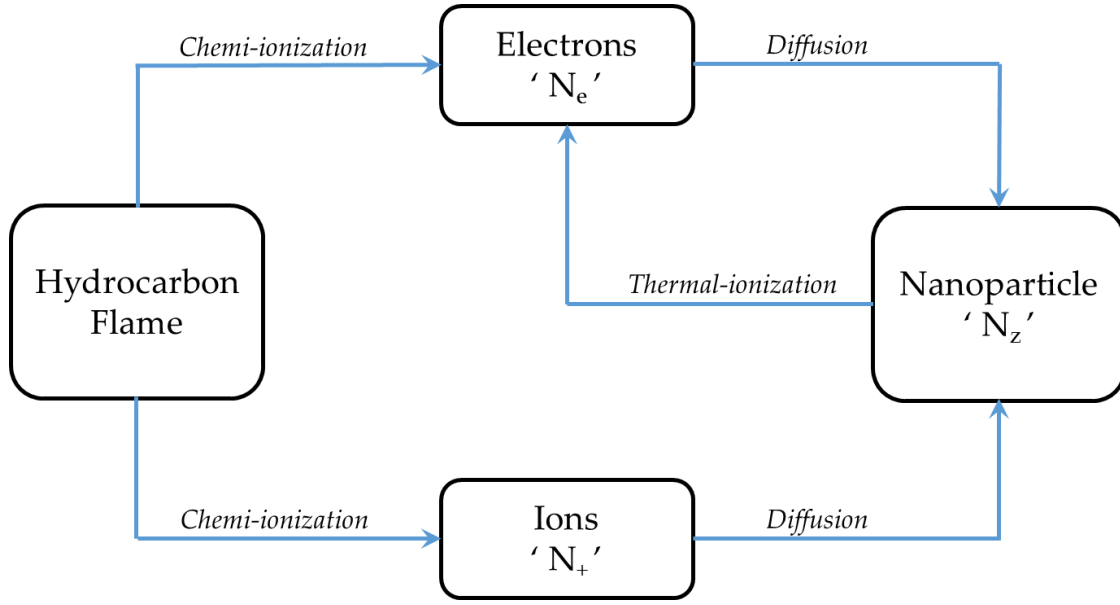


Fig. 6.1. Schematic of the interaction between ions, electrons and nanoparticles in a hydrocarbon flame.

The time-dependent concentration N_z of spherical nanoparticles with a charge z and radius a is given by

$$\frac{dN_z}{dt} = \gamma_{z-1}N_{z-1} + \Gamma_{z+1}^e N_{z+1} - \gamma_z N_z - \Gamma_z^e N_z + \Gamma_{z-1}^+ N_{z-1} - \Gamma_z^+ N_z \quad (6.11)$$

where γ is the thermal ionization rate, Γ is the attachment rate, N_z is the concentration of the nanoparticle with charge z .

The first term in Eq. (6.11) represents the production of particle with charge z due to thermal ionization of a particle with charge $(z - 1)$. The second term describes the generation of a particle with charge z due to the diffusion of electrons to a particle

with charge $(z + 1)$. The third term denotes the loss of a nanoparticle with charge z due to thermal ionization of a particle with charge z . The fourth term indicates again the loss of the particle with charge z due to diffusion of electrons to the same. The fifth and the six terms are responsible for the increase and decrease of the charged nanoparticle due to the diffusion of positive ions to a nanoparticle with charges $(z - 1)$ and z respectively.

The time evolution of electron and ion number density in a flame environment is given by

$$\frac{dN_e}{dt} = \dot{\omega}_e + \sum_{z=-\infty}^{\infty} \gamma_z N_z - \sum_{z=-\infty}^{\infty} \Gamma_z^e N_z \quad (6.12)$$

$$\frac{dN_+}{dt} = \dot{\omega}_+ - \sum_{z=-\infty}^{\infty} \Gamma_z^+ N_z \quad (6.13)$$

Where N_e and N_+ are the electron and ion concentrations respectively.

The first term in Eqs. (6.12, 6.13) describe the net generation or consumption of electrons and ions due to chemi-ionization and volumetric recombination. The second term in Eq. (6.12) denotes the emission of electrons from thermal-ionization. The third term and the second term of Eqs. (6.12) and (6.13), respectively, represent the loss of electrons and ions due to diffusion and recombination of charged species to the nanoparticles with charge z .

Due to the interactions of ions, electrons and nanoparticles Eqs. (6.12-6.13) are integrated over time. The numerical scheme implemented is forward difference Euler method as shown in Appendix A. Since Eq. (6.11) describes particles with a charge z

which theoretically ranges from $-\infty$ to $+\infty$, practically to consider z varying between $-q$ to $+q$, the total number of equations that need to be solved are $(2q + 1)$ for the nanoparticles and in addition one equation for ions and one equation for electrons.

The average charge carried by the particles is given by

$$\hat{z} = \sum_{z=-\infty}^{\infty} f_z z \quad (6.14)$$

Here, f_z is the fraction of the particle with charge z and $f_z = (N_z / N_p)$ with N_p being the total particle concentration. The initial conditions ($t = 0$) used to solve the system of differential equations are

$$N_z(z \neq 0) = 0, N_z(z = 0) = N_p, N_e = 0, N_+ = 0. \quad (6.15)$$

There have been few experimental studies performed (Homann & Wolf, 1983) on evaluating the characteristic charge on soot particles in laboratory flames. To validate our model we use the limited experimental data available as well as a numerical study of Balthasar et al. (2002). The experimental data of Homann & Wolf (1983) were generated by measuring soot sizes and charges on primary soot particles in premixed C_2H_2 and C_6H_6 flames. By using the experimental total nanoparticle concentration and soot volume fraction we can calculate the particle diameter by the relationship $f_v = \frac{1}{6} N_p \pi d_p^3$, where f_v is the soot volume fraction which in turn is used in our model to predict the percentage charged particle distribution at different distances from the burner, as shown in Fig. 6.2. It can be seen that the relative charged particle distribution predicted by the model is in a reasonably good agreement with the experimental results.

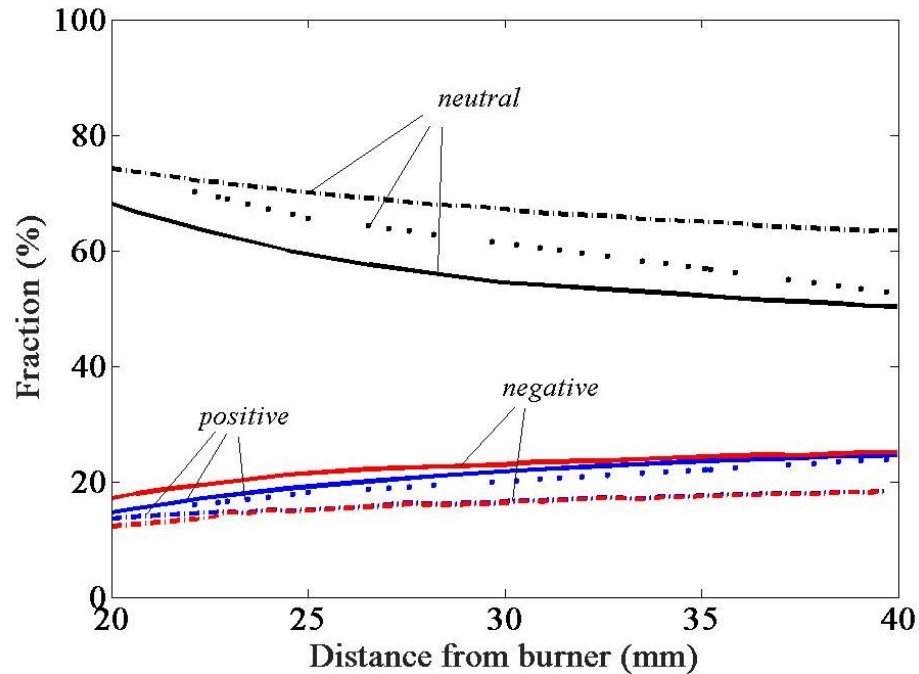


Fig. 6.2. Comparison of relative soot volume fraction: experimental results by Homann and Wolf (1983) (symbols), computed (solid lines) and model by Balthasar et al. (2002) (dashed lines).

The model of Balthasar et al. (2002) under predicts the charged particle distributions, possibly because it does not include the ions and electrons produced due to chemi-ionization and hence the additional effect of diffusion charging is not accounted for. Results for the fraction of charged particles as a function of particle diameter were also compared with the modeling results from Balthasar et al. (2002) (Fig. 6.3) and it was found that the results compare well with the previous modeling results.

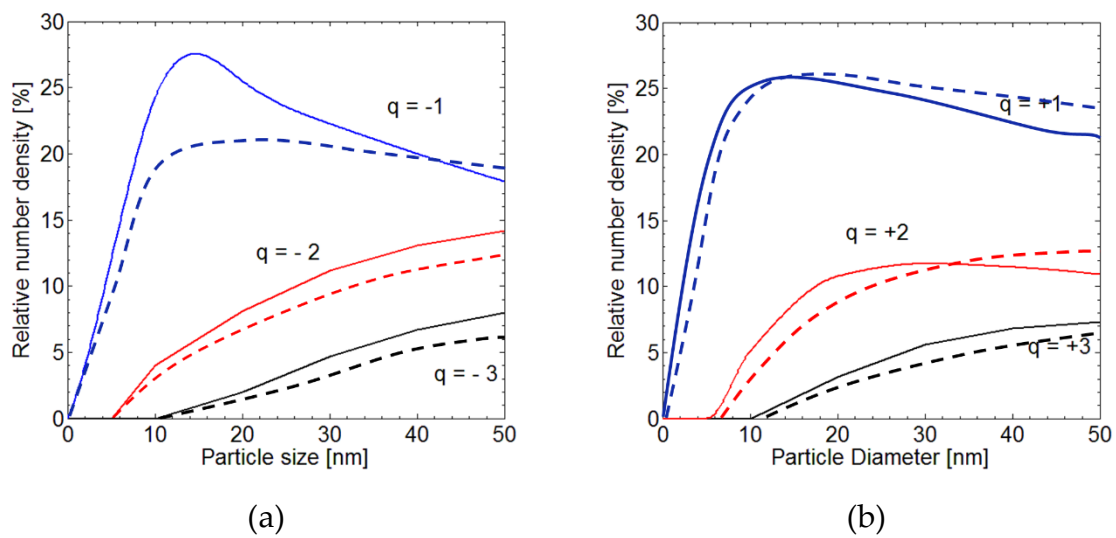


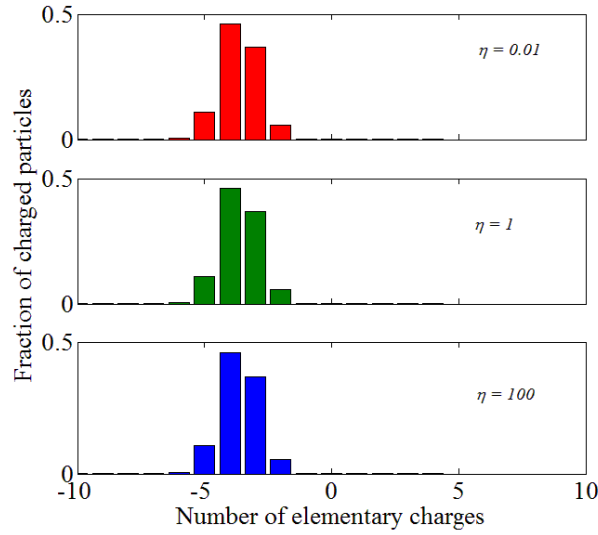
Fig. 6.3. Comparison of relative number density: our modeling results (solid lines) and model by Balthasar et al. (2002) (dashed lines) (a) negatively charged particles (b) positively charged particles.

7 Results of the primary nanoparticle charging model

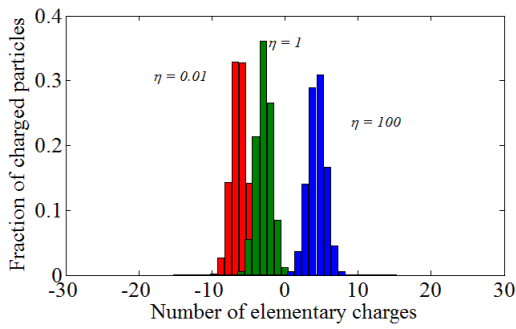
Before considering the model comprehensively, the model was first simplified to analyze the contributions of different processes to the particle charging.

7.1 Fixed ion and electron concentration

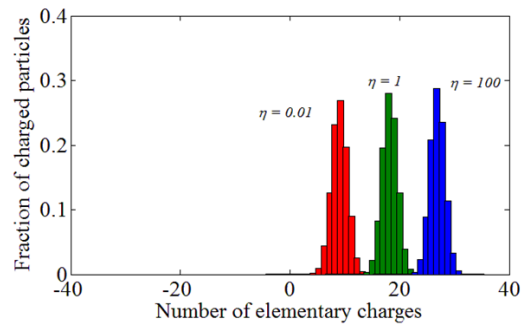
Let us first study the problem by keeping the net ion and electron concentration fixed at 10^{15} m^{-3} . In reality the electron and ion concentrations will be affected by particles in the system but in this section we are assuming a fictitious possibility where the electron and ion concentration can be held constant irrespective of the temperature, nanoparticle concentration or particle diameter. From Fig. 7.1. we can see that 1000 K the particles are equally charged irrespective of η and the average charge is approximately 4 electron charges. But as the temperature is increased to 2000 K and even further to 3000 K, particles convey different behavior for different values of η . At 2000 K and $\eta = 0.1$, each particle has ~ 100 electron charges.



(a)



(b)



(c)

Fig. 7.1. Comparison of fraction of charged particles for fixed total electron and ion concentration at (a) 1000 K (b) 2000 K (c) 3000 K.

The particles become negatively charged due to strong diffusion of electrons towards the nanoparticles in comparison with the heavy ions. As η is increased to 100 the particles become electron deficient and hence the particles become more positively

charged due to the combined effect of thermal ionization and positive ions attaching to the particles. At 3000 K and $\eta = 100$, the thermal ionization becomes the dominant charging process and the thermal ionization rate increases rapidly to make the particles strongly positively charged. Even for $\eta = 0.01$ the particles are positively charged because at such high flame temperatures the diffusion of electrons towards the particles is practically switched off in relation to thermal ionization.

7.2 Zero chemi-ionization

By turning off the source of ions and electrons from chemi-ionization in the model we can evaluate the individual effect of thermal-ionization on the charging of particles, as shown in Fig. 7.2. For fixed $N_p = 10^{15} \text{ m}^{-3}$, when the temperature is 1000 K, the energy acquired by the electrons is not enough to escape from the material surface and hence the thermal ionization rate is zero. Because of this the electrons do not escape from the surface to diffuse towards the particles thus leaving them uncharged. But as the temperature rises to 2000 K some of the electrons acquire energy sufficient for escape from the surface and attaching to small number of particles. Hence in this case about an equal percentage of particles are positively and negatively charged, the remaining 30% of the particles are left uncharged.

But as the temperature is increased to 3000 K, the thermal ionization rate increases exponentially making all the particles positively charged with a mean charge of +13. The electrons are emitted from the particles at a high rate. As a result an equilibrium is reached between highly positive charged particles and the free electrons.

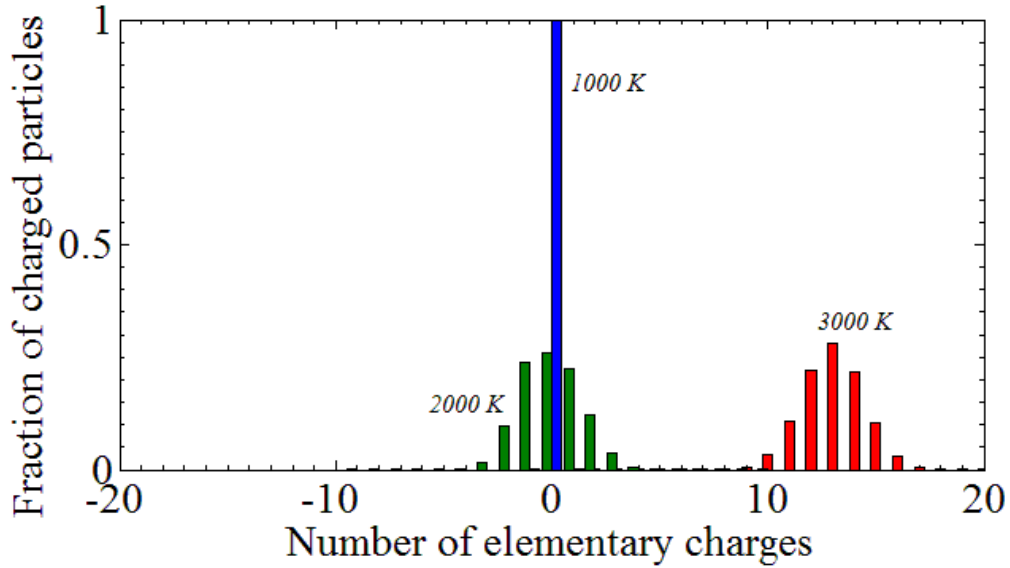


Fig. 7.2. Comparison of fraction of charged particles for zero chemi-ionization.

7.3 Negligible thermal-ionization

To analyze the influence of chemi-ionization we will neglect the thermal ionization terms in the model and keep the nanoparticle concentration fixed at 10^{15} m^{-3} . In Fig. 7.3, the distribution of charges on particles is compared at different temperatures as well as different nanoparticle concentrations to electrons produced from chemi-ionization (η) by assuming the thermal ionization rate equal to zero. In Figs. 7.3 (a-c) we can see that at $\eta = 100$, the particles get charged negligibly. As η is decreased to 1, particles get negatively charged, the effect becoming more pronounced with temperature. The reason being, as the temperature is increased the thermal velocity of the electrons is increased. As a result, more electrons are deposited on the particles

due to the additional kinetic energy available to overcome the electrostatic barrier. We see the particles get more negatively charged when η is equal to 0.01 because of the excess of electrons available in the flame environment.

Even though there is an equal number of ions and electrons considered in the model, the particles become negatively charged. This is because the mass of the hydronium molecule is $3.4 \cdot 10^4$ times the mass of an electron, the thermal velocity of the electrons is more than 180 times that of the ions. Hence, the probability of an electron attaching to the particles is 180 times higher to that of an ion making them only negatively charged.

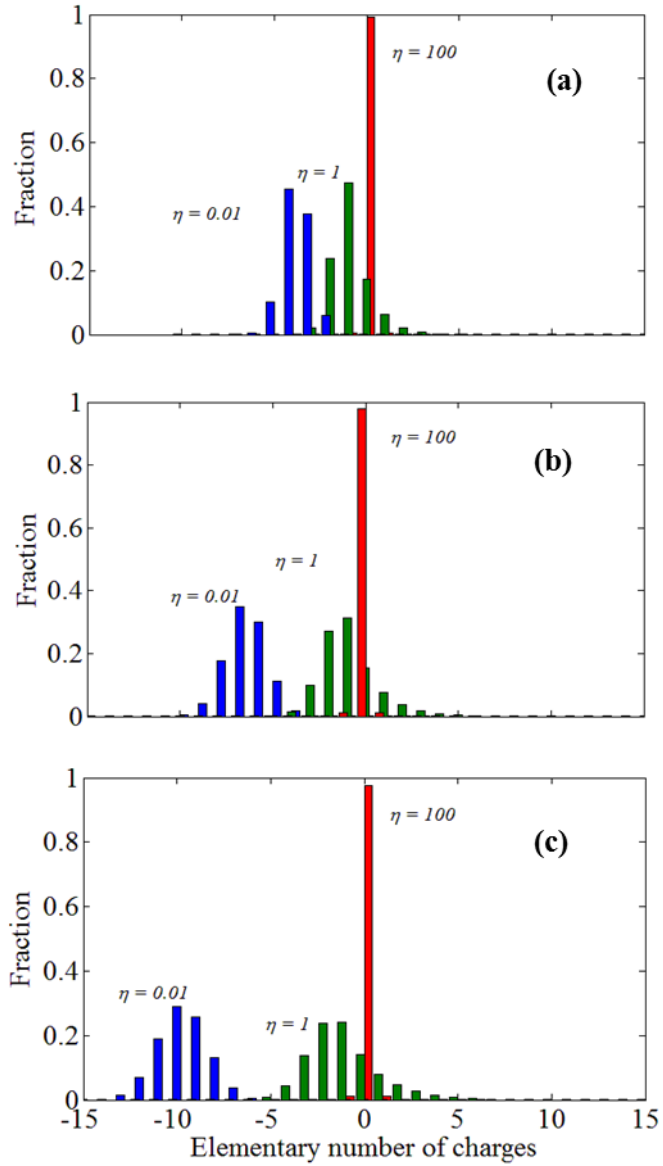


Fig. 7.3. Comparison of distribution of charged particles for zero thermal - ionization at (a) 1000 K (b) 2000 K (c) 3000 K for a fixed $N_p=10^{15} \text{ m}^{-3}$.

7.4 Ions and electrons interacting with charged particles

7.4.1 Charged particle distribution

Particles produced or introduced in a flame undergo bipolar charging due to quasi-neutrality of the flame. Depending on the temperature, the bipolar environment and the nanoparticle concentration the charge distribution would vary, as shown in Fig. 7.4. At 1000 K, for a fixed $N_{e(\text{chemi})}=10^{15} \text{ m}^{-3}$, the particles assume strong negative charges but the effect is opposite when the temperatures is increased to 3000 K. The physics behind the charging mechanism can be better understood by using average charge instead as given by Eq. (6.14). Hence, so forth instead of charge distribution, average charge at different conditions will be presented.

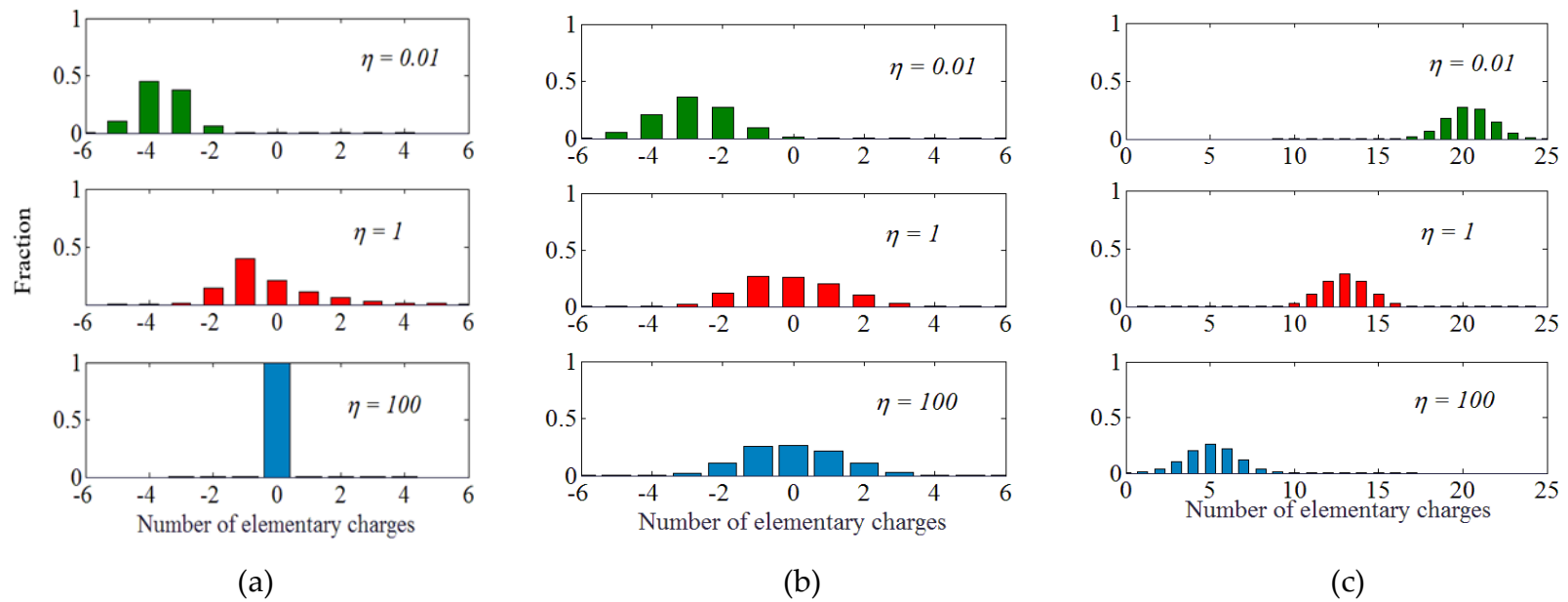


Fig. 7.4. Distribution of charged particles for different η at (a) 1000 K, (b) 2000 K and (c) 3000 K.

7.4.2 Average particle charge

7.4.2.1 Effect of work function

The work function of the material has a strong influence on the charging of the particles especially at high temperatures. The higher the work function, the more difficult it becomes for electrons to escape the material and hence the particles become less positively charged. Figure 7.5 shows the variation of fraction of charged particles for graphite, molybdenum oxide (MoO_3) and titanium oxide (TiO_2) which are amongst the common nanomaterials synthesized in flames.

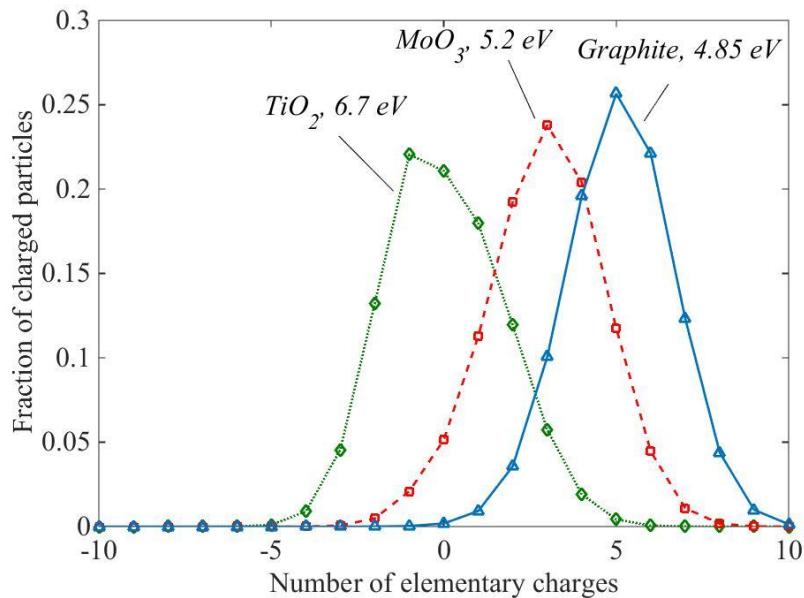


Fig. 7.5. Charge distributions for the nanoparticles of TiO_2 , MoO_3 , and graphite introduced in the flame environment with $T = 3000 \text{ K}$ and $N_{e(\text{chemi})} = 0$.

The results are calculated by turning chemi-ionization off at 3000 K which is also a temperature encountered in a flame environment when the oxygen content is very high. The particle diameter used is 20 nm and the total nanoparticle concentration is 10^{15} m^{-3} . Even a relatively small increase in work function from 4.85 eV to 5.2 eV causes the nanoparticle to become less positively charged and the peak to move from +5 to +3. Figure 7.6 represents the variation of average charge formed on the particle versus the material work function. The work function of nanomaterials for flame synthesis generally ranges from 4 eV to 7 eV. At 3000 K, as the work function increases from 4 eV to 7 eV the average charge deposited on the particle decreases from +10 to 0 respectively. As an example, for $\phi = 4 \text{ eV}$, the average nanoparticle charge varies from +1 to +23 for 2000 K to 4000 K respectively. This shows as the temperature is lowered thermal ionization becomes less influential and it will be shown later that effect of charging due to diffusion becomes important.

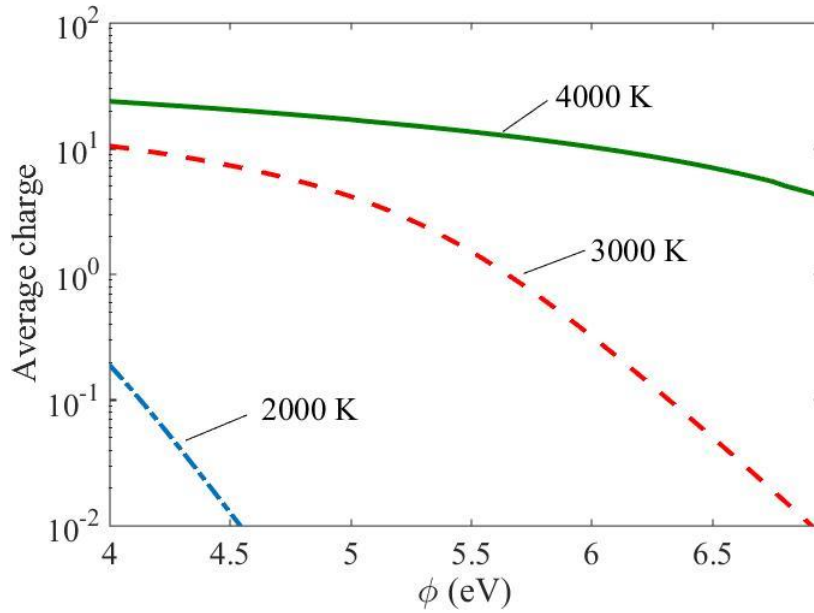


Fig. 7.6. Comparison of average charge carried by a 20 nm spherical particle at different temperatures.

7.4.2.2 Effect of temperature

Effect of temperature on nanoparticle charging has generally been ignored since most of the work done in the past has usually been in low temperature environment and also the work done for combustion studies have been limited to 2100 K (Savel'ev & Starik, 2006). But in oxy-fuel flames the temperatures could reach more than 3000 K where thermal ionization becomes very important, as shown in Fig. 7.7. When the number of nanoparticles equals that of the electrons in a given volume the electrons and ions attach to the nanoparticles creating a net zero charge until about 2100 K when the thermal-ionization gets triggered creating a net positive charge on the particle.

When $\eta = 0.01$, the diffusion charging and thermal ionization effect are more pronounced. At very low temperature diffusion charging is weak hence the net charge is close to 0, as shown in Figs. 7.4(a) and 7.7. The net charge formed on a nanoparticle at 1000 K and 2000K are close to zero but in case at 1000 K most of the particles stay neutral but at 2000 K almost equal number of particles acquire positive and negative charge and some stay neutral, as shown in Fig. 7.4(a). But as the temperature is increased the thermal velocity of electrons increases and they flow towards the nanoparticles creating a net negative charge. Ions do not have a strong effect on charging as compared to the electrons because of their much higher mass and hence much lower thermal velocities. The negative charging increases as the temperature increases until the temperatures become high enough to thermally ionize the nanoparticles and make them strongly positively charged. At $\eta = 100$ the environment around nanoparticles becomes electron deficient and hence the charging due to diffusion from chemi-ions and electrons becomes negligible. But as the temperature is increased the nano-particles themselves become highly positively charged and increase the net free electron concentration as will be discussed later.

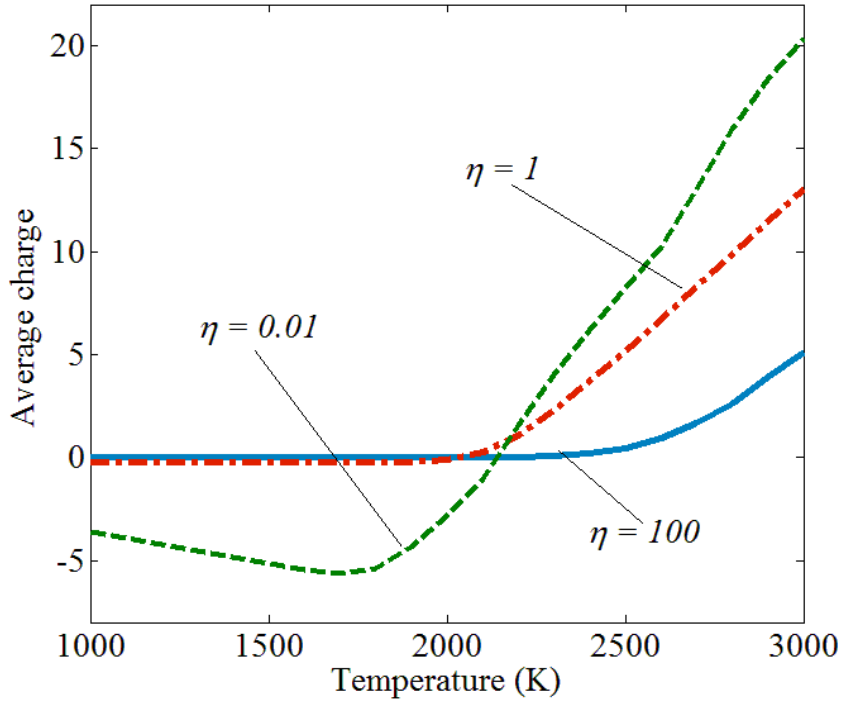


Fig. 7.7. Comparison of average charge accumulated on a 20 nm particle as a function of temperature with $N_{e(chemi)} = 10^{15} m^{-3}$ at 3 different η .

7.4.2.3 Chemi-ionization

The electrons and ions formed in a flame by chemi-ionization create a bipolar environment for nanoparticles because the total ion and electron population are generally equal. The local peak concentration of ions and electrons produced in the flame generally is of the order of $10^{16} m^{-3}$ depending on the type of the flame, the fuel and oxidizer, the temperature, pressure and the local flame chemistry (Cancian et al., 2013; Goodings et al., 1979). At temperatures up to 2000 K the average nanoparticle

charge is zero and at 3000 K the average charge is highly positive $\sim +13$, until $N_{e(\text{chemi})} = 10^{15} \text{ m}^{-3}$, as shown in Fig. 7.8. The total nanoparticle concentration is fixed at 10^{15} m^{-3} . As that ratio decreases with the increase in chemi-ions and electron concentration the electron flux towards the nanoparticle increases because the number of available electrons increase and due to that the net charge formed on the particle becomes less positive and more negative.

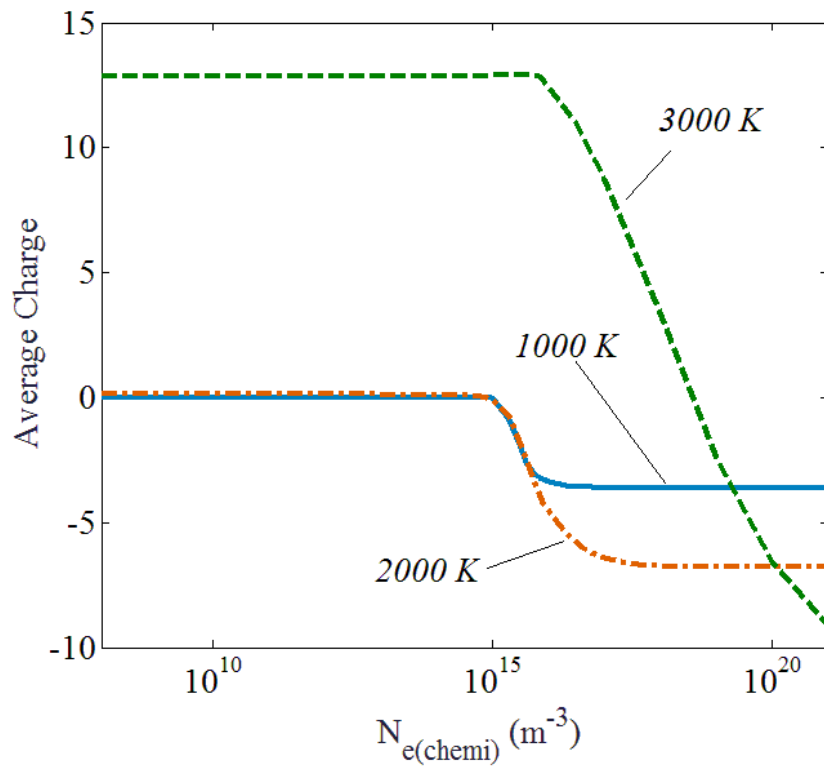


Fig. 7.8 Comparison of average charge formed on a 20 nm particle versus electrons and ions formed per unit volume by chemi-ionization at three different temperatures with $N_p = 10^{15} \text{ m}^{-3}$.

As the temperature is increased that effect is even more pronounced because of the increase in electron thermal velocity and reduced effect of thermal ionization due to decrease in nanoparticle population relative to chemi-ions and chemi-electrons. Also it is evident, for temperatures 1000 K and 2000 K the average nanoparticle charge increases between $0.01 < \eta < 1$. For 3000 K it starts to decrease when $\eta \approx 1$.

7.4.2.4 Effect of nanoparticle concentration

The amount of soot produced in the flame changes rapidly from 21 % - 100 % O₂. In the study performed on methane-oxygen oxy-fuel flames by Beltrame et al., 2001 it is evident from that increasing in oxygen content from 21 % to 100 % the soot volume fraction increases approximately from 0.03 ppmv to 0.3 ppmv respectively which corresponds to a particle density of $\sim 10^{21} \text{ m}^{-3}$ for a particle diameter of about 20 nm. In premixed flames the soot concentration also has a wide range varying from 0 to 10^{17} m^{-3} . Depending on the amount of nanoparticles per unit volume the charging time and the distribution of charges would strongly vary.

As expected, at low to mid-range temperatures, i.e. 1000 K and 2000 K, the particles become strongly negatively charged with an average charge of about -3.5 and at 3000 K the particles are highly positively charged (Fig. 7.9). The average charge increases between $0.01 < \eta < 1$ for 1000 K and 2000 K but for 3000 K the charge decreases to zero when the $N_p \sim 10^{19} \text{ m}^{-3}$. Hence from Figs. 7.8 and 7.9 we can say that the charging of a particle at a fixed diameter not only depends on the η but also on the absolute value of N_p .

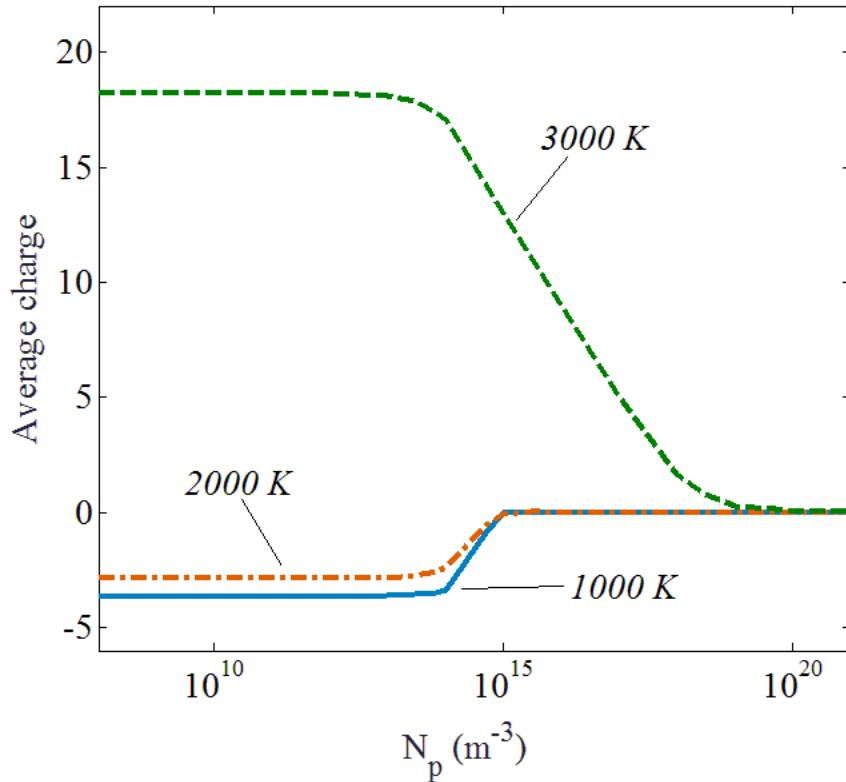
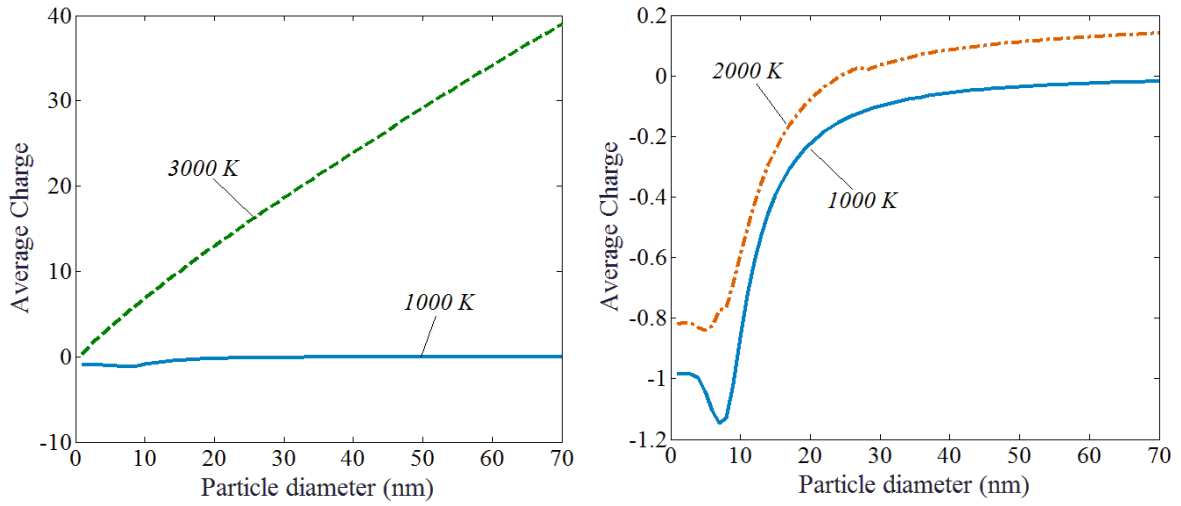


Fig. 7.9. Comparison of average charge formed on a 20 nm particle as a function of total nanoparticle concentration for a fixed $N_{e(chemi)} = 10^{15} m^{-3}$.

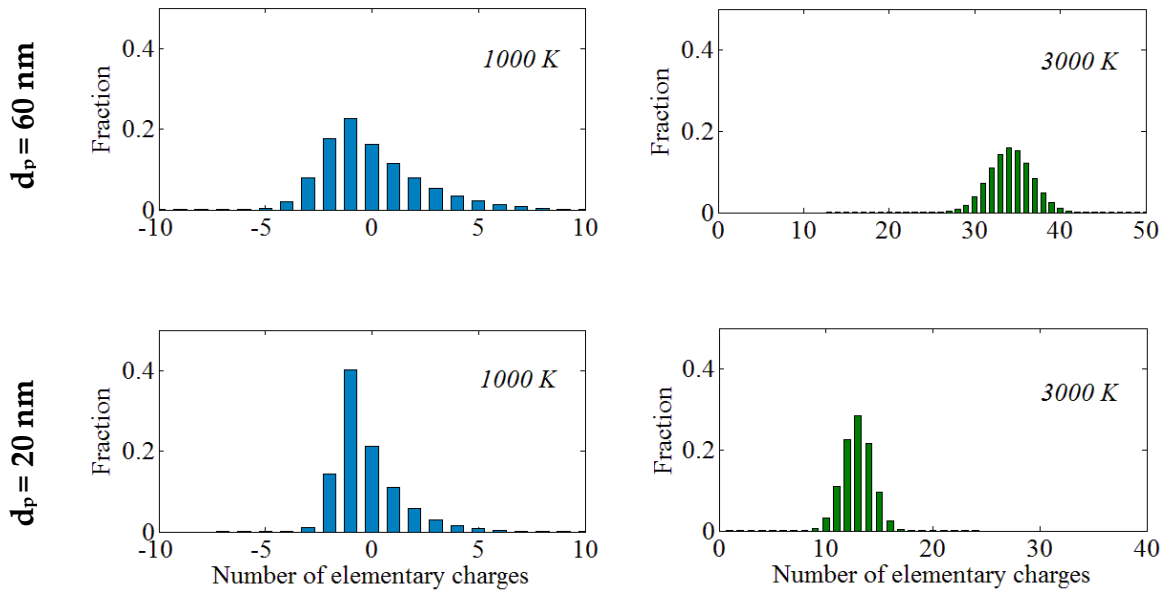
7.4.2.5 Effect of particle diameter

Primary soot particles have a spherical structure and they generally vary between 10 and 20 nm depending on the nature of the flame (Merchan-Merchan et al., 2003). But inorganic nanoparticles for flame synthesis can be as large 60 nm (Sahu et al., 2012). At 1000 K and 2000 K with fixed nanoparticle ($10^{15} m^{-3}$) and chemi-electron concentrations ($10^{15} m^{-3}$), the particles are weakly negative as shown in Fig. 7.10 and

the average charge formed is close to zero irrespective of the particle diameter. Figure 7.10 (b) indicates that at 1000 K and 2000 K, for low particle diameters, as the diameter is increased the particles become more and more negatively charged. But after a certain diameter the average charge slowly becomes close to zero with an increase in diameter. At 3000 K, with increasing size and hence the surface area, more electrons escape the potential barrier due to accelerated thermal ionization rates at those temperatures making the particles strongly positive. At this temperature, the average number of elementary charges formed on a 20 nm particle is $\sim +13$ and that on a 70 nm particle is $\sim +38$.



(a) (b)



(c)

Fig. 7.10. Comparison of (a) average charge at 1000 K and 3000 K (b) average charge at 1000 K and 2000 K (c) distribution of charges formed on a particle as a function for 20 nm and 60 nm particle and $\eta = 1$.

7.4.3 Electron concentration

7.4.3.1 Temperature

Depending on the local temperature in a flame an electron will either attach to the particle or be released due to thermal ionization. The effect of thermal ionization and diffusion charging is more pronounced when the ratio of the total nanoparticle concentration to that of chemi-electron concentration is higher, as shown in Fig. 7.11. At $\eta \gg 1$ most of the electrons available from chemi-ionization attach to the nanoparticles via diffusion charging at low temperatures reducing the net electron concentration but as the temperature is increased the particles start emitting electrons and increase the number of electrons in a given volume.

As the above ratio decreases the effect of thermal ionization and diffusion charging on net electron concentration reduces and therefore the change in net electron concentration also decreases. Due to that when $\eta \ll 1$ the net electron concentration becomes equal to the chemi-electron concentration. At 1000 K, for low chemi-electron concentration with the total nanoparticle concentration fixed at 10^{15} m^{-3} , the net electron concentration decreases because of much higher rate of attachment of electrons making the particles negatively charged, as shown in Fig. 7.12. For the same temperature at higher chemi-electron concentrations the net electron concentration becomes equal to the chemi-electron concentration. For higher temperature such as 3000 K the net electron concentration exceeds the chemi-electron concentration due to thermal ionization until $\eta \approx 1$.

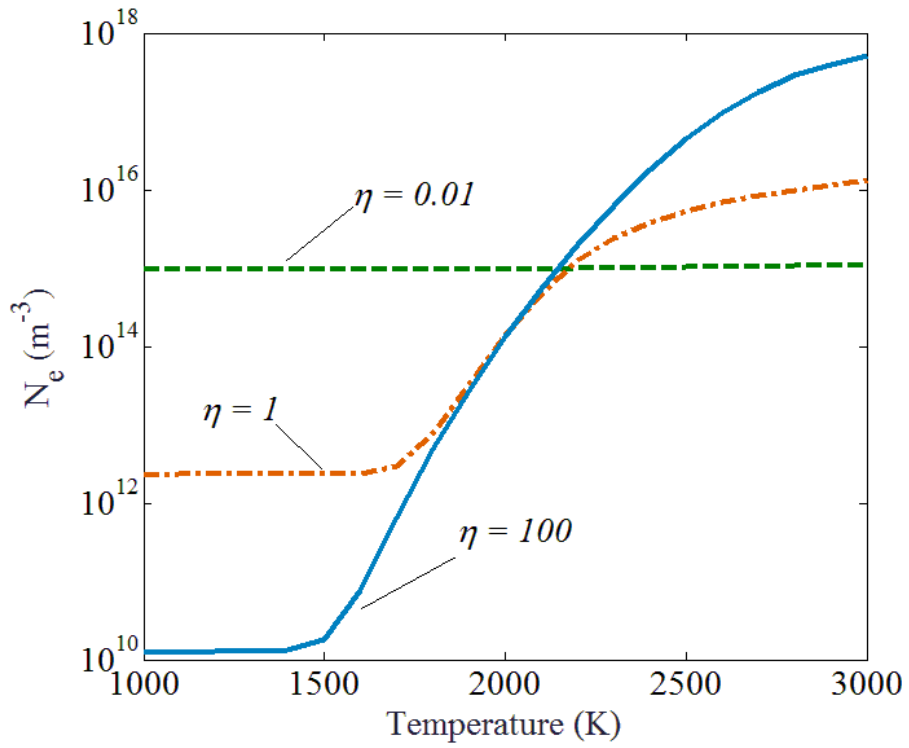


Fig. 7.11. Electron concentration as a function of temperature for $N_{e(\text{chemi})} = 10^{15} \text{ m}^{-3}$

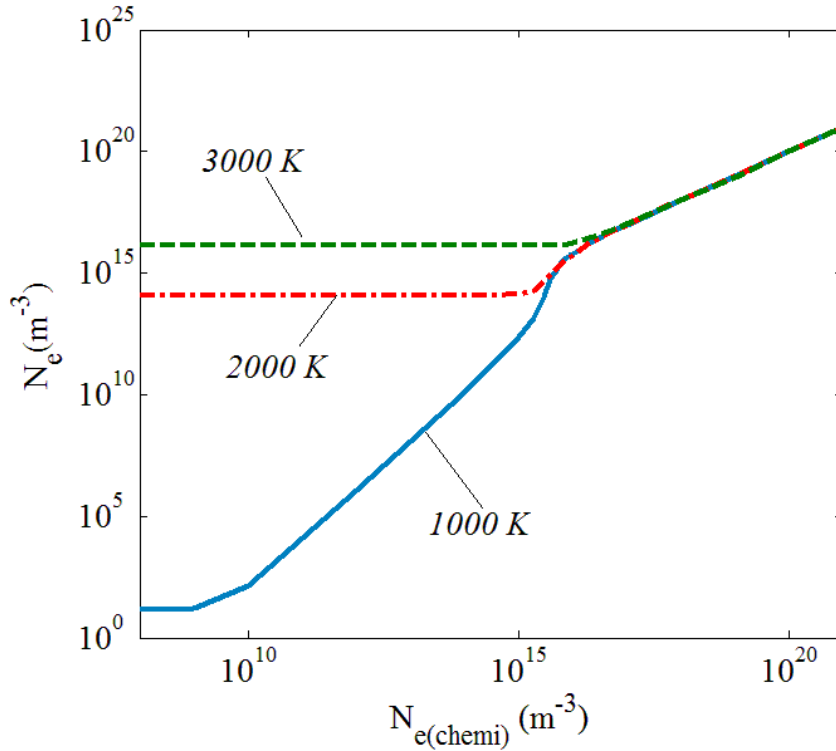


Fig. 7.12. Electron concentration as a function of electrons produced by chemi-ionization at $N_p = 10^{15} m^{-3}$.

When $\eta < 0.1$ nanoparticle concentration has a negligible influence on the net electron concentration for all temperatures because the nanoparticle density isn't high enough for thermal ionization to have a strong effect to produce free electrons and electron consumption from diffusion to reduce the electron concentration. As $\eta > 0.1$, degree of chemi-ionization has a great impact on net electron concentration depending on the temperature, as shown in Fig. 7.13. At 1000 K, relatively negligible amount of free electrons remain because most of them attach to the nanoparticles. As the

temperature is increased to 2000 K the ratio between thermal ionization rate and diffusion rate approach to 1 and hence there is a small change in free electron concentration as compared to that at 1000 K. With further rise in temperature to 3000 K the nanoparticles become thermally ionized for a large quantity of electrons to escape as the particle concentration increases. But when $\eta \approx 1000$, the system reaches an equilibrium for net electron concentration to reach a constant value of $\sim 3 \cdot 10^{18} \text{ m}^{-3}$.

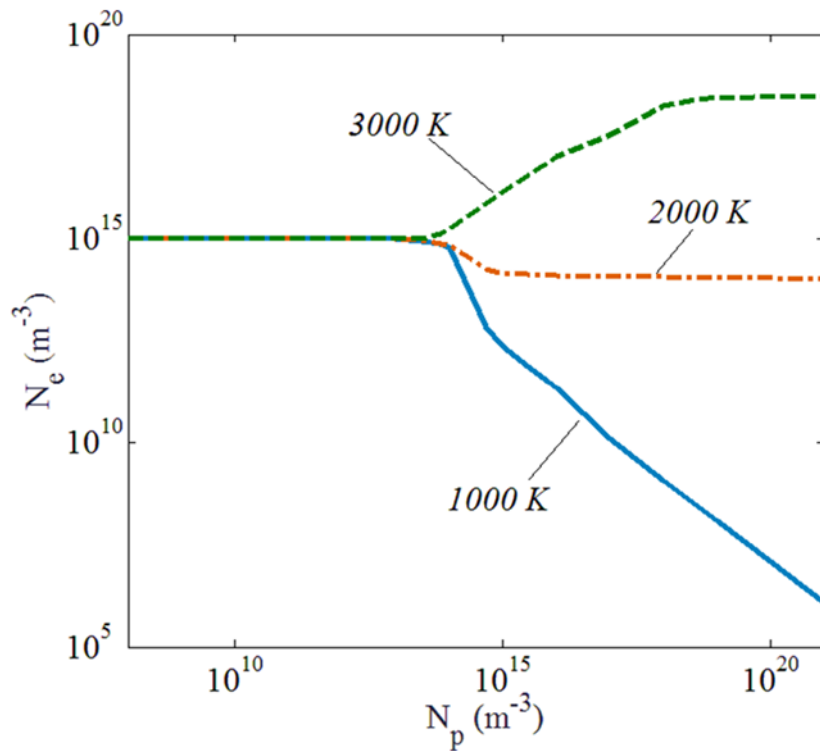


Fig. 7.13. Electron concentration as a function of total particle concentration at

$$N_{e(chemi)} = 10^{15} \text{ m}^{-3}.$$

For fixed nanoparticle and chemi-electron concentration (10^{15} m^{-3}), from Figs. 7.10 and 7.14 it can be seen that as the particle diameter increases electrons diffuse towards the particles at low temperatures making them weakly negatively charged. However as the temperature is increased to 3000 K, due to strong thermal-ionization effect particles emit large quantities of electrons $\sim 2 \cdot 10^{16} \text{ m}^{-3}$ making them strongly positive.

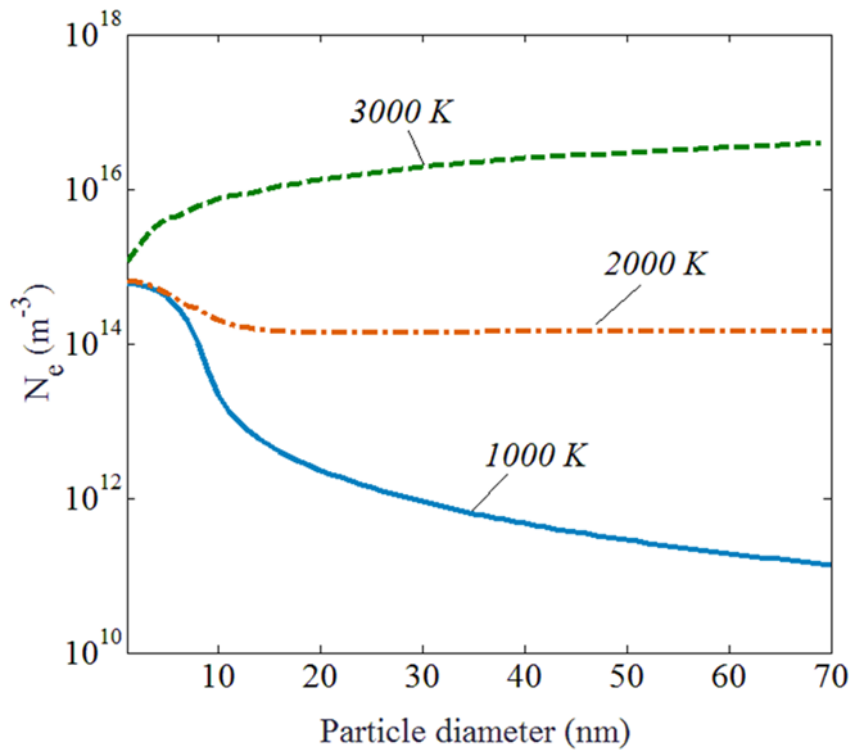


Fig. 7.14. Electron concentration as a function of particle diameter for

$$N_p = N_{e(\text{chemi})} = 10^{15} \text{ m}^{-3}.$$

7.4.4 Ion concentration

From Eq. (6.13), we can see that unlike electrons which are generated from chemi-ionization as well from the nanoparticles, ions are only formed in the flame. So diffusion charging and chemi-ionization are the processes which determine ion production and recombination with the nanoparticles. As expected, when the nanoparticle concentration is very less as compared to the chemi-electron or chemi-ion concentration there little or no change in the net ion concentration when the temperature is varied, as shown in Fig. 7.15(a). But as the nanoparticle concentration is increased relative to the fixed chemi-electron concentration, the nanoparticles act like a sink and ions attach to them decreasing the net ion concentration.

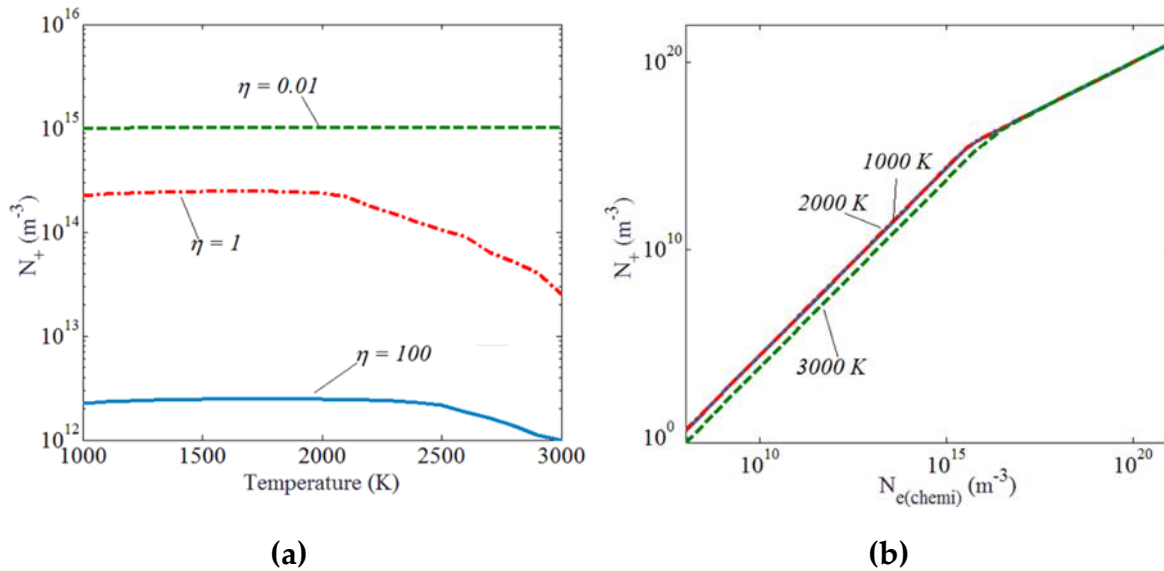


Fig. 7.15. Ion concentration as a function of (a) temperature for a fixed $N_{e(chemi)} = 10^{15} m^{-3}$ (b) electrons from chemi-ionization for a fixed $N_p = 10^{15} m^{-3}$.

As the temperature is increased from around 600 K to about 2000 K the electrons accelerate due to increase in thermal velocity and hence they create a potential barrier in order for more ions or electron to deposit on the surface. As the temperature is increased further the ion concentration reduces further because of increase in thermal ion velocity and hence depositing more on the particle surface. According to Eq. (6.9), the thermal velocity of ions has an influence at much higher temperatures as compared to electrons because of the heavier mass of electrons. This effect is also seen in Figs. 7.15(b) and 7.16(a) for low chemi-electron concentration as compared to nanoparticle concentration. At 3000 K, more ions are consumed as compared at 1000 K and 2000 K. When $\eta < 1$, the ion concentration stays unaffected and it is equal to the chemi-ion concentration due to negligible attachment of ions towards the nanoparticles. Without changing other conditions, increase in the particle diameter causes decrease in ion concentration, as shown in Fig. 7.16(b). This is because with increase in surface area, the number of ions that can attach to a particle significantly increase causing the particles positively charged.

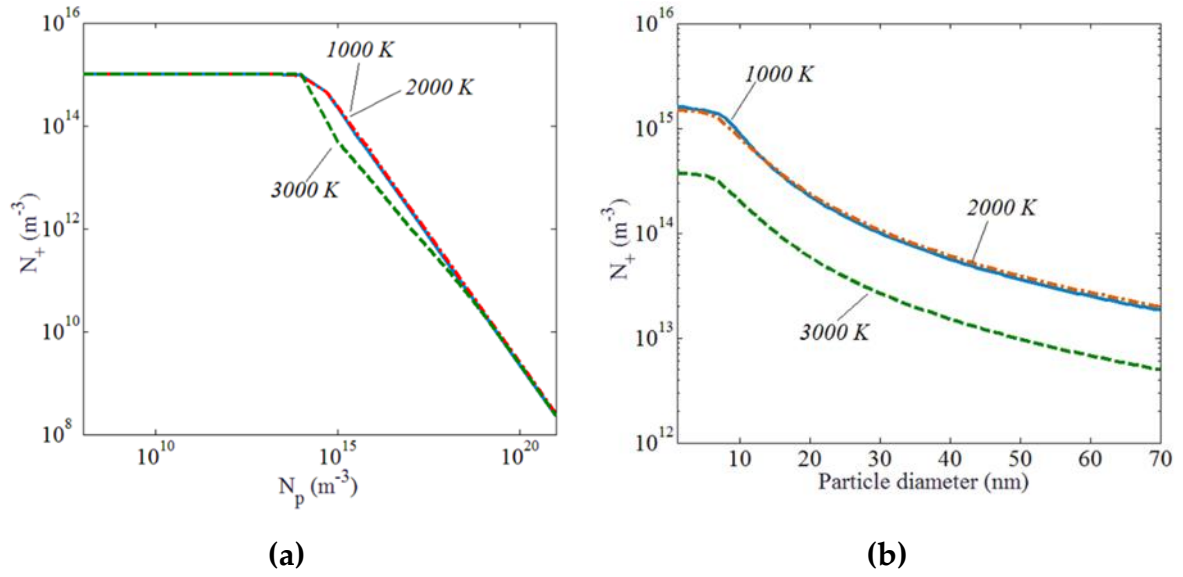


Fig. 7.16. Ion concentration as a function of (a) total particle concentration fixed

$N_{e(chemi)} = 10^{15} m^{-3}$ and (b) particle diameter for $N_p = N_{e(chemi)} = 10^{15} m^{-3}$.

8 Nanoparticle agglomerates charging model

8.1 Theory

In combustion or plasma systems, nanoparticles generally appear not only as separated primary particles but also as agglomerates which in the simplest form are primary particles attached together. In hydrocarbon flames, soot particles are first formed in the form of 5-10 nm primary particles from the reactive coagulation of PAH molecules (Megaridis and Dobbins, 1989). After that, due to coalescence, coagulation and surface growth the particles grow and become bigger. The spherical particles thus formed can attach together to form agglomerates that are open structures like linear chain or more closed structures like fractal morphology. The number of primary particles per agglomerate can range anywhere from 2 to 10,000. When an agglomerate is introduced in a bipolar ionic environment, the nature of the charge acquired by the agglomerate as a whole is quite different from that of the primary particles. Shin et al. (2010) showed that compact particles with high fractal dimension had a lower charge as compared with particles with low fractal dimension and same mobility diameter. This is because the electrical capacitance of agglomerates decreases as its structure goes from open and straight chain like structure to a more closed and branched chain like structure. Hence usually the characteristic charge of a chain like structure is usually more than charges acquired by branched chain agglomerates. In special cases, it has been shown that agglomerates with low fractal values acquire more charges than spheres when charged using a photoelectric source (Shin et al., 2010).

The objective of this study is to formulate a model and analyze the model to predict the effect of number of particles per agglomerate on charging behavior for straight chain and fractal (branched chain) particles with an aspect ratio of 1.6. The structure of the two types of agglomerates is shown in Fig. 8.1.

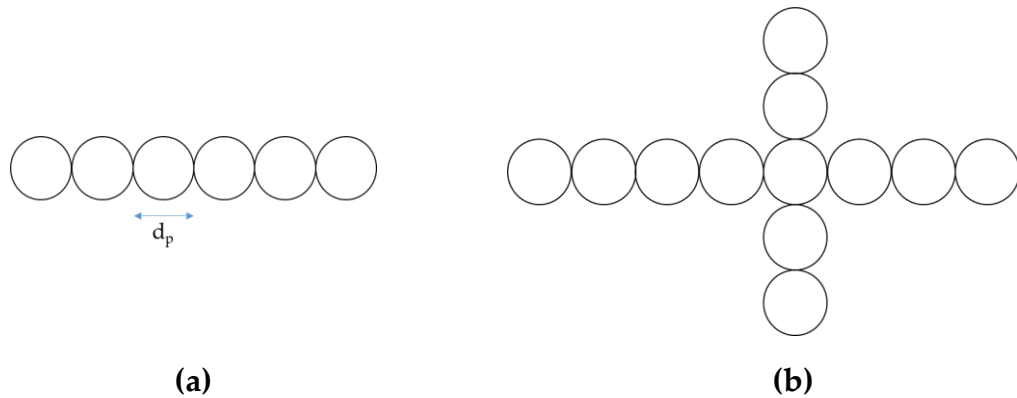


Fig. 8.1. Schematic of (a) straight chain (b) branched chain agglomerates.

8.2 Modifications to the primary nanoparticle charging model

There have been a number of theories put forward to describe the charging of agglomerates made of arbitrary and spherical shaped particles. Lafromboise and Chang (1977) created a model to evaluate the charging efficiency of arbitrary shaped particles. One of the most classical theories was put forth by Chang (1981) who

proposed a model for the mean charge for agglomerates. Chang and Yeh (1981) proposed a model for the equilibrium bipolar charge distribution on straight chain like agglomerates. Charging equivalent diameter was first put forth by Wen et al. (1984 a). Filippov (1993) showed using charge balance equations that the correct way to treat the charging of agglomerates is to use the modified Boltzmann solution instead of the standard Boltzmann law. There have been no comprehensive theories or models on agglomerate charging in a high temperature oxy-fuel environment.

The primary difference between the primary particles and the agglomerate particles is the difference in the electrical capacitance between the two. As the number of particles per agglomerate increases the capacity of the primary particles to store charge decreases because of the increase in electrostatic interaction between the two particles in the agglomerate. More open-like the structure, higher is the electrical capacitance of the agglomerate as compared to the closed-like structures. Hence we replace the conventional capacitance term by the one modified for agglomerates depending whether the agglomerate is straight chain or branched chain. We use the following capacitance 'C' terms as experimentally measured by Shin et al. (2010).

$$C = 0.5789N_A^{0.7692} (4\pi a\epsilon_0) \quad (\text{straight chain with } \beta=1.0) \quad (8.1)$$

$$C = 0.4703N_A^{0.7874} (4\pi a\epsilon_0) \quad (\text{branched chain with } \beta=1.6) \quad (8.2)$$

Also, $12 < N_A \leq 300$

Where N_A is the number of primary particles in one agglomerate and β is fractal dimension of the fractal agglomerate. The remaining parameters can be referred from Chapter 6.

Figure 8.2 shows the difference in normalized capacitance of the two type of agglomerates. It is clear that the capacitance of particles in an agglomerate is much lower than that of a particle suspended freely and the capacitance of straight chain particle is 10% - 15% higher than that of a branched chain agglomerate depending on N .

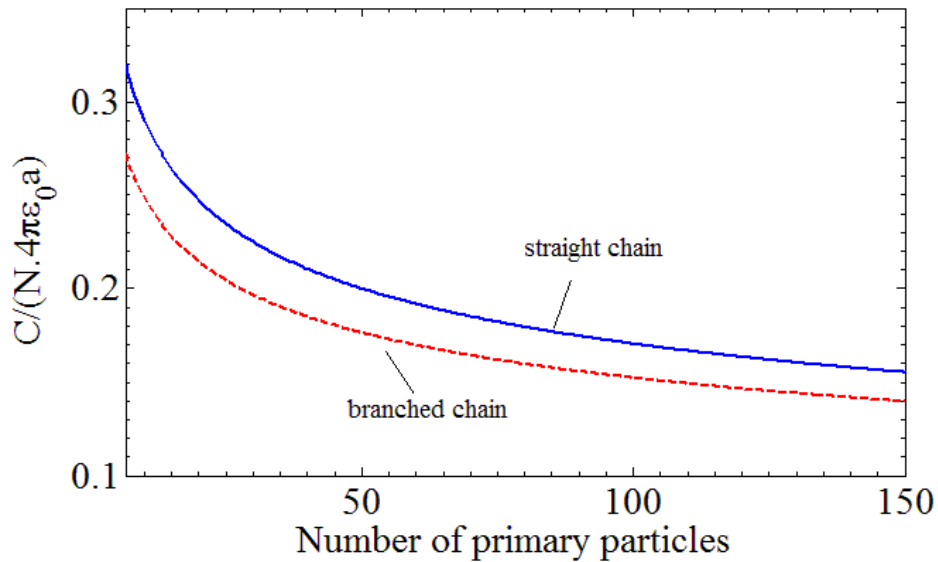


Fig. 8.2. Comparison of capacitance of straight and branched chain normalized by capacitance of primary particles.

Also if we neglect necking in the agglomerates then we can assume the surface area of the aggregate $S_{Agg} = N_A \cdot S_A$. Applying these changes to Eqs. (6.5 – 6.11) we can

formulate a modified version of the model for charging of the agglomerates as described in Section 8.3.

We shall also introduce the following new terms for the purpose of this study:

- Number of primary particles per agglomerate (N_A)
- Average charge per agglomerate (q_A)
- Number density of agglomerates (N_{pA}) which is related to the number density of primary particles by $N_{pA} = \frac{N_p}{N_A}$.

8.3 Model formulation and validation

The equation for charged nanoparticles is modified as follows:

For $z < 0$

$$\begin{aligned} \frac{dN_z}{dt} = & N_{z-1}\gamma_{z-1} + S_{Agg}N_{z+1}N_e \frac{v_e}{4} \exp\left(\frac{(z+1)e^2}{Ck_bT}\right) - N_z\gamma_z - S_{Agg}N_zN_e \frac{v_e}{4} \exp\left(\frac{ze^2}{Ck_bT}\right) \\ & + S_A N_{z-1}N_+ \frac{v_+}{4} - S_A N_zN_+ \frac{v_+}{4} \end{aligned} \quad (8.3)$$

For $z \geq 0$

$$\frac{dN_z}{dt} = N_{z-1}\gamma_{z-1} + S_{Agg}N_{z+1}N_e \frac{v_e}{4} - N_z\gamma_z - S_{Agg}N_zN_e \frac{v_e}{4} + S_A N_{z-1}N_+ \frac{v_+}{4} - S_A N_zN_+ \frac{v_+}{4} \quad (8.4)$$

The modified kinetic equation for electrons is as follows:

$$\frac{dN_e}{dt} = \dot{\omega}_e + \left(\sum_{-\infty}^{-1} \gamma_{(z<0)} N_z + \sum_0^{\infty} \gamma_{(z \geq 0)} N_z \right) - \frac{S_{Agg} \sum_{-\infty}^{-1} N_z N_e \frac{v_e}{4} \exp\left(\frac{ze^2}{Ck_b T}\right)}{\Big|_{z<0}} - \frac{S_{Agg} \sum_0^{\infty} N_z N_e \frac{v_e}{4}}{\Big|_{z \geq 0}} \quad (8.5)$$

The modified kinetic equation for ions is as follows:

$$\frac{dN_+}{dt} = \dot{\omega}_+ - S_{Agg} \sum_{-\infty}^{\infty} N_z N_+ \frac{v_+}{4} \quad (8.6)$$

$$\gamma_z(a, z) = \begin{cases} S_{Agg} AT^2 \exp\left(\frac{-\phi}{k_b T}\right) & z < 0 \\ S_{Agg} AT^2 \left(1 + \frac{(z+1)e^2}{Ck_b T}\right) \times \exp\left(-\frac{1}{k_b T} \left[\phi + \frac{(z+1)e^2}{C}\right]\right) & z \geq 0 \end{cases}$$

The parameters in the equations are described in Chapter 6. Similar to that chapter, the first term in Eqs. (8.3) and (8.4) represents the production of particle with charge z due to thermal ionization of a particle with charge $(z - 1)$. The second term describes the generation of a particle with charge z due to the diffusion of electrons to a particle with charge $(z + 1)$. The third term denotes the loss of a nanoparticle with charge z due to thermal ionization of a particle with charge z . The fourth term indicates again the loss of the particle with charge z due to diffusion of electrons to the same. The fifth and the six terms are responsible for the increase and decrease of the charged nanoparticle due to the diffusion of positive ions to a nanoparticle with charges $(z - 1)$ and z respectively.

The first term in Eqs. (8.5, 8.6) describe the net generation or consumption of electrons and ions due to chemi-ionization alone. The second term in Eq. (8.5) denotes the emission of electrons from thermal-ionization. The third term and the second term of

Eqs. (8.5) and (8.6), respectively, represent the loss of electrons and ions due to diffusion and recombination of charged species to the nanoparticles with charge z . Eqs. (6.1 – 6.4), (6.14) and (6.15) apply here as well.

The model thus formulated is validated by comparing the results for average charge per particle with previous experimental results (Ball and Howard, 1971), as shown in Fig. 8.3. The conditions used here were $N_{e(chemi)}=10^{14} \text{ m}^{-3}$, $N_p=10^{10} \text{ m}^{-3}$, $T=2100 \text{ K}$ and $\phi = 4.35 \text{ eV}$ for soot. The average charge thus calculated shows a similar trend and matches to a great degree for larger particles.

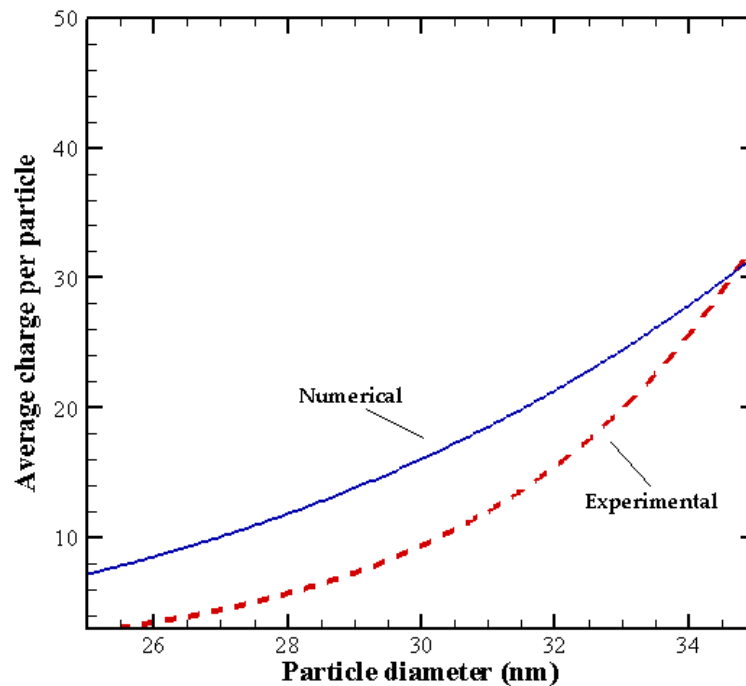


Fig. 8.3. Comparison of previous experimental (Ball and Howard, 1971) and numerical results.

8.4 Results of the nanoparticle agglomerates charging model

8.4.1 Zero chemi-ionization

The model is simplified to analyze the effect of thermal ionization only. Hence, the chemi-ionization term is neglected. As discussed at Section 7.2, the thermal ionization is dominant at 3000 K. Hence, the conditions used here are as follows: $N_p = 10^{15} \text{ m}^{-3}$, $T = 3000 \text{ K}$, $d_p = 20 \text{ nm}$.

Figure 8.4 shows that the net charge acquired by the agglomerates is higher for the straight chain structures than the branched chain structures. The difference in charges acquired become higher as the number of primary particles increases. But the average charge acquired by per particle decreases with an increase in N_A . This is because when N_A increases the electrostatic interaction between the particles increase making them less and less positively charged. The reason they get positively charged is because at 3000 K, the electrons on the material surface acquire enough energy to escape and hence the thermal ionization rate is very high. This makes the particles to become strongly positively charged.

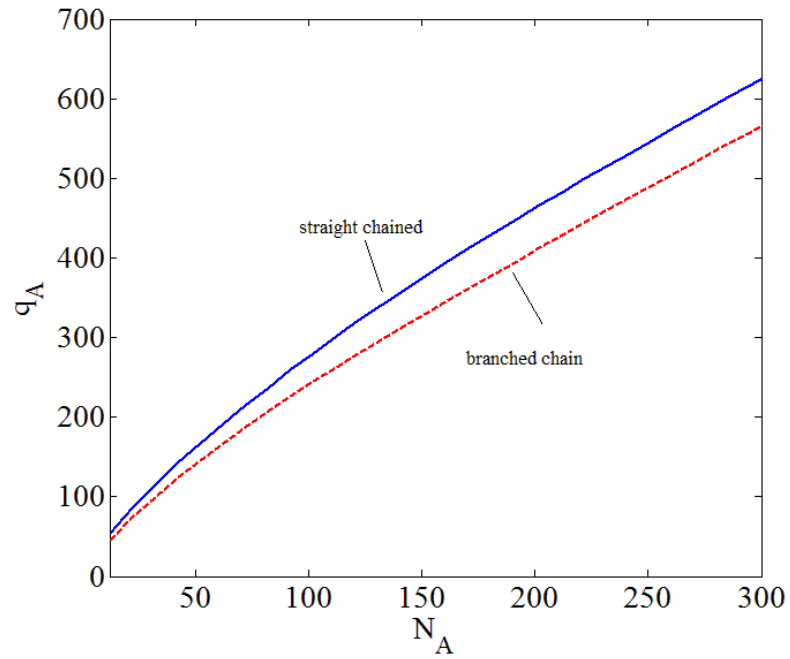


Fig. 8.4. Comparison of net charge formed on an agglomerate as a function of the number of primary particles for zero chemi-ionization.

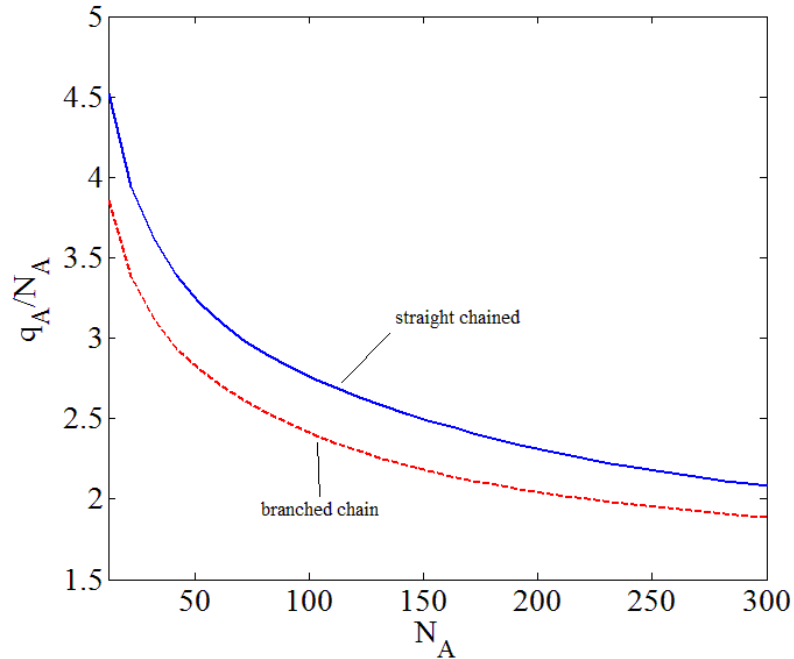


Fig. 8.5. Comparison of net charge per particle of an agglomerate as a function of the number of primary particles for zero chemi-ionization.

8.4.2 Zero thermal-ionization

The model is simplified to analyze the effect of chemi-ionization only. Hence, the thermal-ionization term is neglected. From section 7.3 we see that chemi-ionization is most dominant when $T=1000\text{K}$. Hence, the conditions used here are as follows: $N_p=10^{15}\text{m}^{-3}$, $T=1000\text{K}$, $d_p=20\text{nm}$, $N_{e(\text{chemi})}=10^{15}\text{m}^{-3}$

The agglomerates become negatively charged as the number of primary particles increases. The reason is at 1000K , the conditions are suitable for electrons generated from chemi-ionization to attach to the nanoparticles. The positive ions which are

although available in equal number do not attach equally to the particles as their thermal velocity is much lower than that of the electrons. As a result the agglomerates are strongly negatively charged.

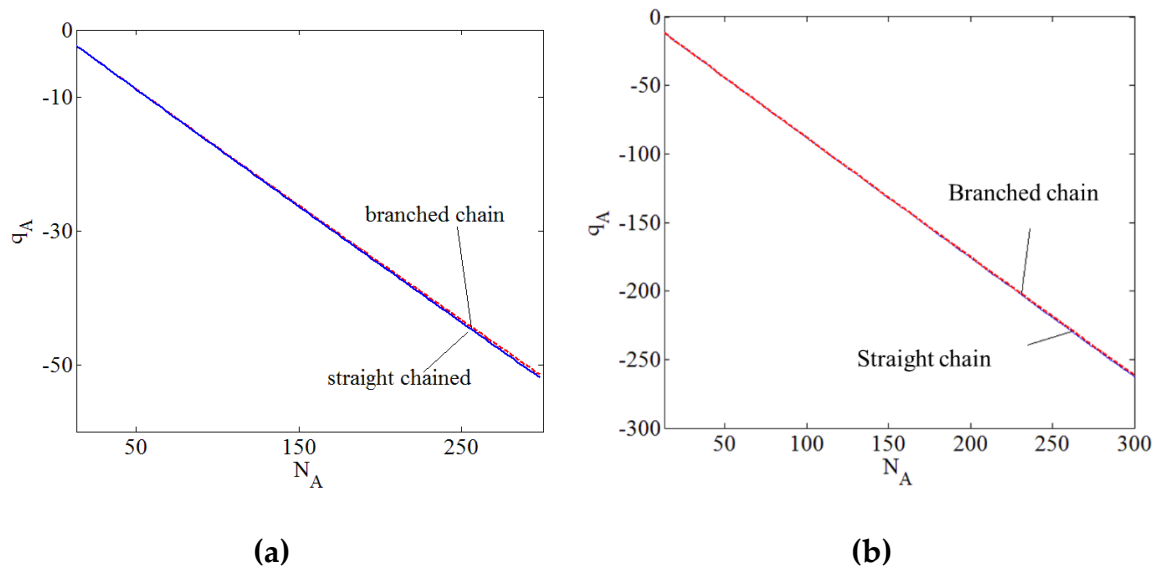


Fig. 8.6. Comparison of net charge formed on an agglomerate as a function of the number of primary particles for zero thermal-ionization at (a) 1000 K (b) 3000K.

In the case of chemi-ionization the average charge on particle is not highly negative unlike thermal ionization where the agglomerates and the particles become highly positive, as shown in Fig. 8.7. The reason being the strong electrostatic repulsion felt by the particles as the number of particles increases, making the particles weakly

negatively charged. As the temperature is increased to 3000 K the agglomerates become more negatively charged, as shown in Figs. 8.6(b) and 8.7(b).

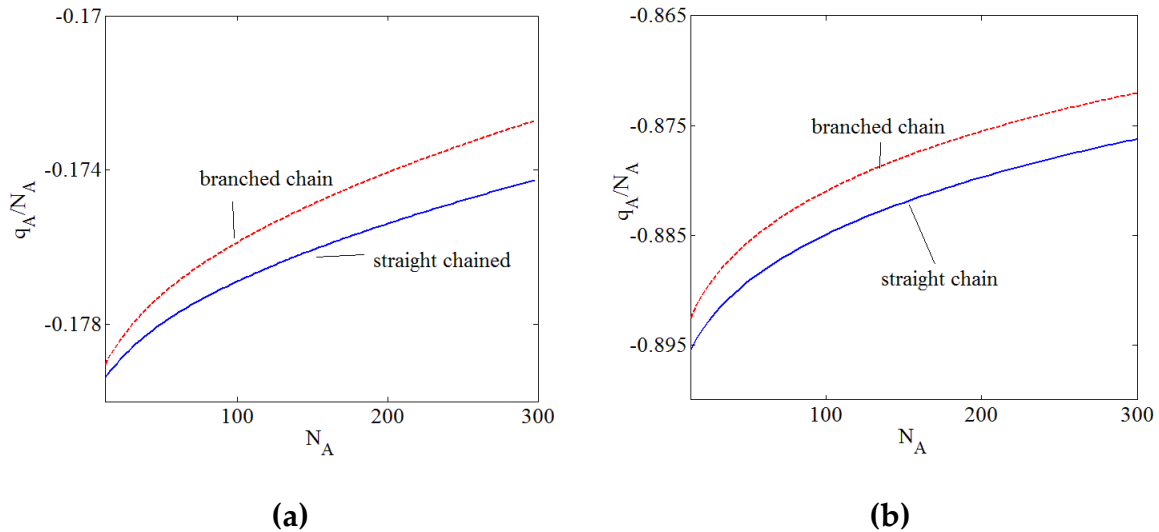


Fig. 8.7. Comparison of net charge formed on an agglomerate as a function of the number of primary particles for zero thermo-ionization (a) 1000 K (b) 3000K.

8.4.3 Relative charge and effects on ions and electrons

It might be beneficial and more intuitive to express the charging behavior in terms of charge deposited on a primary particle in an agglomerate relative to that on a single particle under same conditions i.e. $\frac{q_A}{N_A q_{(1)}}$.

where, $q_{(1)}$ is the charge deposited on a single particle.

Let see the effect of thermal-ionization only under conditions same as in Section 8.4.1. Figure 8.8 shows that the relative charge on an agglomerate decreases strongly with an increase in number of primary particles. It is as low as 15% when the number of primary particles is 300.

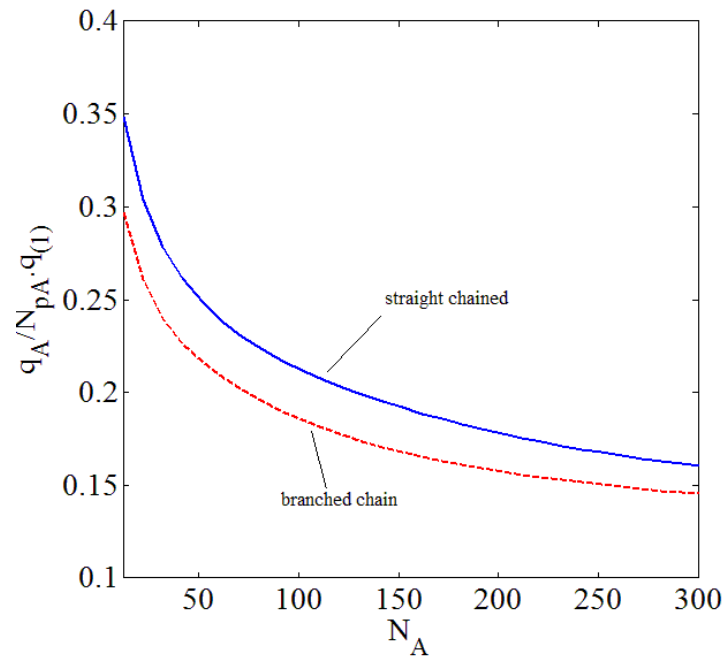


Fig. 8.8. Comparison of relative charge for straight chain and branched chain agglomerates with zero chemi-ionization.

We also calculate the relative charge when there is no thermal-ionization but only chemi-ionization as in Fig. 8.9 for conditions same as in Section 8.4.2. We see the relative charge does not decrease as much as it decreases when there is only thermal-ionization. Also, there is not a big difference in the charging of straight chain and the branched chain agglomerates. The electron concentration at 3000 K when there are no agglomerates but only equal number of singular particles is 3.10^{18} m^{-3} . When agglomerates are introduced the particles become highly positively charged but not as much as the singular particles. Hence less number of electrons are released, as shown in Fig. 8.9.

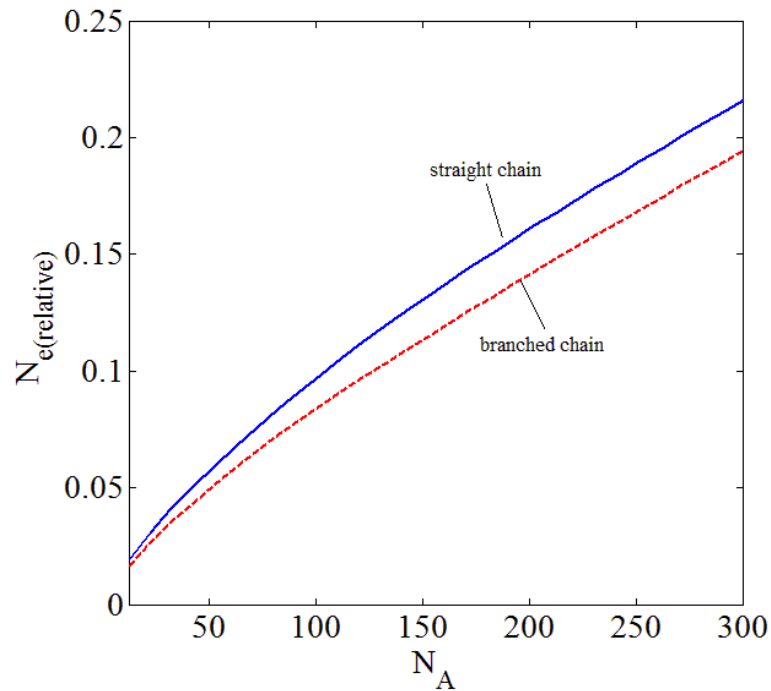


Fig. 8.9. Relative electron concentration as a function of number of primary particles.

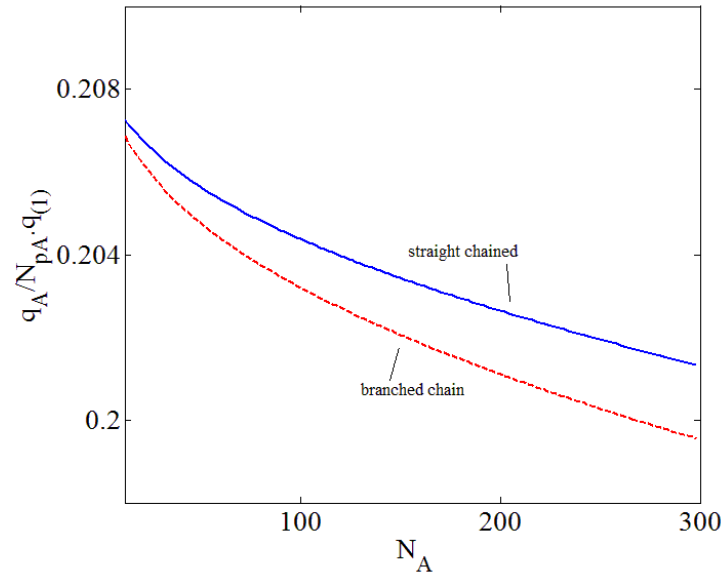


Fig. 8.10. Comparison of relative charge for straight chain and branched chain agglomerates with zero thermal-ionization.

8.4.4 Ions and electrons in equilibrium with charged agglomerates

8.4.4.1 Effect of primary particle diameter

Size of the primary particle in an agglomerate also has a strong influence on the charging of the particles since the surface area increases with the size. We study the effect of diameter on charging under following conditions: $N_{e(chemi)} = 10^{13} \text{ m}^{-3}$, $N_p = 10^{15} \text{ m}^{-3}$, $T = 3000 \text{ K}$.

Figure 8.11 shows that as the diameter increases the charge deposited increases linearly as anticipated. Also, the charge acquired by particles in an agglomerate is small as compared to that by single particles due to the reduced relative capacitance. As the number of primary particles in an agglomerate increases the charge acquired by primary particle decreases.

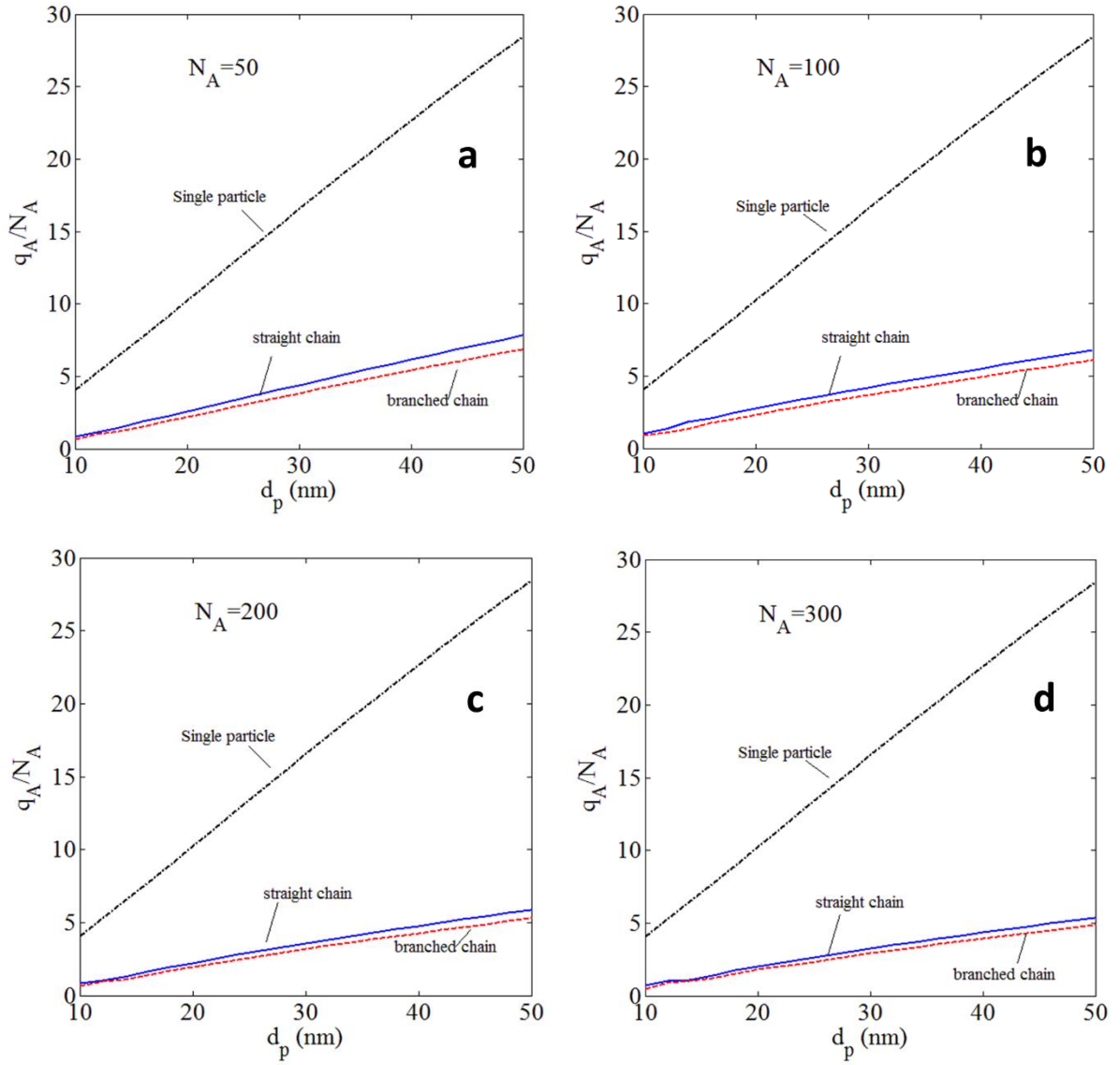


Fig. 8.11. Comparison of charge on a primary particle as a function of particle diameter for (a) $N_A= 50$ (b) $N_A= 100$ (c) $N_A= 200$ (d) $N_A= 300$.

9 Conclusions

The thesis had two major objectives. The first one was to experimentally measure and numerically model the charged species concentration in a methane-oxygen counterflow diffusion flame. This part of the effort was primarily to gain a better understanding of the charged species distribution in a diffusion flame at different oxygen contents and at different strain rates. This would help in better understanding of the chemi-ionization processes and the ionic chemistry in diffusion flames and to predict the charge species concentrations as a function of oxygen contents by using a simple experimental and a numerical technique.

A model that used a detailed methane-oxygen neutral and ionic chemistry was analyzed and compared with the experimental results. A traditional Langmuir probe was modified specifically for high temperature and atmospheric conditions to generate reasonable volt-ampere characteristics for different conditions to validate the numerical results. The results proved to be in an appreciable agreement with the experiments. The numerical results were successfully able to predict the effect of oxygen and strain rate on electron and ion concentrations. The results showed that increase in oxygen content has a big impact on peak electron and positive ion concentration. The peak electron concentration increases as much as by three times and the peak positive ion concentration increases as much as by four times. The experiments also validated the fact that strain rate has a small effect on the charged species concentrations. When the effect of thermal-ionization from major neutral molecules in the flame at 3000 K was analyzed it was concluded that the number of electrons emitted from those molecules was negligible as compared to those emitted

due to chemi-ionization and hence this effect was not included in the experiments and the numerical model. It was shown with good agreement between experimental and numerical results that electrons are the primary negative charge carriers and the hydronium (H_3O^+) ions are the major positive charge carriers in the flame. Hence, the total ion concentration was assumed to be equal to the hydronium ion concentration.

The second part of the thesis proposed and analyzed a numerical model to predict the charging behavior of spherical and fractal agglomerates and the interaction of the same with ions and electrons in oxy-fuel flame environment. A set of population balance equations for nanoparticle charging, ion formation and electron formation are solved temporally and the steady state solution is used to perform parametric studies on the charging behavior of the nanoparticles. The model's significant success was proved when it was validated not only with previous numerical models but also with previous experimental results and found to be in good agreement with both. The model is one of a kind because it includes the three effects i.e. chemi-ionization, diffusion charging and thermal-ionization in a simplified format. It shows that the nanoparticle charging is extremely sensitive to material, temperature, nanoparticle size, degree of chemi-ionization and also the total nanoparticle concentration. It proved that the particles become highly positively charged at high temperatures in an oxy-fuel flame environment because of high rate of thermal-ionization. At low temperatures and the regions where chemi-ionization is dominant the particles become strongly negatively charged due to the higher mobility of electrons and hence the high rate of attachment. Also, the total nanoparticle concentration has a big influence on electrons. Electron concentration increases as much as 10^5 times at 3000 K with increase in nanoparticle concentration from 10^8 to 10^{19} m^{-3} while at 1000 K

electrons almost get consumed with nanoparticle addition. Ion concentration decreases strongly with nanoparticle concentration irrespective of the temperature unlike the electrons. Another big accomplishment made by the model was to achieve reasonable results when simple and empirical modifications were made to the capacitance term in the case for the agglomerate particles. Increase in the chemi-ionization effect makes the particles more charged whereas increase in the nanoparticle concentration makes particles less charged. The model showed that the linear chain agglomerates are charged more than the branched chain agglomerates due to their relatively more open structure and hence less interaction with the other nanoparticles in the agglomerates for the same number of particles per agglomerate. With more number of primary particles per agglomerate the average negative or positive charged formed on the particle decreases. This is because the capacitance per primary particle would decrease with number of primary particles in an agglomerate. Future studies can be performed by solving the flame model together with the nanoparticle model and develop a comprehensive 1-D model to evaluate the charging behavior of soot particles and their interaction with the individual charged species in the flame.

REFERENCES

- Axford, S. D. T., Goodings, J. M., & Hayhurst, A. N. (1998). Mass-spectrometric sampling of ions from flames at atmospheric pressure: The effects of applied electric fields and the variation of electric potential in a flame. *Combustion and flame*, 114(3), 294-302.
- Ball, R. T., & Howard, J. B. (1971, December). Electric charge of carbon particles in flames. In *Symposium (International) on Combustion* (Vol. 13, No. 1, pp. 353-362). Elsevier.
- Balthasar, M., Mauss, F., & Wang, H. (2002). A computational study of the thermal ionization of soot particles and its effect on their growth in laminar premixed flames. *Combustion and Flame*, 129, 204-216.
- Bascombe, K. N., Green, J. A., & Sugden, T. M. (1963). *Advances in mass spectrometry*, vol. 2.
- Beltrame, A., Porshnev, P., Merchan-Merchan, W., Saveliev, A., Fridman, A., Kennedy, L. A., & Charon, O. (2001). Soot and NO formation in methane–oxygen enriched diffusion flames. *Combustion and Flame*, 124, 295-310.
- Belhi, M., Domingo, P., & Vervisch, P. (2010). Direct numerical simulation of the effect of an electric field on flame stability. *Combustion and flame*, 157(12), 2286-2297.
- Brande, W. T. (1814). The Bakerian Lecture: On some new electro-chemical phenomena. *Philosophical Transactions of the Royal Society of London*, 51-61.
- Bulewicz, E. M., & Padley, P. J. (1963). Ninth Symposium (International) on Combustion. *Academic Press, New York*, 324, 638.
- Burcat, A., & Ruscic, B. (2005). *Third millenium ideal gas and condensed phase thermochemical database for combustion with updates from active thermochemical tables*. Argonne, IL: Argonne National Laboratory.

- Burke, R., Dewael, F., & Van Tiggelen, A. (1963). Kinetics of the propylene—Oxygen flame reaction. *Combustion and flame*, 7, 83-87.
- Calcote, H. F. (1957). Mechanisms for the formation of ions in flames. *Combustion and Flame*, 1(4), 385-403.
- Calcote, H. F. (1961). Ion production and recombination in flames. In *Symposium (International) on Combustion*, 8(1), 184-199.
- Calcote, H. F. (1963). Ion and electron profiles in flames. *Symposium (International) on Combustion* 9: 1, 622-637.
- Calcote, H. F. (1981). Mechanisms of soot nucleation in flames—a critical review. *Combustion and Flame*, 42, 215-242.
- Cancian, J., Bennett, B. A. V., Colket, M. B., & Smooke, M. D. (2013). Prediction of electron and ion concentrations in low-pressure premixed acetylene and ethylene flames. *Combustion Theory and Modelling*, 17, 294-315.
- Chang, J. S. (1981). Theory of diffusion charging of arbitrarily shaped conductive aerosol particles by unipolar ions. *Journal of Aerosol Science*, 12(1), 19-26.
- Chase, W., C.A. Davies, J.R. Downey, Jr., D.J. Frurip, R.A. McDonald, and A.N. Syverud. *J. Phys. Chem. Ref. Data*, 14.
- Cheng, Y. S., & Yeh, H. C. (1981). Equilibrium bipolar charge distribution of aerosols consisting of chains of uniform spheres. *Journal of Colloid and Interface Science*, 84(2), 444-450.
- Clements, R. M. (1978). Plasma diagnostics with electric probes. *Journal of Vacuum Science and Technology*, 15(2), 193-198.
- Desai, M. (2011). *Gas-phase and Solid Support Flame Synthesis of Transition Metal Oxide Structures in a Counter-flow Diffusion Flame* (Doctoral dissertation, University of Oklahoma).
- Eraslan, A. N., & Brown, R. C. (1988). Chemiionization and ion-molecule reactions in fuel-rich acetylene flames. *Combustion and flame*, 74(1), 19-37.

- Fialkov, A. B. (1997). Investigations on ions in flames. *Progress in Energy and Combustion Science*, 23, 399-528.
- Filippov, A. V. (1994). Charge distribution among non-spherical particles in a bipolar ion environment. *Journal of aerosol science*, 25(4), 611-615.
- Fuchs, N. A. (1963). On the stationary charge distribution on aerosol particles in a bipolar ionic atmosphere. *Geofisica Pura e Applicata*, 56, 185-193.
- Feugier, A., & Van Tiggelen, A. (1965). Tenth Symposium (International) on Combustion. *The Combustion Institute, Pittsburgh*, 621.
- Franklin, R. N. (2003). Ambipolar diffusion is a misnomer. *Journal of Physics D: Applied Physics*, 36(7), 828.
- Gerhardt, P., Homann, K. H., Lffler, S., & Wolf, H. (1988). Large ionic species in sooting acetylene and benzene flames. *Combustion and Fuels in Gas Turbine Engines*, 22, 2.
- Glassman, I. (1989, December). Soot formation in combustion processes. In *Symposium (international) on combustion* (Vol. 22, No. 1, pp. 295-311). Elsevier.
- Goodings, J. M., Bohme, D. K., & Sugden, T. M. (1977, December). Positive ion probe of methane-oxygen combustion. In *Symposium (International) on Combustion* (Vol. 16, No. 1, pp. 891-902). Elsevier.
- Goodings, J. M., Bohme, D. K., & Ng, C. W. (1979). Detailed ion chemistry in methane-oxygen flames. I. Positive ions. *Combustion and Flame*, 36, 27-43.
- Goodings, J. M., Bohme, D. K., & Ng, C. W. (1979). Detailed ion chemistry in methane-oxygen flames. II. Negative ions. *Combustion and Flame*, 36, 45-62.
- Goodwin, D. (2009). Cantera: An object-oriented software toolkit for chemical kinetics, thermodynamics, and transport processes", *Caltech, Pasadena*. [Online]. Available:<http://code.google.com/p/cantera>.
- Grcar, J. F. (1992). The Twopnt program for boundary value problems. *Sandia National Laboratories Report SAND91-8230*.

- Guénault, E. M., & Wheeler, R. V. (1931). XXVII. — The propagation of flame in electric fields. Part I. Distortion of the flame surface. *Journal of the Chemical Society (Resumed)*, 195-199.
- Gunn, R. (1955). The statistical electrification of aerosols by ionic diffusion. *Journal of Colloid Science*, 10(1), 107-119.
- Homann, K. H., & Wolf, H. (1983). Charged Particles in Sooting Flames II. Determination of the Fraction of Charged Soot. *Berichte der Bunsengesellschaft für Physikalische Chemie*, 87, 1073-1077.
- Hoppel, W. A., & Frick, G. M. (1986). Ion—Aerosol Attachment Coefficients and the Steady-State Charge Distribution on Aerosols in a Bipolar Ion Environment. *Aerosol Science and Technology*, 5(1), 1-21.
- Jain, S. C., & Krishnan, K. S. (1952). The thermionic constants of metals and semi-conductors. I. Graphite. *Proceedings of the Royal Society of London. Series A. Mathematical and Physical Sciences*, 213(1113), 143-157.
- Jiang, J., Lee, M. H., & Biswas, P. (2007). Model for nanoparticle charging by diffusion, direct photoionization, and thermionization mechanisms. *Journal of Electrostatics*, 65, 209-220.
- Karman, T. (1946). Ztsch. angew. Mathematik Mechanik (1921) 1. *NACA Technical Memorandum*, (1092), 233.
- Kee, R. J., Miller, J. A., Evans, G. H., & Dixon-Lewis, G. (1988). Twenty-Second Symposium (International) on Combustion. *The Combustion Institute, Pittsburgh*, 1479-1494.
- Kelly, R., & Padley, P. J. (1969). Use of a rotating single probe in studies of ionization of metal additives to premixed flames. Part 1.—Measurement of total positive ion concentrations, and ionization of gallium, indium and thallium. *Transactions of the Faraday Society*, 65, 355-366.
- Knewstubb, P. F., & Sugden, T. M. (1960). Mass-spectrometric studies of ionization in flames. I. The spectrometer and its application to ionization in hydrogen

flames. *Proceedings of the Royal Society of London. Series A. Mathematical and Physical Sciences*, 255(1283), 520-537.

Kuo, K. K. (1986). *Principles of combustion*.

Lawton, J., & Weinberg, F. J. (1969). *Electrical aspects of combustion* (Vol. 1). Oxford: Clarendon Press.

Laframboise, J. G., & Chang, J. S. (1977). Theory of charge deposition on charged aerosol particles of arbitrary shape. *Journal of Aerosol Science*, 8(5), 331-338.

Lall, A. A., & Friedlander, S. K. (2006). On-line measurement of ultrafine aggregate surface area and volume distributions by electrical mobility analysis: I. Theoretical analysis. *Journal of Aerosol Science*, 37(3), 260-271.

Lochte-Holtegreven, W. (1968). *Plasma-diagnostics*. Amsterdam: North-Holland Publication Co., 1968, edited by Lochte-Holtegreven, W., 1.

Lutz, A. E., Kee, R. J., Grcar, J. F., & Rupley, F. M. (1997). OPPDIF: A Fortran program for computing opposed-flow diffusion flames. *Sandia National Laboratories Report SAND96-8243*.

Maricq, M. M. (2005). The dynamics of electrically charged soot particles in a premixed ethylene flame. *Combustion and Flame*, 141, 406-416.

Maricq, M. M. (2006). A comparison of soot size and charge distributions from ethane, ethylene, acetylene, and benzene/ethylene premixed flames. *Combustion and Flame*, 144, 730-743.

Mayo, P. J., and Weinberg, F. J. (1970). On the size, charge and number-rate of formation of carbon particles in flames subjected to electric fields. *Proceedings of the Royal Society of London. A. Mathematical and Physical Sciences*, 319, 351-371.

McBride, B. J., Zehe, M. J., & Gordon, S. (2002). *NASA Glenn coefficients for calculating thermodynamic properties of individual species*. National Aeronautics and Space Administration, John H. Glenn Research Center at Lewis Field.

- Megaridis, C. M., & Dobbins, R. A. (1989, December). Soot aerosol dynamics in a laminar ethylene diffusion flame. In *Symposium (International) on Combustion* (Vol. 22, No. 1, pp. 353-362). Elsevier.
- Merchan-Merchan, W., Saveliev, A. V., & Kennedy, L. A. (2003). Carbon nanostructures in opposed-flow methane oxy-flames. *Combustion Science and Technology*, 175(12), 2217-2236.
- Merchan-Merchan, W., Saveliev, A. V., & Kennedy, L. A. (2003). Carbon nanostructures in opposed-flow methane oxy-flames. *Combustion Science and Technology*, 175, 2217-2236.
- Mizuno, A. (2000). Electrostatic precipitation. *IEEE Transactions on Dielectrics and Electrical Insulation*, 7, 615-624.
- Mott-Smith, H. M., & Langmuir, I. (1926). The theory of collectors in gaseous discharges. *Physical review*, 28(4), 727.
- Ombrello, T., Qin, X., Ju, Y., Gutsol, A., Fridman, A., & Carter, C. (2006). Combustion enhancement via stabilized piecewise nonequilibrium gliding arc plasma discharge. *AIAA journal*, 44(1), 142-150.
- Ombrello, T., Ju, Y., & Fridman, A. (2008). Kinetic ignition enhancement of diffusion flames by nonequilibrium magnetic gliding arc plasma. *AIAA journal*, 46(10), 2424-2433.
- Onischuk, A. A., Di Stasio, S., Karasev, V. V., Baklanov, A. M., Makhov, G. A., Vlasenko, A. L., & Panfilov, V. N. (2003). Evolution of structure and charge of soot aggregates during and after formation in a propane/air diffusion flame. *Journal of Aerosol Science*, 34, 383-403.
- Padley, P. J., & Sugden, T. M. (1962). Eighth Symposium (International) on Combustion. *Williams and Wilkins*, 164.
- Perkins Jr, G., Laramy, R. E., & Lively, L. D. (1963). Flame Response in the Quantitative Determination of High Molecular Weight Paraffins and Alcohols by Gas Chromatography. *Analytical Chemistry*, 35(3), 360-362.

- Pedersen, T., & Brown, R. C. (1993). Simulation of electric field effects in premixed methane flames. *Combustion and Flame*, 94(4), 433-448.
- Place, E. R., & Weinberg, F. J. (1966). Electrical control of flame carbon. *Proceedings of the Royal Society of London. Series A. Mathematical and Physical Sciences*, 289(1417), 192-205.
- Prager, J., Riedel, U., & Warnatz, J. (2007). Modeling ion chemistry and charged species diffusion in lean methane-oxygen flames. *Proceedings of the Combustion Institute*, 31, 1129-1137.
- Reischl, G. P., Scheibel, H. G., & Porstendörfer, J. (1983). The bipolar charging of aerosols: Experimental results in the size range below 20-nm particle diameter. *Journal of Colloid and Interface Science*, 91(1), 272-275.
- Rogak, S. N., & Flagan, R. C. (1992). Bipolar diffusion charging of spheres and agglomerate aerosol particles. *Journal of aerosol science*, 23(7), 693-710.
- Sahu, M., Park, J., & Biswas, P. (2012). In Situ Charge Characterization of TiO₂ and Cu-TiO₂ Nanoparticles in a Flame Aerosol Reactor. *Journal of Nanoparticle Research*, 14, 1-11.
- Salkar, G. U. (2011). *Opposed Flow Oxy-Fuel Diffusion Flame Synthesis of One-Dimensional Vanadium Oxide Nanostructures on Solid Support* (Master's thesis, North Carolina State University).
- Savel'ev, A. M., & Starik, A. M. (2006). Interaction of ions and electrons with nanoparticles in hydrocarbon combustion plasmas. *Technical Physics*, 51, 444-452.
- Schaeublin, N. M., Braydich-Stolle, L. K., Schrand, A. M., Miller, J. M., Hutchison, J., Schlager, J. J., & Hussain, S. M. (2011). Surface charge of gold nanoparticles mediates mechanism of toxicity. *Nanoscale*, 3, 410-420.
- Sgro, L. A., D'Anna, A., & Minutolo, P. (2010). Charge distribution of incipient flame-generated particles. *Aerosol Science and Technology*, 44, 651-662.

- Shin, W. G., Wang, J., Mertler, M., Sachweh, B., Fissan, H., & Pui, D. Y. (2010). The effect of particle morphology on unipolar diffusion charging of nanoparticle agglomerates in the transition regime. *Journal of Aerosol Science*, 41(11), 975-986.
- Skalov, B. and Sokolic, A., *J. Phys. Chem. (Rus)*, 1934.5, 617.
- Sodha, M. S., & Guha, S. (1971). Physics of colloidal plasmas. *Advances in Plasma Physics*, 4, 219.
- Speelman, N., Kiefer, M., Markus, D., Maas, U., de Goey, L. P. H., & van Oijen, J. A. (2014). Validation of a novel numerical model for the electric currents in burner-stabilized methane–air flames. *Proceedings of the Combustion Institute*.
- Starik, A. M., Savel'ev, A. M., Titova, N. S., & Schumann, U. (2002). Modeling of sulfur gases and chemiions in aircraft engines. *Aerospace Science and Technology*, 6(1), 63-81.
- Starik, A. M., Savel'ev, A. M., & Titova, N. S. (2008). Formation of charged nanoparticles in hydrocarbon flames: principal mechanisms. *Plasma Sources Science and Technology*, 17(4), 045012.
- Sugden, T. M., Goodings, J. M., Jones, J. M., & Parkes, D. A. (1973). Combustion Institute (European) Symposium.
- Tree, D. R., & Svensson, K. I. (2007). Soot processes in compression ignition engines. *Progress in Energy and Combustion Science*, 33(3), 272-309.
- Tsuji, H. (1982). Counterflow diffusion flames. *Progress in energy and combustion science*, 8(2), 93-119.
- Warnatz, J., Maas, U., & Dibble, R. W. (2006). *Combustion: physical and chemical fundamentals, modeling and simulation, experiments, pollutant formation*. Springer.
- Wen, H. Y., Reischl, G. P., & Kasper, G. (1984). Bipolar diffusion charging of fibrous aerosol particles—I. Charging theory. *Journal of aerosol science*, 15(2), 89-101.
- Wersborg, B.L., Howard, J.B., & Williams, G.C. (1973) Physical mechanisms in carbon formation in flames. *Proceedings of the Combustion Institute* , 14, 929-940.

- Zhang, H., & Wang, D. (2008). Controlling the growth of charged-nanoparticle chains through interparticle electrostatic repulsion. *Angewandte Chemie*, 120, 4048-4051.
- Zobnin, A. V., Nefedov, A. P., Sinel'Shchikov, V. A., & Fortov, V. E. (2000). On the charge of dust particles in a low-pressure gas discharge plasma. *Journal of Experimental and Theoretical Physics*, 91, 483-487.

APPENDICES

Appendix A: Numerical scheme for the charging model

Fixed Ion and Electron concentration (Constant Bi-polar environment)

Let

For $z < 0$

$$A_z = S_A n_{th(z)} \Big|_{z < 0}; \quad A_{z-1} = S_A n_{th(z-1)} \Big|_{z < 0};$$

$$B'_z = S_A N_e \frac{v_e}{4} \exp\left(\frac{ze^2}{4\pi\epsilon_0 k_b T a}\right); \quad B'_{z+1} = S_A N_e \frac{v_e}{4} \exp\left(\frac{(z+1)e^2}{4\pi\epsilon_0 k_b T a}\right);$$

$$C'_z = S_A N_+ \frac{v_+}{4}; \quad C'_{z-1} = S_A N_+ \frac{v_+}{4};$$

For $z \geq 0$

$$A_z = S_A n_{th(z)} \Big|_{z > 0}; \quad A_{z-1} = S_A n_{th(z-1)} \Big|_{z > 0}; \quad B'_z = S_A N_e \frac{v_e}{4}; \quad B'_{z+1} = S_A N_e \frac{v_e}{4};$$

$$C'_z = S_A N_+ \frac{v_+}{4}; \quad C'_{z-1} = S_A N_+ \frac{v_+}{4};$$

\therefore Hence,

For $z < 0$ & $z \geq 0$

$$\frac{dN_z}{dt} = A_{z-1} N_{z-1} + B'_{z+1} N_{z+1} - A_z N_z - B'_z N_z + C'_{z-1} N_{z-1} - C'_z N_z$$

Using Forward Finite Difference method in time t, time step being k

$$\frac{N_z^{k+1} - N_z^k}{\Delta t} = A_{z-1}N_{z-1}^k + B'_{z+1}N_{z+1}^k - A_zN_z^k - B'_zN_z^k + C'_{z-1}N_{z-1}^k - C'_zN_z^k$$

Electrons in equilibrium with the charged particles

For $z < 0$

$$B_z = S_A \frac{v_e}{4} \exp\left(\frac{ze^2}{4\pi\epsilon_0 k_b T a}\right); B_{z+1} = S_A \frac{v_e}{4} \exp\left(\frac{(z+1)e^2}{4\pi\epsilon_0 k_b T a}\right)$$

$$C_z = S_A \frac{v_+}{4}; C_{z-1} = S_A \frac{v_+}{4};$$

For $z \geq 0$

$$B_z = S_A \frac{v_e}{4}; B_{z+1} = S_A \frac{v_e}{4}$$

$$C_z = S_A \frac{v_+}{4}; C_{z-1} = S_A \frac{v_+}{4};$$

\therefore Hence,

For $z < 0$ & $z \geq 0$

Nanoparticle charging equation, for $z = -\infty$ to $+\infty$

$$\frac{dN_z}{dt} = A_{z-1}N_{z-1} + B_{z+1}N_e N_{z+1} - A_z N_z - B_z N_e N_z + C_{z-1}N_+ N_{z-1} - C_z N_+ N_z$$

Using Forward Finite Difference method in time t , time step being k

$$\frac{N_z^{k+1} - N_z^k}{\Delta t} = A_{z-1}N_{z-1}^k + B_{z+1}N_e^k N_{z+1}^k - A_z N_z^k - B_z N_e^k N_z^k + C_{z-1}N_+^k N_{z-1}^k - C_z N_+^k N_z^k$$

$$\frac{N_z^{k+1} - N_z^k}{\Delta t} = A_{z-1}N_{z-1}^k + B_{z+1}N_e^k N_{z+1}^k - A_z N_z^k - B_z N_e^k N_z^k + C_{z-1}N_+^k N_{z-1}^k - C_z N_+^k N_z^k$$

$$\therefore N_z^{k+1} = N_z^k + \Delta t \left(A_{z-1}N_{z-1}^k + B_{z+1}N_e^k N_{z+1}^k - A_z N_z^k - B_z N_e^k N_z^k + C_{z-1}N_+^k N_{z-1}^k - C_z N_+^k N_z^k \right)$$

$$N_z^{k+1} = N_z^k \left(1 - \Delta t \left[A_z + B_z N_e^k + C_z N_+^k \right] \right) + N_{z-1}^k \left(\Delta t \left[A_{z-1} + C_{z-1} N_+^k \right] \right) + N_{z+1}^k \left(\Delta t B_{z+1} N_e^k \right)$$

$$\text{Let, } P^k = \left(1 - \Delta t \left[A_z + B_z N_e^k + C_z N_+^k \right] \right); Q^k = \Delta t \left[A_{z-1} + C_{z-1} N_+^k \right]; R^k = \Delta t B_{z+1} N_e^k;$$

$$\therefore N_z^{k+1} = N_z^k P^k + N_{z-1}^k Q^k + N_{z+1}^k R^k$$

Electron production equation

$$\text{Let, } \left. \frac{dN_e}{dt} \right|_{\text{chemi}} = k_1 [CH][O] - k_{\text{recomb}} N_e N_+$$

$$\therefore \frac{dN_e}{dt} = k_1 [CH][O] - k_{\text{recomb}} N_e N_+ + \sum_{-\infty}^{-1} A_{z(z<0)} N_z + \sum_0^{\infty} A_{z(z \geq 0)} N_z - \sum_{-\infty}^{-1} \underbrace{N_z N_e B_z}_{z<0} - \sum_0^{\infty} \underbrace{N_z N_e B_z}_{z \geq 0}$$

$$\text{Let } k_1 [CH][O] = D;$$

Using Forward-finite difference method in time t and step k ;

$$\begin{aligned} \frac{N_e^{k+1} - N_e^k}{\Delta t} &= D - k_{recomb} N_e^k N_+^k + \sum_{-\infty}^{-1} A_{z(z<0)} N_z^k + \sum_0^{\infty} A_{z(z \geq 0)} N_z^k - \underbrace{\sum_{-\infty}^{-1} N_z^k N_e^k B_z}_{z \geq 0} - \underbrace{\sum_0^{\infty} N_z^k N_e^k B_z}_{z \geq 0} \\ N_e^{k+1} &= N_e^k + \Delta t \left(D - k_{recomb} N_e^k N_+^k + \sum_{-\infty}^{-1} A_{z(z<0)} N_z^k + \sum_0^{\infty} A_{z(z \geq 0)} N_z^k - \underbrace{\sum_{-\infty}^{-1} N_z^k N_e^k B_z}_{z \geq 0} - \underbrace{\sum_0^{\infty} N_z^k N_e^k B_z}_{z \geq 0} \right) \\ \therefore N_e^{k+1} &= \Delta t D + N_e^k \left(1 - \Delta t \left[k_{recomb} N_+^k + \sum_{-\infty}^{-1} N_z^k B_z + \sum_0^{\infty} N_z^k B_z \right] \right) + \Delta t \left(\sum_{-\infty}^{-1} A_{z(z<0)} N_z^k + \sum_0^{\infty} A_{z(z \geq 0)} N_z^k \right) \end{aligned}$$

Let $A_z N_z^k = U^k$; $B_z N_z^k = V^k$;

$$\therefore N_e^{k+1} = \Delta t D + N_e^k \left(1 - \Delta t \left[k_{recomb} N_+^k + \sum_{-\infty}^{\infty} V^k \right] \right) + \Delta t \left(\sum_{-\infty}^{\infty} U^k \right)$$

Ion production equation

Let, $\left. \sum \frac{dN_+}{dt} \right|_{chemi} = k_1 [CH][O] - k_{recomb} N_e N_+$

Using Forward-finite difference method in time t and step k ;

$$\frac{N_+^{k+1} - N_+^k}{\Delta t} = D - k_{recomb} N_e^k N_+^k - \sum_{-\infty}^{\infty} N_z^k N_+^k C_z$$

Let $C_z N_z^k = W^k$;

$$\frac{N_+^{k+1} - N_+^k}{\Delta t} = D - k_{recomb} N_e^k N_+^k - \sum_{-\infty}^{\infty} W^k N_+^k$$

$$\therefore N_+^{k+1} = N_+^k + \Delta t \left(D - k_{recomb} N_e^k N_+^k - \sum_{-\infty}^{\infty} W^k N_+^k \right)$$

$$\therefore N_+^{k+1} = \Delta t D + N_+^k \left(1 - \Delta t \left[k_{recomb} N_e^k + \sum_{-\infty}^{\infty} W^k \right] \right)$$

We have to solve the following $(2m+3)$ equations for $z = -m$ to $+m$ at each time step k ; {1 equation for neutral particle, $2m$ equations to include positive and negative charges and 1 equation for electron and ion each}

$$\begin{aligned} \therefore N_z^{k+1} &= N_z^k P^k + N_{z-1}^k Q^k + N_{z+1}^k R^k \\ N_e^{k+1} &= \Delta t D + N_e^k \left(1 - \Delta t \left[k_{recomb} N_+^k + \sum_{-\infty}^{\infty} V^k \right] \right) + \Delta t \left(\sum_{-\infty}^{\infty} U^k \right) \\ N_+^{k+1} &= \Delta t D + N_+^k \left(1 - \Delta t \left[k_{recomb} N_e^k + \sum_{-\infty}^{\infty} W^k \right] \right) \end{aligned}$$